UNIVERSITY OF SOUTHAMPTON

Plasmon excitations in metallic nanostructures

by

Maxim Bashevoy

A thesis submitted for the degree of

Doctor of Philosophy

Faculty of Engineering, Science and Mathematics
Optoelectronics Research Centre

January 2008

UNIVERSITY OF SOUTHAMPTON

ABSTRACT

FACULTY OF ENGINEERING, SCIENCE AND MATHEMATICS
OPTOELECTRONICS RESEARCH CENTRE

Doctor of Philosophy

PLASMON EXCITATIONS IN METALLIC NANOSTRUCTURES

by Maxim Bashevoy

A new hyperspectral imaging technique and apparatus for imaging plasmon excitations and cathodoluminescence in nanostructures with nanoscale resolution have been developed. The apparatus, based on a scanning electron microscope synchronized with a multi-channel spectrum analyzer, allows for collection and detection of optical electron-induced emission from a sample in two configurations (high efficiency and high angular resolution modes) and in the wavelength region from 350 to 1150 nm with 0.8 nm spectral resolution and high quantum efficiency.

Using this instrument it was demonstrated that the injection of a beam of free electrons into an unstructured metal surface creates a highly localized nanoscale source of SPPs. It was shown that on a gold surface a 50 keV electron beam of 10 μA current creates a 10 nW source of plasmons with the spectrum spreading from 350 to 1150 nm. The plasmons were detected by controlled decoupling into light with a grating at a distance from the excitation point. The 30 nm delocalization of the plasmon source at the grating was demonstrated and decay lengths of SPPs were measured.

The hyperspectral imaging technique was used to study plasmon emission, induced by an electron beam excitation on gold monocrystal decahedron-shaped nanoparticles and dimers consisting of such nanoparticles. It was shown that in 100 nm gold decahedron-shaped nanoparticles electron-induced plasmon emission is excited in the spectral range from 350 to 850 nm. The dependence of spatial and spectral structure of dimer plasmon emission on wavelength and separation between the nanoparticles within the dimer was studied. The excitation of hybridized mode on a dimer with a 50 nm gap between the particles was detected at wavelength 600 nm.

It was demonstrated that the electromagnetic field structure near a plasmonic nanoparticle forms a vortex. It was shown that the power-flow lines of linear polarized monochromatic light interacting with a metal $\lambda/20$ nanoparticle, in the proximity of its plasmon resonance, form whirlpool-like nanoscale optical vortices (optical whirlpools). Both spherical and spheroidal particles were studied using analytical Mie theory and the Finite Element method. One of two types of vortices, inward or outward, was observed depending on the sign of frequency detuning between the external field and plasmon resonance of the nanoparticle.

Contents

Acknowledgements

I would like to thank my supervisor Professor Nikolay Zheludev for his guidance, assistance and encouragement throughout my time as a research student.

I would also like to express my gratitude to those with whom I worked, both in Southampton and at other institutions, in particular K. MacDonald, B. Soares, F. Jonsson, A. Schwanecke, A. Krasavin, V. Fedotov, S. Birtwell, Y. Chen, F. García de Abajo and M. Stockman.

Furthermore, I would like to thank the technical and administrative staff at the Department of Physics and Astronomy, and Optoelectronic Research Centre for the help afforded to me over the years.

I would like to acknowledge the Dorothy Hodgkin Postgraduate Award for providing the funding enabling me to study at Southampton, as well as SPANS and the Engineering and Physical Sciences Research Council, United Kingdom, for funding my attendance at conferences.

Finally, I would like to thank Gem and all of my family and friends for their support and encouragement.

Chapter 1

Introduction

1.1 Introduction

Optics will always be one of the most exciting areas of physical science. By definition, optics is the scientific study of light and vision. In other words, optics answers the question that has bothered mankind for centuries: why do we see objects in the way that we do?

The familiarity of this question might seem like an advantage, but most people never thought carefully about light and vision. Even intelligent people who studied vision came up with incorrect ideas. The ancient Greeks, Arabs and Chinese had theories of light and vision, all of which were mostly wrong, and all of which were accepted for thousands of years [1].

The Greek philosophers Pythagoras (575–490 BC) and Empedocles of Acragas (490–430 BC), who unfortunately were very influential, claimed that we see an object due to emission of some mysterious matter from both the object and our eye. When our eye's matter collided with the object's, the object would become evident to our sense of sight. Today, photography is the simplest experimental evidence that nothing needs to be emitted from our eyes and hit an object to make it visible.

Despite the naïvety of the theory, many of the ideas of the ancient Greeks were accurate. Empedocles was one of the first people to state the theory that light travels at a finite (although very fast) speed, a theory that gained acceptance only much later. Another Greek philosopher, Aristotle (384–322 BC) rightly explained rainbows as a reflection off raindrops.

Claudius Ptolemaeus (83–161 AD), known in English as Ptolemy, is the first recorded person to experiment with optics and collect data. In his work "Optics" he writes about the properties of light, including reflection, refraction and color. Ptolemy's work was further developed by the Egyptian scientist Ibn al Haythen, who drew first ray diagrams. His work was influential in later studies of light.

The 16th to 18th centuries are marked by the invention of the optical microscope and debates over the nature of light. Sir Isaac Newton (1642–1727) believed in the particle theory of light, in part because he did not observe diffraction of light, a property it should have if it were a wave. His contemporary, Christiaan Huygens (1629–1695) was the first to write of light as a wave. Because of Newton's prestige, the particle theory was accepted for almost a century.

It was not until the early 19th century that the wave theory of light became widely accepted due to the experimental work of Thomas Young (1773–1829) on light diffraction. In the same century, Augustin-Jean Fresnel (1788–1827) and later James Clerk Maxwell (1831–1879), working within a wave theory of light seemed to explain phenomena that Newton had been unable to interpret in terms of a particle theory of light, such as polarization, interference, and diffraction. This question was reopened in the 20th century with the rise of quantum theory.

It was the Irish mathematician Sir William Rowan Hamilton (1805–1865) who developed a theory that joined optics and mechanics, thus elucidating the relationship between wave and particle viewpoints. His theory helped lay the foundation for the later development of quantum mechanics.

The investigations into the manipulation and focusing of light, for centuries conducted in parallel to the discovery of its nature, soon hit one of the fundamental limits. The resolution of telescopes and microscopes appeared to be limited by the wave nature of light. The mathematical theory correlating resolution to the wavelength of light was formulated by Ernst Karl Abbe (1840–1905). For most optical systems the resolution is limited to approximately half a wavelength of light.

A tremendous amount of research has been conducted during 20th century to overcome the fundametal diffraction limit. In 1903 an Austrian-German chemist Richard Zsigmondy (1865–1929) invented an ultramicroscope, allowing imaging of colloidal particles with a size below the diffraction limit of light [2]. Illuminating particles from the side and keeping the field of view of the microscope dark, it was possible to observe the particles as bright specs. For his work he received the Nobel prize in Chemistry in 1908.

In 1928, an Irish scientist E.H. Synge introduced an idea of using a small aperture to image a surface with sub-wavelength resolution using optical light. For the small opening, he suggested using either a pinhole in a metal plate or a quartz cone that is coated with a metal except for at the tip [3, 4]. Almost sixty years later this idea was realized in the optical range by the groups of D.W. Pohl and A. Lewis in 1984 [5, 6]. The new technique was called scanning near-field optical microscopy (SNOM) and allowed optical imaging with the resolution of $\lambda/20$.

It was scanning optical microscopy that opened the door to manipulation of light at a nanoscale. The SNOM probe is a convenient way to launch surface plasmon polaritons (SPPs) — coupled light–electron oscillations propagating along metal–dielectric interfaces with incredible localization. By coupling light into SPPs the imaging, propagation and control of light far beyond the diffraction limit became available [7–14].

By that time, however, surface plasmons were well-known. First predicted in 1957 by Rufus Ritchie [15], and later observed in metal films bombarded by an electron beam [16, 17], surface plasmon polaritons have been studied by a wide variety of scientists since the demonstration of SPP excitation by prisms in 1968 [18, 19]. At this point the optical response of gold and silver nanoparticles has been described. Another major discovery in the field of metal optics occurred with the observation of strong Raman scattering from pyridine molecules in the vicinity of roughened silver surfaces [20–23]. This observation led to the now well established field of Surface Enhanced Raman Scattering (SERS) [24–27]. All these discoveries have set the stage for the current surge in surface plasmon *nanophotonics* — the study of the behavior of light on a nanometer scale [28, 29].

This rising interest in plasmon based research is happening at a time where crucial technological areas such as optical lithography, optical data storage, and high density electronics manufacturing are approaching fundamental limits. Several current technological challenges may be overcome by utilizing the unique properties of surface plasmon polaritons. Thanks to many recent studies, a wide range of plasmon-based optical elements and techniques have now been developed, including a variety of passive waveguides, active switches, biosensors, lithography masks, and more. These developments have led to the notion of *plasmonics*, the science and technology of metal-based optics and nanophotonics [30].

One of the experimental challenges of the plasmonics today is the lack of a highly localized and powerful source of surface plasmons that can be easily repositioned on a nanoscale. Existing methods of SPP generation either do not allow high localization of SPPs on a nanoscale (prisms, gratings) or are cumbersome (SNOM). In Chapter 3 of this thesis it is demonstrated that such a source of SPPs can be generated by a beam of free electrons on an unstructured metal surface. Moreover, a new imaging technique has been developed using this method of generation of surface plasmon polaritons. Application of this technique to gratings and nanodimers is described in Chapters 4 and 5.

Certain problems of plasmonics, such as determination of electromagnetic field structure, both in the vicinity of and inside metallic nanoparticles, can not currently be approached experimentally. In this case, the information can be obtained through numerical and analytical modeling. The excitation of vortex-like structures of light powerflow on metallic nanoparticles near plasmon resonance has been demonstrated by a theoretical technique, described in Chapter 2 of this thesis.

As noted above, nanophotonics is a new and rapidly growing area of optics. The importance of the research within this field is evidenced by the implementation of related national programs in many countries. Despite the tremendous progress achieved by mankind in the understanding of light interaction with matter, many fascinating discoveries are still to be made in the field of plasmonics.

1.2 Thesis plan

This thesis is divided into six chapters:

This first chapter is an introduction to the subject areas that have been investigated, with a brief outline of the subsequent chapters.

Chapter 2 describes the studies of whirlpool-like nanoscale optical vortices formed by power-flow lines of light interacting with a metallic nanoparticle.

Chapter 3 details experiments which demonstrate that the injection of a beam of free electrons into an unstructured gold surface creates a highly localized source of traveling surface plasmons with spectra centered below the surface plasmon resonance frequency.

Chapter 4 describes a novel hyperspectral imaging technique for surface plasmon polaritons on metallic nanostructures. This technique uses a scanning electron beam and allows for simple visualization of light emission from decoupled plasmons, providing information on decay lengths and feature sizes with nanometer resolution.

Chapter 5 describes studies of the spatial and spectral mode structure of single nanoparticles and nano-dimers using the hyperspectral imaging technique for surface plasmons.

Chapter 6 concludes the thesis with a summary of the results reported in previous chapters and a discussion of ongoing and potential research work.

The work reported in this thesis was carried out while the author was registered as a postgraduate student within the School of Physics and Astronomy and the Optoelectronics Research Centre at the University of Southampton, UK. It is, unless otherwise indicated, the original work of the author.

1.3 References

[1] B. Crowell. *Optics*. Fullerton: Light and Matter, 2007.

[2] R. Zsigmondy. *Colloids and the ultramicroscope*. London: Chapman and Hall, 1914.

[3] E.H. Synge. A suggested method for extending the microscopic resolution into the ultramicroscopic region. *Phil. Mag.*, 6:356, 1928.

[4] E.H. Synge. An application of piezo-electricity to microscopy. *Phil. Mag.*, 13:297, 1932.

[5] D.W. Pohl, W. Denk, and M. Lanz. Optical stethoscopy: image recording with the resolution $\lambda/20$. *Appl. Phys. Lett.*, 44(7):651, 1984.

[6] A. Lewis, M. Isaacson, A. Harootunian, and A. Murray. Development of a 500 angstrom spatial resolution light microscope. I. Light is efficiently transmitted through $\lambda/16$ diameter apertures. *Ultramicroscopy*, 13:227, 1984.

[7] S.I. Bozhevolnyi, I.I. Smolyaninov, and A.V. Zayats. Near-field microscopy of surface-plasmon polaritons: localization and internal interface imaging. *Phys. Rev. B*, 51(24):17916, 1995.

[8] B. Hecht, H. Bielefeldt, L. Novotny, Y. Inouye, and D.W. Pohl. Local excitation, scattering, and interference of surface plasmons. *Phys. Rev. Lett.*, 77(9):1889, 1996.

[9] J.R. Krenn, R. Wolf, A. Leitner, and F.R. Aussenegg. Near-field optical imaging the surface plasmon fields of lithographically designed nanostructures. *Opt. Comm.*, 137(1):46, 1997.

[10] K. Imura, H. Okamoto, M.K. Hossain, and M. Kitajima. Visualization of localized intense optical fields in single gold-nanoparticle assemblies and ultrasensitive Raman active sites. *Nano Lett.*, 6(10):2173, 2006.

[11] H. Okamoto and K. Imura. Near-field imaging of optical field and plasmon wavefunctions in metal nanoparticles. *J. Mat. Chem.*, 16(40):3920, 2006.

[12] A. Huber, N. Ocelic, D. Kazantsev, and R. Hillenbrand. Near-field imaging of mid-infrared surface phonon polariton propagation. *Appl. Phys. Lett.*, 87(8):081103, 2005.

[13] S.I. Bozhevolnyi. Near-field mapping of surface polariton fields. *J. Microsc.*, 202(2):313, 2001.

[14] S. Ducourtieux, V.A. Podolskiy, S. Grésillon, S. Buil, B. Berini, P. Gadenne, A.C. Boccara, J.C. Rivoal, W.D. Bragg, K. Banerjee, V.P. Safonov, V.P. Drachev, Z.C. Ying, A.K. Sarychev, and V.M. Shalaev. Near-field optical studies of semicontinuous metal films. *Phys. Rev. B*, 64(16):165403, 2001.

[15] R.H. Ritchie. Plasma losses by fast electrons in thin films. *Phys. Rev.*, 106(5):874, 1957.

[16] C.J. Powell and J.B. Swan. Origin of the characteristic electron energy losses in magnesium. *Phys. Rev.*, 116(1):81, 1959.

[17] C.J. Powell and J.B. Swan. Origin of the characteristic electron losses in aluminum. *Phys. Rev.*, 115(4):869, 1959.

[18] A. Otto. Excitation of nonradiative surface plasma waves in silver by the method of frustrated total reflection. *Z. Physik A*, 216(4):1431, 1968.

[19] E. Kretschmann and H. Raether. Radiative decay of nonradiative surface plasmons excited by light. *Z. Naturforsch*, 23:2135, 1968.

[20] C.V. Raman and K.S. Krishnan. A new type of secondary radiation. *Nature*, 121:501, 1928.

[21] M. Fleischmann, P.J. Hendra, and A.J. McQuillan. Raman spectra of pyridine adsorbed at a silver electrode. *Chem. Phys. Lett.*, 26(2):163, 1974.

[22] D.L. Jeanmaire and R.P. Van Duyne. Surface Raman spectroelectrochemistry: Part I. Heterocyclic, aromatic, and aliphatic amines adsorbed on the anodized silver electrode. *J. Electroanal. Chem.*, 84(1):1, 1977.

[23] M.G. Albrecht and J.A. Creighton. Anomalously intense Raman spectra of pyridine at a silver electrode. *J. Am. Chem. Soc.*, 99(15):5215, 1977.

[24] G. Gouadec and P. Colomban. Raman spectroscopy of nanostructures and nanosized materials. *J. Raman Spec.*, 38(6):598, 2007.

[25] K. Kneipp and H. Kneipp. Single molecule Raman scattering. *Appl. Spec.*, 60(12):322A, 2006.

[26] C.E. Talley, J.B. Jackson, C. Oubre, N.K. Grady, C.W. Hollars, S.M. Lane, T.R. Huser, P. Nordlander, and N.J. Halas. Surface-enhanced Raman scattering from individual Au nanoparticles and nanoparticle dimer substrates. *Nano Lett.*, 5(8):1569, 2005.

[27] K. Kneipp, H. Kneipp, I. Itzkan, R.R. Dasari, and M.S. Feld. Surface-enhanced Raman scattering and biophysics. *J. Phys. Cond. Matter*, 14(18):R597, 2002.

[28] M.L. Brongersma and P.G Kik, editors. *Surface plasmon nanophotonics*. Springer, 2007.

[29] A.V. Krasavin, K.F. MacDonald, and N.I. Zheludev. *Active plasmonics*. Nanophotonics with Surface Plasmons. Elsevier Science, 2007.

[30] S.A. Maier. *Plasmonics: fundamentals and applications*. Springer, New York, 2007.

Chapter 2

Optical whirlpools on an absorbing metallic nanoparticle

2.1 Synopsis

It has been found that the power-flow lines of linear polarized monochromatic light interacting with a metallic nanoparticle, in the proximity of its plasmon resonance, form whirlpool-like nanoscale optical vortices (optical whirlpools). These vortices were independently observed using analytical Mie theory and 3D finite element numerical modeling of the Maxwell equations.

The theoretical apparatus developed for simulations of light interaction with the nanoparticle is outlined in Section 2.4 with the full theoretical background being detailed in Section 2.3. In the following Section, a series of Mie theory simulations, performed on a metallic spherical nanoparticle, using the full three-dimensional solution of Maxwell's equations, and the results thereof, are described. This illustrates four different regimes of light interaction with a nanoparticle in the vicinity of its plasmon resonance: weak interaction, high-loss regime, and the creation of both outward and inward whirlpool-like vortices on the nanoparticle. The parameter field for both vortex regimes, again detailed in the Section 2.5, demonstrates the possibility of excitation of such whirlpool-like structures on 20 nm silver nanoparticles in the upper ultra-violet and visible wavelength regions. In Section 2.6 the excitation of the same four light–nanoparticle interaction regimes has been demonstrated for an oblate metallic spheroid with semiaxis ratio 2 by finite element method simulations.

2.2 Introduction

Given the extensive range of existing and potential applications, in fields such as Raman spectroscopy [1–4], all-optical nano-switching memory [5–7], design of plasmonic [8–11] and metamaterial waveguides [12–14], biological nanosensing [15–17], the study of the optical properties of metal nanoparticles in the vicinity of the plasmon resonance is very important. These applications rely on the fact that the properties of such nanoparticles, both individual and collective, are very different from those of the corresponding bulk materials. Most notable among these properties are a high localization of electromagnetic fields around the nanoparticle and extreme dependance of emission on the surrounding media, boundary state, and distance to nearby nanoparticles.

To study the optical properties of nanoparticles near plasmon resonance it is necessary to solve the full three-dimensional system of Maxwell equations and obtain exact values of $\mathbf{E}$ and $\mathbf{H}$ components of the electromagnetic field around and inside the nanoparticle. Approximate approaches such as Rayleigh scattering are not applicable for this purpose, although they provide convenient dimensionless parameters, for example scattering and absorption cross-sections, helping relate the results of the calculations to observable values [18]. The solution to the problem can be obtained by Mie theory, giving an exact analytical solution for spherical particles, or using numerical techniques, such as Finite Element Method (FEM), for complex geometries.

During my simulations of linear polarized monochromatic light scattering on a subwavelength aperture blocked by a homogeneous metallic nanoparticle it was found that powerflow lines of light in the vicinity of the nanoparticle follows "vortex" trajectory. It was also found that such vortex-like behavior of light persists on an isolated nanoparticle in the same illumination conditions. These peculiar features of the interaction of linear polarized monochromatic light with homogeneous nanoparticles, hereinafter denoted as *optical whirlpools*, became a separate subject of the research described in this Chapter. The difference between optical whirlpools and well-known *optical vortices* is detailed below.

Optical vortices have been identified as phase singularities in wavefronts of monochromatic light fields [19]. Consider a complex monochromatic scalar field ψ, with amplitude $\rho(\mathbf{r})$ and phase $\varphi(\mathbf{r})$ (suppressing the time dependence $e^{-i\omega t}$):

$$\psi(\mathbf{r}) = \rho(\mathbf{r})e^{i\varphi(\mathbf{r})}$$

A *phase singularity* exists at point $\mathbf{r}$ if the amplitude $\rho(\mathbf{r})$ is zero, and hence the phase $\varphi(\mathbf{r})$ is undefined. The condition $\psi(\mathbf{r}) = 0$ is equivalent to:

$$\mathrm{Re}[\rho(\mathbf{r})] = 0, \qquad \mathrm{Im}[\rho(\mathbf{r})] = 0.$$

These two conditions imply that phase singularities can be found as lines in three-dimensional space, whereas in two dimensions, they are typically separate points. The phase around a phase singularity possesses a vortex-like structure, and increases or decreases as one moves around the singularity. Optical vortices can be found in three dimensional beams with helical wave fronts [20]. In a typical laser beam in a vacuum the wavefronts (surfaces of the constant phase) are planar and the wavevectors are parallel to the axis of the beam (Fig. 2.1a). Beams with helical wavefronts can be generated by diffraction of a normal laser beam on a specially designed computer-generated hologram [21], and these beams possess a linear phase singularity that coincides with the beam axis and wavevectors spiral along it (Fig. 2.1b).

The first mention of optical vortices seems to date back to the theoretical studies, carried out in 1950s [22], of the diffraction of a plane wave by a perfectly conducting, infinitely thin half-plane. The systematic study of topological defects of wavefields [23] began with a study by Nye and Berry [24]. The latest developments in the field, now known as *singular optics*, can be found in reviews [25–30].

Optical whirlpools, or *optical whirlpool-like vortices*, are identified as whirlpool-like vortex structures in the streamlines of the Poynting vector (lines of energy flow) [31]. As illustrated in Figure 2.1c, the energy flow of light around a metal spherical nanopartice has peculiar features: powerflow lines penetrate the particle near its centerline, then, on exiting the particle, the flow-lines turn away from the centerline and enter a spiral trajectory.

Optical whirlpools have been detected in Sommerfeld's edge diffraction. The discussion of the eel-like motion of light at the edge is dated back to Newtonian times [28]. Recently vortices were found in light diffracted by narrow slits in silver and silicon [19, 32]. Complex patterns of energy flux in the near-field region around a small particle and the observation of energy flow "input windows" on the particle surface have also been observed [33].

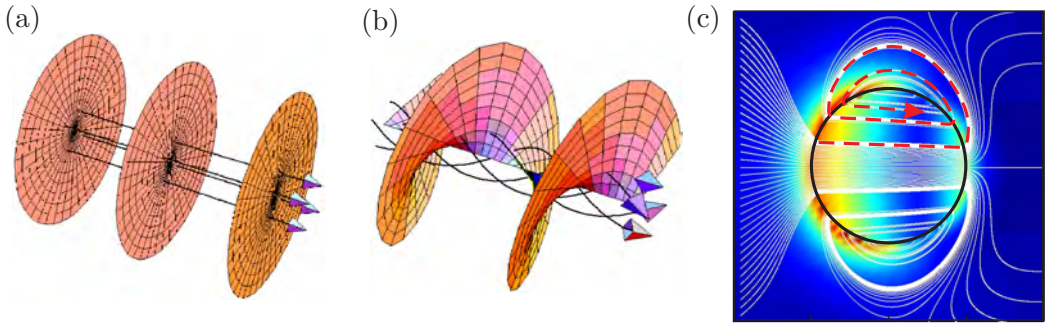

Figure 2.1: Optical vortices and optical whirlpools. *Optical vortices* have been identified as phase singularities in wavefronts of monochromatic light fields. The phase around a phase singularity possesses a vortex-like structure, and increases or decreases as one moves around the singularity. Laser beam with a planar wave front (a): wavevectors are parallel to the beam axis. Optical vortex in a laser beam with a helical wavefront (b): phase singularity along the beam axis and wavevectors spiraling along it [20]. *Optical whirlpools* are whirlpool-like vortex structures in the streamlines of the Poynting vector [31]. Optical whirlpool on a metallic nanoparticle in the vicinity of its plasmon resonance (see Section 2.5): powerflow lines penetrate the particle near its centerline then, on exiting the particle, the flow-lines turn away from the centerline and enter a spiral trajectory (c).

In the series of simulations discussed in this chapter two different types of vortex have been detected. The outward vortex first penetrates the particle near its centerline then, on exiting the particle, the flow-lines turn away from the centerline and enter a spiral trajectory. Outward vortices are seen for wavelengths shorter than the plasmon resonance. For wavelengths longer that the plasmon resonance the vortex is inward: the power-flow lines pass around the sides of the particle before turning towards the centerline and entering the particle to begin their spiral trajectory. Excitation of both vortex regimes has been demonstrated on a metal spherical (see Section 2.5)

and oblate spheroidal nanoparticle (Section 2.6). The theoretical background of methods used for the simulations and analysis is described in detail in the following Section.

2.3 Theoretical basis of the computational apparatus for simulation and analysis of light interaction with nanoparticles

In this Section the theoretical background of the analytical and numerical apparatus used to demonstrate the excitation of optical whirlpool-like vortices on homogenous spherical- and oblate spheroid-shaped nanoparticles by linear polarized monochromatic light: Mie theory, optical cross-sections formalism, Finite Element Method (FEM), Perfectly Matched Layer boundary conditions, and their implementation for FEM, is discussed.

2.3.1 Mie theory

The boundary-value problem of scattering of a monochromatic plane wave by a homogeneous sphere of an arbitrary radius and dielectric coefficient is often referred to as "Mie problem" or "Mie solution." The basis for the association of the problem with the name of the German physicist Gustav Mie (1869–1857) is a classic paper published in 1908 [34]. Mie developed the complete analytical solution of the problem and discussed its significance in terms of partial electric and magnetic waves. This solution was then used as the basis for the explanation of the colors of metal sols.

An examination of literature of the late 1800's, conducted by Nelson Logan [35, 36] in the early sixties, reveals that the Mie problem was formulated and solved long before original publication by G. Mie. In 1861 one of the greatest mathematicians of the 19th century, Alfred Clebsch (1833–1872) developed the mathematical theory required to solve the class of boundary-value problems in which a wave propagating in an elastic medium impinges upon a spherical surface [37]. However, this 68-page memoir was

buried within the pages of one of the leading mathematical journals to be rediscovered only in the middle of the nineteenth century.

The same fate was suffered by an equally great memoir [38] about the reflection and refraction of light by a transparent sphere, which was published in 1890 by Ludwig Lorenz (1829–1891). Lorenz derived the formulas which later came to be known as the Mie solution. In his paper Mie refers to Lorenz's theory for the color of metal sols made up of small particles. However, although Mie was familiar with Lorenz's preliminary papers, he was apparently unaware of this memoir.

The modern formulation of the Mie solution can be found in any classical book on electromagnetic theory [18, 39–41]. The Mie solution was firstly applied to meteorological optics, including numerical simulations of rainbows and glories [42–45]. At present the theory is widely used in nanophotonics, particularly in cases involving single metallic nanoparticles [46] and nanoparticle waveguides [47]. The underlying principles of Mie theory, following [41], are detailed below.

Mie theory is a complete analytical solution for the scattering of linear polarized monochromatic light wave by a sphere of arbitrary size and dielectric constant. Components of electromagnetic field at all points in the particle and at all points of the homogeneous medium in which the particle is embedded are determined. Mie theory can also be applied to problems with arbitrary illumination by decomposing the incident wave into its Fourier components and obtaining the solution by superposition.

The field inside the particle is denoted by $(\mathbf{E}_1, \mathbf{H}_1)$; in the medium surrounding the particle the field $(\mathbf{E}_2, \mathbf{H}_2)$ is the superposition of the incident field $(\mathbf{E}_i, \mathbf{H}_i)$ and the scattered field (Fig. 2.2):

$$\mathbf{E}_2 = \mathbf{E}_i + \mathbf{E}_s, \quad \mathbf{H}_2 = \mathbf{H}_i + \mathbf{H}_s,$$

where:

$$\mathbf{E}_i = \mathbf{E}_0 \exp(i\mathbf{k} \cdot \mathbf{x} - i\omega t), \quad \mathbf{H}_i = \mathbf{H}_0 \exp(i\mathbf{k} \cdot \mathbf{x} - i\omega t),$$

and $\mathbf{k}$ is the wave vector appropriate to the surrounding medium.

The fields must satisfy the Maxwell equations

$$\nabla \cdot \mathbf{E} = 0, \tag{2.1}$$

$$\nabla \cdot \mathbf{H} = 0, \tag{2.2}$$

$$\nabla \times \mathbf{E} = i\omega\mu\mathbf{H}, \tag{2.3}$$

$$\nabla \times \mathbf{H} = -i\omega\varepsilon\mathbf{E}, \tag{2.4}$$

at all points where ε and μ are continuous.

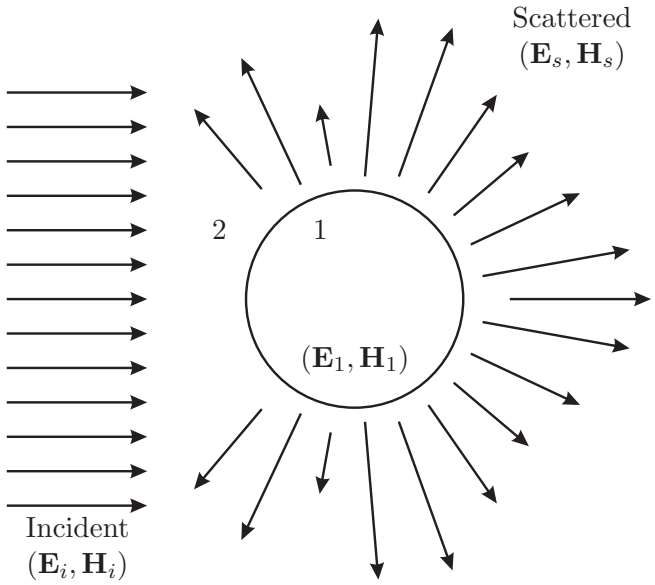

Figure 2.2: Electromagnetic fields in Mie problem: the incident monochromatic wave $(\mathbf{E}_i, \mathbf{H}_i)$ gives rise to a field $(\mathbf{E}_1, \mathbf{H}_1)$ inside the spherical particle and a scattered field $(\mathbf{E}_s, \mathbf{H}_s)$ in the medium surrounding the particle. Total field outside the particle is a superposition of the incident field and scattered field: $\mathbf{E}_2 = \mathbf{E}_i + \mathbf{E}_s$, $\mathbf{H}_2 = \mathbf{H}_i + \mathbf{H}_s$ [41].

In the spherical system of coordinates each component of the electromagnetic field in and around the particle can be expanded in vector spherical harmonics [41]. The field inside the particle:

$$\mathbf{E}_i = E_0 \sum_{n=1}^{\infty} i^n \frac{2n+1}{n(n+1)} (\mathbf{M}_{o1n}^{(1)} - i\mathbf{N}_{e1n}^{(1)}),$$

$$\mathbf{H}_i = -\frac{k}{\omega\mu} E_0 \sum_{n=1}^{\infty} i^n \frac{2n+1}{n(n+1)} (\mathbf{M}_{e1n}^{(1)} + i\mathbf{N}_{o1n}^{(1)}).$$

The expansion of the field $(\mathbf{E}_1), \mathbf{H}_1$ is:

$$\mathbf{E}_1 = \sum_{n=1}^{\infty} E_n \left(c_n \mathbf{M}_{o1n}^{(1)} - i d_n \mathbf{N}_{e1n}^{(1)} \right),$$
$$\mathbf{H}_1 = -\frac{k_1}{\omega \mu_1} \sum_{n=1}^{\infty} E_n (d_n \mathbf{M}_{e1n}^{(1)} + i c_n \mathbf{N}_{o1n}^{(1)}),$$

and the scattered field is:

$$\mathbf{E}_s = \sum_{n=1}^{\infty} E_n \left(i a_n \mathbf{N}_{e1n}^{(3)} - b_n \mathbf{M}_{o1n}^{(3)} \right),$$
$$\mathbf{H}_s = \frac{k}{\omega \mu} \sum_{n=1}^{\infty} E_n (i b_n \mathbf{N}_{o1n}^{(3)} + a_n \mathbf{M}_{e1n}^{(3)}).$$

Here $E_n = i^n E_0 (2n+1)/n(n+1)$, E_0 is the amplitude of the incident field, μ_1 is the permeability of the sphere, k_1 is the wave number in the sphere. Coefficients a_n, b_n, c_n, and d_n can be found from the boundary conditions. The explicit expressions of the field components are presented in Appendix A.

2.3.2 Extinction, scattering, and absorption by a small nanoparticle

Suppose that a beam of electromagnetic radiation is illuminating the aperture of a detector. Placing particles in front of the detector will result in the decrease of the electromagnetic energy received by the detector: the presence of the particles has resulted in *extinction* of the incident beam, which can be accounted for by *absorption* (i.e. transformation of electromagnetic energy into other forms) in the particles and *scattering* by the particles, provided the medium in which the particles are embedded is nonabsorbing. Although this extinction depends on a wide range of parameters such as size and shape of the particles, polarization and frequency of the incident beam, and so on, it nevertheless can be described for any system of particles in terms of cross sections.

The ratio of the net rate at which electromagnetic energy crosses a surface A of an imaginary sphere of radius r around the particle to incident

irradiance I_i is a quantity with dimensions of area:

$$C_{\text{abs}} = -\int_A \frac{1}{2}\text{Re}\{\mathbf{E}_2 \times \mathbf{H}_2^*\} \cdot \hat{\mathbf{e}}_r dA \,/ I_i \tag{2.5}$$

and is denoted as a *absorption cross section*.

The sum of the *scattering cross section*

$$C_{\text{sca}} = -\int_A \frac{1}{2}\text{Re}\{\mathbf{E}_s \times \mathbf{H}_s^*\} \cdot \hat{\mathbf{e}}_r dA \,/ I_i \tag{2.6}$$

and the absorption cross section gives the extinction cross section:

$$C_{\text{ext}} = C_{\text{abs}} + C_{\text{sca}}.$$

The extinction cross section has a clear physical interpretation. Consider a single arbitrary particle interposed between a source of light and a detector. It can be shown [41] that the effect of the particle is to reduce the detector area by C_{ext}. In the language of geometrical optics one would say that the particle "casts the shadow" of area C_{ext}. However, this "shadow" can be considerably greater — or much less — than the particle's geometrical shadow.

Extinction, scattering and absorption cross sections of a homogeneous sphere can be calculated using Mie coefficients a_n and b_n:

$$C_{\text{ext}} = \frac{W_{\text{ext}}}{I_i} = \frac{2\pi}{k^2}\sum_{n=1}^{\infty}(2n+1)\text{Re}\{a_n + b_n\}, \tag{2.7}$$

Similarly, the scattering and absorption cross sections are:

$$C_{\text{sca}} = \frac{W_s}{I_i} = \frac{2\pi}{k^2}\sum_{n=1}^{\infty}(2n+1)\left(|a_n|^2 + |b_n|^2\right), \quad C_{\text{abs}} = C_{\text{ext}} - C_{\text{sca}}. \tag{2.8}$$

Although equations (2.7) and (2.8) give the exact expressions for the cross sections of a spherical particle, it is difficult to apply the approach used to derive them, to a particle of a different shape.

For small particles with:

$$x \ll 1, \qquad |m|x \ll 1, \tag{2.9}$$

where x is a size parameter and m is a relative refractive index (see Section 2.3.1), the extinction cross section can be defined through *polarizability* α. This approach is often referred to as *Rayleigh approximation*:

$$C_{\text{ext}} = k\text{Im}\{\alpha\} = \pi a^2 4x\text{Im}\left\{\frac{\varepsilon_1 - \varepsilon_m}{\varepsilon_1 + 2\varepsilon_m}\right\}, \tag{2.10}$$

$$C_{\text{sca}} = \frac{k^4}{6\pi}|\alpha|^2 = \pi a^2 \frac{8}{3} x^4 \left|\frac{\varepsilon_1 - \varepsilon_m}{\varepsilon_1 + 2\varepsilon_m}\right|^2, \tag{2.11}$$

$$C_{\text{abs}} = C_{\text{ext}} - C_{\text{sca}}. \tag{2.12}$$

Formulas (2.10)–(2.12) can be applied to any particle with a cross section α and satisfying (2.9). For an oblate spheroid with semiaxes $a = b$, c with dielectric constant ε_1 surrounded by medium ε_m the polarizability is

$$\alpha = 4\pi abc \frac{\varepsilon_1 - \varepsilon_m}{3\varepsilon_m + 3L(\varepsilon_1 - \varepsilon_m)}, \tag{2.13}$$

where L is a geometrical factor defined by

$$L = \frac{g(e)}{2e^2}\left[\frac{\pi}{2} - \tan^{-1} g(e)\right] - \frac{g(e)}{2e^2}, \tag{2.14}$$

$$g(e) = \left(\frac{1 - e^2}{e^2}\right)^{1/2}, \qquad e^2 = 1 - \frac{c^2}{a^2}. \tag{2.15}$$

2.3.3 Finite element method

The finite element method (FEM) is a numerical technique for obtaining approximate solutions to boundary-value problems of mathematical physics [48–54]. Perhaps no other approximation method had a greater impact on the theory and practice of numerical methods during the twentieth century [55]. Finite element method has now been used in virtually every conceivable area of engineering and science that can make use of models of nature characterized by partial differential equations.

It is difficult to trace the origins of finite element method because of a basic problem in defining precisely what constitutes a "finite element method." In 1891 K. Schellbach [56] proposed a finite-element-like solution to Plateau's problem [57, 58] of determining the minimum surface area enclosed

by a given closed curve. If a finite element method is one in which a global approximation of a partial differential equation is built up from a sequence of local approximations over subdomains, then credit must go to A. Hrennikoff [59], who applied the method to solve plane elasticity problems in his early papers. To most mathematicians the origins of the FEM are frequently traced to the appendix of a paper by R. Courant [60] in which piecewise linear approximations of the Dirichlet problem over a network of triangles is discussed.

The 1970's represent a decade in which the generality of finite element methods began to be appreciated over a large portion of the mathematics and scientific community and it was during this period that significant applications to highly nonlinear problems were made. The fact that very general nonlinear phenomena in continuum mechanics, including problems of finite deformation of solids and of flow of viscous fluids could be modeled by finite elements and solved on existing computers was demonstrated in the early seventies [61], and, by the end of that decade, several "general purpose" finite element programs were in use by engineers to treat broad classes of nonlinear problems in solid mechanics and heat transfer. Now one of the most popular software packages implementing a three dimensional Final Elements method is Comsol Multiphysics, which was used to perform series of simulations on optical whirlpools.

The alternative to the Finite Elements methods is a group of Finite Difference methods (FDM), particularly Finite-Difference Time-Domain method. The main advantages of the Finite Element method are: the ease of implementation and availability of exceptionally well developed software packages; the ability of FEM to handle complex geometries, which is theoretically straightforward; and the quality of the FEM solution is generally higher than in the corresponding FDM approach. Despite its mathematically simple definition, a sphere is a complex object for a numerical technique, especially one with an inherently rectangular grid like FDM. Like every numerical technique, FEM has its disadvantages. While the Finite Difference method approximates the equation, the Finite Element method approximates the solution to the equation. In this sense FEM solutions are always approximate.

Generally FEM requires more memory to complete the solution, which is also extremely sensitive to mistakes in the boundary conditions and initialization of sources.

A typical boundary-value problem [54] can be defined by a governing differential equation in a domain Ω:

$$\mathcal{L}\varphi = f \tag{2.16}$$

together with the boundary conditions on the boundary Γ that encloses the domain. In (2.16), $\mathcal{L}$ is a differential operator, f is the excitation or forcing function, and φ is the unknown quantity. In electromagnetics, the form of the governing differential equation ranges from simple Poisson equations to complicated scalar wave equations. The boundary conditions also range from the simple Dirichlet and Neumann conditions, to complicated impedance and radiation conditions, and even more complicated higher-order conditions.

The principle of the Finite Element method is to replace an entire continuous domain by a number of subdomains in which the unknown function is represented by simple interpolation functions with unknown coefficients. Thus, the original boundary-value problem (2.16), with an infinite number of degrees of freedom, is converted into a problem with a finite number degrees of freedom, or in other words, the solution of the entire system is approximated by a finite number of unknown coefficients. Then a system of algebraic equations is obtained by applying a variational method, and finally, solution of the boundary-value problem is achieved by solving the system of equations. Therefore, a finite element analysis of a boundary-value problem should include the following basic steps: *discretization of the domain*, *selection of interpolation functions*, *formulation of the system of equations* and *solution of the system of equations*. Each step of the analysis, following [54], is described in detail below.

Discretization of the domain. The discretization of the domain Ω, is the first and perhaps the most important step in any finite element analysis because the manner in which the domain is discretized will affect the computer storage requirements, the computation time, and the accuracy of the numerical results. In this step, the entire domain Ω is subdivided

into a number of small domains, denoted as Ω^e ($e = 1, 2, 3, \ldots, M$), with M denoting the total number of subdomains. These subdomains are usually referred to as *elements*. For a one-dimensional domain (a straight or curved line), the elements are often short line segments interconnected to form (at least approximately) the original line (Fig. 2.3a). For a two-dimensional domain, the elements are usually small triangles and rectangles (Fig. 2.3b). The rectangular elements are, of course, best suited for discretizing rectangular regions, while the triangular ones can be used for irregular regions. In three-dimensional solution, the domain may be subdivided into tetrahedra, triangular prisms, or rectangular bricks (Fig. 2.3c). Of these, the tetrahedra are the simplest and best suited for arbitrary-volume domains. Figure 2.4 shows examples of the finite element discretization of a two- and three-dimensional domain.

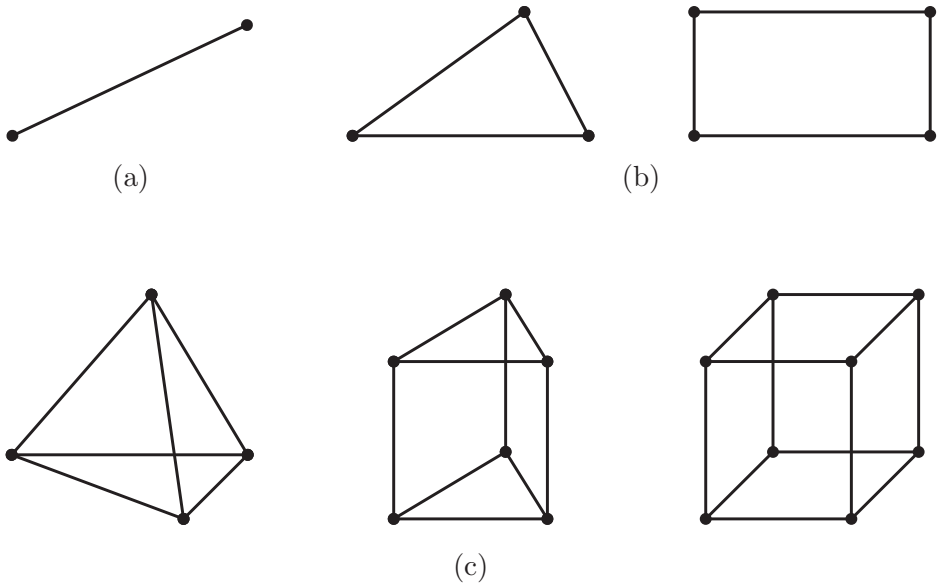

Figure 2.3: Basic finite elements for the discretization of the finite element computational domain: short line for one-dimentional (a), triangle and rectangle for two-dimensional domain (b), tetrahedron, triangular prism, and rectangular brick for three-dimensional (c) [54].

The problem is formulated in terms of the unknown function φ at nodes associated with the elements. For example, a linear line element has two

nodes, one at each endpoint. A linear triangular element has three nodes, located in its three vertices, whereas a linear tetrahedron has four nodes, located at its four corners. For implementation purposes, it is necessary to describe these nodes. A complete description of a node contains its coordinate values, local number and global number, is a task requiring special consideration [54].

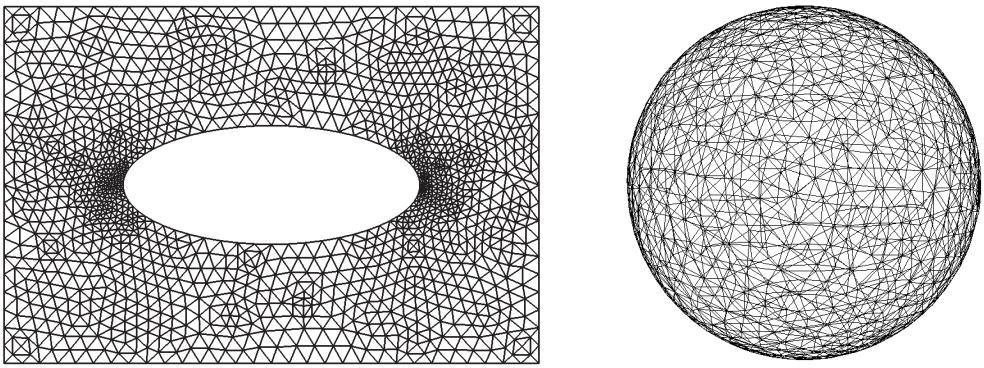

(a) (b)

Figure 2.4: Examples of finite element discretization: two dimensional computational domain discretized with triangular elements (a) for the case of prolate spheroid in free space, three-dimensional sphere with tetrahedral elements (b) [62].

Selection of interpolation functions. The second step of a finite element analysis is the selection of an interpolation function that provides an approximation of the unknown solution within an element. The interpolation is usually selected to be a polynomial of first (linear), second (quadratic), or higher order. Higher-order polynomials, although very accurate, usually result in a more complicated formulation than lower-order polynomials. Hence, the simple linear interpolation is still widely used. Once the order of the polynomial is selected, an expression for the unknown solution in an element, say element e, can be derived in the following form:

$$\tilde{\varphi}^e = \sum_{j=1}^{n} N_j^e \varphi_j^e = \{N^e\}^T \{\varphi^e\} = \{\varphi^e\}^T \{N^e\}, \tag{2.17}$$

where n is the number of nodes in the element, φ_j^e is the value of φ at node j of the element, and N_j^e is the interpolation function for node j, which is known as the *expansion* or *basis function*. The highest order of the functions N_j^e for a given element is referred to as the *order of the element*; for example, if the N_j^e are linear functions, the element e is a linear element. An important feature of the functions N_j^e is that they are nonzero only within the element e, and outside this element they vanish.

Formulation of the system of the equations. The third step in a finite element analysis is to formulate the system of equations. For that purpose the Ritz's method can be used, as described below.

The Ritz method, also known as the Rayleigh-Ritz method, is a variational method in which the boundary-value problem is formulated in terms of a variational expression, called *functional*. The minimum of this functional corresponds to the governing differential equation under the given boundary conditions. The approximate solution is then obtained by *minimizing the functional* with respect to variables that define a certain approximation to the solution.

Consider an inner product, denoted by angular brackets:

$$\langle \varphi, \psi \rangle = \int_\Omega \varphi \psi^* \, d\Omega,$$

where the asterisk denotes the complex conjugate. With this definition it can be shown that the solution of (2.16) can be obtained by minimizing the functional [63]:

$$F(\tilde{\varphi}) = \frac{1}{2}\langle \mathcal{L}\tilde{\varphi}, \tilde{\varphi} \rangle - \frac{1}{2}\langle \tilde{\varphi}, f \rangle - \frac{1}{2}\langle f, \tilde{\varphi} \rangle \tag{2.18}$$

with respect to $\tilde{\varphi}$, where $\tilde{\varphi}$ denotes a trial function. For the considered case the functional can be expressed as:

$$F(\tilde{\varphi}) = \sum_{e=1}^{M} F^e(\tilde{\varphi}^e), \tag{2.19}$$

where M is the number of the elements comprising the entire domain and

$$F^e(\tilde{\varphi}^e) = \frac{1}{2}\int_{\Omega^e} \tilde{\varphi}^e \mathcal{L}\tilde{\varphi}^e \, d\Omega - \int_{\Omega^e} f\tilde{\varphi}^e \, d\Omega. \tag{2.20}$$

Substituting (2.17) into (2.20) and using the matrix form, we obtain:

$$F^e = \frac{1}{2}\{\varphi^e\}^T[K^e]\{\varphi^e\} - \{\varphi^e\}^T\{b^e\}, \tag{2.21}$$

where $[K^e]$ is an $n \times n$ matrix and $\{b^e\}$ an $n \times 1$ column vector with their elements given by:

$$K_{ij}^e = \int_{\Omega^e} N_i^e \mathcal{L} N_j^e \, d\Omega, \qquad b_i^e = \int_{\Omega^e} f N_i^e \, d\Omega.$$

Substituting (2.21) into (2.19) and performing the summation and adopting the global node numbers, we obtain:

$$F = \frac{1}{2}\{\varphi\}^T[K]\{\varphi\} - \{\varphi\}^T\{b\},$$

where $[K]$ is an $N \times N$ symmetric matrix, with N being the total number of unknowns or nodes, $\{\varphi\}$ is an $N \times 1$ unknown vector, whose elements are the unknown expansion coefficients, and $\{b\}$ an $N \times 1$ known vector. The system of equations is then obtained by imposing the stationarity requirement $\delta F = 0$, or equivalently, by setting the partial derivative of F with respect to φ_i to zero:

$$\frac{\partial F}{\partial \varphi_i} = \frac{1}{2}\sum_{j=1}^{N}(K_{ij} + K_{ji})\varphi_j - b_i = 0, \qquad i = 1, 2, 3, \ldots, N. \tag{2.22}$$

Since $[K]$ is symmetric, $K_{ij} = K_{ji}$, and therefore (2.22) becomes:

$$\frac{\partial F}{\partial \varphi_i} = \sum_{j=1}^{N} K_{ij}\varphi_j - b_i = 0, \qquad i = 1, 2, 3, \ldots, N$$

or in matrix form:

$$[K]\{\varphi\} = \{b\}. \tag{2.23}$$

Before the system of equations (2.23) is ready to be solved for a specific solution, the required boundary conditions have to be applied.

It is seen that the formulation of a system of equations is actually composed of three steps: formulate the *elemental equation* (2.21), sum the elemental equations over all elements to *form the system of equations*, and finally, *impose boundary conditions* to obtain the final form of the system of equations.

Solution of the system of equations. Solving the system of equations is the final step in a finite element analysis. The resultant system has one of the following two forms:

$$[K]\{\varphi\} = \{b\} \tag{2.24}$$

or

$$[A]\{\varphi\} = \lambda[B]\{\varphi\}. \tag{2.25}$$

Equation (2.24) is of the deterministic type, resulting from either an inhomogeneous differential equation or inhomogeneous boundary conditions or both. In electromagnetics, deterministic systems are usually associated with scattering, radiation, and other problems where there exists a source of excitation. On the other hand, Equation (2.25) is of the eigenvalue type, resulting from a homogeneous governing differential equation and homogeneous boundary conditions. In electromagnetics, eigenvalue systems are usually associated with source-free problems such as wave propagation in waveguides and resonances in cavities.

2.3.4 Perfectly matched layer (PML) boundary conditions

When solving open-region light scattering problems, such as Mie scattering by a free-standing sphere, the infinite region exterior to the scatterer must be truncated with an artificial boundary to limit the size of the computational domain. Such a condition should make the boundary appear as transparent as possible to the scattered field, or in other words, it should minimize the nonphysical reflections from that boundary. An ideal boundary condition is one that possesses zero reflection for all angles of incidence. Unfortunately, except for those derived from the boundary integral representation or the eigenfunction expansion of the scattered field[1], this ideal condition is unrealizable and an approximation is often used [54, 64].

[1]These methods are difficult to implement for complex geometries, and produce full matrices whose treatment requires excessive storage and computing time. This is particularly true for three dimensional problems.

One such approximation is the so-called *absorbing boundary conditions* (ABCs) [65–67], which are usually derived from differential wave equations. The ABCs are applied at the artificial boundary directly and, as a result, their use does not introduce additional unknowns. However, they do not yield zero reflection for all angles of incidence and thus are not exact. To minimise the solution error, they are often applied some distance away from the scatterer, resulting in an extended discretization region. However, the ABC's have two advantages in that: they do not increase the condition number of the FEM matrix, and they can have a perfect absorption at some prescribed angles of incidence.

An alternative "engineer's" approach, which can be used to truncate the infinite region in a finite element analysis was proposed by J. Jin et al. [68]. In this approach, the finite element mesh is truncated by a conducting boundary, either electric or magnetic, whose inner surface is coated with a layer or several layers of fictitious dielectric, whose thickness and constitutive parameters can be chosen to absorb the field over a wide range of incident angles. To a certain extent, this is similar to what happens in an anechoic chamber whose walls are coated with lossy material for absorbing the scattered field, thus simulating a free-space environment. This approach is referred to as the *fictitious absorbers method*.

The fictitious absorbers, however, are designed to work at a single frequency and they cannot be applied to a wide frequency band without redesign. In 1994 this problem was solved by J.P. Berenger [69], who proposed the concept of a *perfectly matched layer* (PML). A perfectly matched interface is an interface between two half spaces, one of which is lossy, however, the interface does not reflect a plane wave for all frequencies and all angles of incidence and polarizations. The loss of a wave in the lossy half-space is in the direction perpendicular to the interface.

The PML medium has been described in many different ways by various authors. In particular, Chew and Weedon [70] have interpreted the PML as *coordinate stretching* in a frequency domain. This approach is used to introduce perfectly matched layer below.

Derivation of PML based on coordinate stretching. Consider the modified source-free Maxwell's equations:

$$\nabla_s \times \mathbf{E} = -i\omega\mu\mathbf{H}, \tag{2.26}$$

$$\nabla_s \times \mathbf{H} = i\omega\varepsilon\mathbf{E}, \tag{2.27}$$

$$\nabla_s \cdot (\varepsilon\mathbf{E}) = 0, \tag{2.28}$$

$$\nabla_s \cdot (\mu\mathbf{H}) = 0, \tag{2.29}$$

where ∇_s is defined by:

$$\nabla_s = \widehat{x}\frac{1}{s_x}\frac{\partial}{\partial x} + \widehat{y}\frac{1}{s_y}\frac{\partial}{\partial y} + \widehat{z}\frac{1}{s_z}\frac{\partial}{\partial z}. \tag{2.30}$$

Therefore, ∇_s can be considered as the standard ∇ operator in Cartesian coordinates whose x, y, and z axes are *stretched* by a factor s_x, s_y, and s_z, respectively.

Now consider a plane wave whose electric and magnetic fields are given by

$$\begin{aligned} \mathbf{E} &= \mathbf{E}_0 e^{-i\mathbf{k}\cdot\mathbf{r}} = \mathbf{E}_0 e^{-i(k_x x + k_y y + k_z z)}, \\ \mathbf{H} &= \mathbf{H}_0 e^{-i\mathbf{k}\cdot\mathbf{r}} = \mathbf{H}_0 e^{-i(k_x x + k_y y + k_z z)}. \end{aligned} \tag{2.31}$$

From equations (2.26) and (2.28) we can obtain the dispersion relation

$$\left(\frac{k_x}{s_x}\right)^2 + \left(\frac{k_y}{s_y}\right)^2 + \left(\frac{k_z}{s_z}\right)^2 = \omega^2\mu\varepsilon = k^2. \tag{2.32}$$

The obvious solution to this equation is:

$$k_x = k s_x \sin\theta\cos\varphi \tag{2.33}$$

$$k_y = k s_y \sin\theta\sin\varphi \tag{2.34}$$

$$k_z = k s_z \cos\theta. \tag{2.35}$$

This demonstrates that when s_x is a complex number, the wave will be *attenuated* in the x-direction, and the same is true in the other two dimensions. The wave impedance is:

$$\eta = \frac{|\mathbf{E}|}{|\mathbf{H}|} = \frac{|k_s|}{\omega\varepsilon} = \frac{\omega\mu}{|k_s|} = \sqrt{\frac{\mu}{\varepsilon}}, \tag{2.36}$$

which indicates that the stretching factors do not affect the wave impedance.

Next consider plane-wave reflection by the interface of two half-spaces in the stretched coordinate system (Fig. 2.5). For the TE_z case, the incident, reflected, and transmitted fields can be written as:

$$\mathbf{E}_i = \mathbf{E}_0 e^{-i\mathbf{k}_i\cdot\mathbf{r}} \tag{2.37}$$

$$\mathbf{E}_r = R^{\mathrm{TE}}\mathbf{E}_0 e^{-i\mathbf{k}_r\cdot\mathbf{r}} \tag{2.38}$$

$$\mathbf{E}_t = T^{\mathrm{TE}}\mathbf{E}_0 e^{-i\mathbf{k}_t\cdot\mathbf{r}} \tag{2.39}$$

where $\mathbf{E}_0$ is a constant vector perpendicular to $\widehat{z}$, and R^{TE} and T^{TE} denote the reflection and transmission coefficients, respectively.

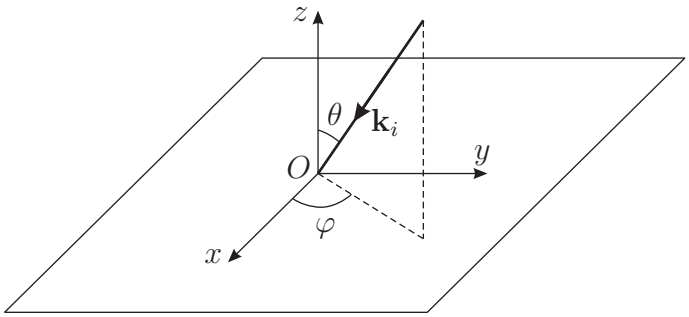

Figure 2.5: Plane-wave reflection by the interface of two half-spaces.

Using the phase-matching continuity conditions for $\mathbf{E}$ and $\mathbf{H}$, we obtain:

$$R^{\mathrm{TE}} = \frac{k_{1z}s_{2z}\mu_2 - k_{2z}s_{1z}\mu_1}{k_{1z}s_{2z}\mu_2 + k_{2z}s_{1z}\mu_1}. \tag{2.40}$$

Here the subscript 1 denotes the parameters in the upper half-space and subscript 2 denotes those in the lower half-space. Similarly, we find the reflection coefficient for the TM_z case as:

$$R^{\mathrm{TM}} = \frac{k_{1z}s_{2z}\varepsilon_2 - k_{2z}s_{1z}\varepsilon_1}{k_{1z}s_{2z}\varepsilon_2 + k_{2z}s_{1z}\varepsilon_1}. \tag{2.41}$$

From the case-matching conditions $k_{1x} = k_{2x}$ and $k_{1y} = k_{2y}$, we obtain:

$$k_1 s_{1x}\sin\theta_1\cos\varphi_1 = k_2 s_{2x}\sin\theta_2\cos\varphi_2 \tag{2.42}$$

$$k_1 s_{1y}\sin\theta_1\cos\varphi_1 = k_2 s_{2y}\sin\theta_2\cos\varphi_2 \tag{2.43}$$

Clearly, if we choose $\varepsilon_1 = \varepsilon_2$, $\mu_1 = \mu_2$, $s_{1x} = s_{2x}$, and $s_{1y} = s_{2y}$, we have:

$$R^{\mathrm{TE}} = 0, \qquad R^{\mathrm{TM}} = 0 \tag{2.44}$$

which remains true regardless of the choice of s_{1z} and s_{2z}, the angle of incidence, and the frequency.

To illustrate PML algorithm, we allow $s_{2z} = s' - is''$ to be a constant, where s' and s'' are real numbers with $s' \geqslant 1$ (for faster decay of evanescent waves) and $s'' \geqslant 0$ (for absorption of propagating wave), then $k_{2z} = k_2(s' - is'')\cos\theta$ and the transmitted wave will be attenuated by the factor $\exp(k_2 s'' z \cos\theta)$ in the z-direction. If we place a metal plane a distance of L away from the interface, the magnitude of the reflection coefficient becomes

$$|R(\theta)| = e^{-2k_2 s'' L\cos\theta} \tag{2.45}$$

assuming that k_2 is a real constant.

Clearly, a metal-backed PML can be used to truncate the computational domain for numerical solution of partial differential equations. The basic scheme is shown in Figure 2.6, where the scatterer of interest is surrounded by PML, which is terminated by a metal. Hence, the computational domain becomes *finite*.

The choice of the PML parameters depends on its position. For a PML perpendicular to the x-axis:

$$s_x = s' - js'', \qquad s_y = s_z = 1.$$

Similarly, for a PML normal to the y-axis:

$$s_y = s' - js'', \qquad s_x = s_z = 1.$$

For the four corners:

$$s_x = s_y = s' - js'', \qquad s_z = 1.$$

The extension to the three-dimensional case is straightforward.

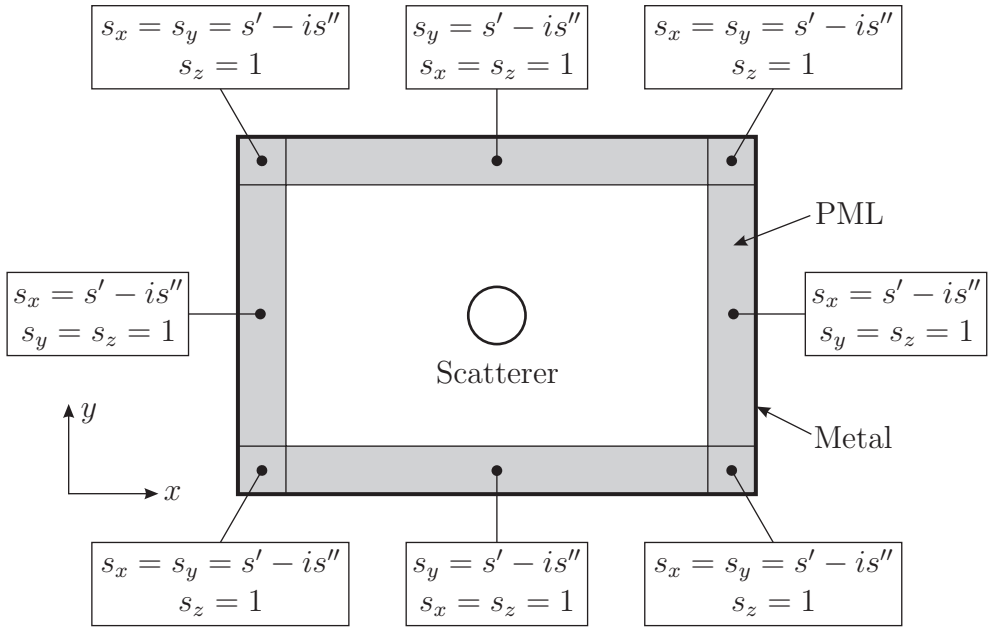

Figure 2.6: Basic scheme of two dimensional computational domain: the scatterer of interest is surrounded by a PML, terminated by a metal. The choice of PML parameters s_x, s_y and s_z depends on its position: for a PML perpendicular to the x-axis $s_x = s' - js''$ and $s_y = s_z = 1$ and so on. The extension to the three-dimensional case is straightforward [54].

Formulation of PML for Finite Element method. The implementation of PML to a Finite Element analysis is better understood with the interpretation of PML as an anisotropic absorber [71]. This can be done by first writing Maxwell's equations in an anisotropic medium as:

$$\nabla \times \mathbf{E} = -i\omega\bar{\boldsymbol{\mu}}\mathbf{H}, \tag{2.46}$$

$$\nabla \times \mathbf{H} = i\omega\bar{\boldsymbol{\varepsilon}}\mathbf{E}, \tag{2.47}$$

$$\nabla \cdot (\bar{\boldsymbol{\varepsilon}}\mathbf{E}) = 0, \tag{2.48}$$

$$\nabla \cdot (\bar{\boldsymbol{\mu}}\mathbf{H}) = 0, \tag{2.49}$$

where $\bar{\boldsymbol{\varepsilon}}$ and $\bar{\boldsymbol{\mu}}$ are the diagonal permittivity and permeability tensors given by:

$$\bar{\boldsymbol{\varepsilon}} = \begin{bmatrix} \varepsilon_{xx} & 0 & 0 \\ 0 & \varepsilon_{yy} & 0 \\ 0 & 0 & \varepsilon_{zz} \end{bmatrix}, \qquad \bar{\boldsymbol{\mu}} = \begin{bmatrix} \mu_{xx} & 0 & 0 \\ 0 & \mu_{yy} & 0 \\ 0 & 0 & \mu_{zz} \end{bmatrix} \tag{2.50}$$

Comparing (2.26)–(2.29) with (2.46)–(2.49), it is possible to find $\bar{\boldsymbol{\varepsilon}}$ and $\bar{\boldsymbol{\mu}}$ in terms of stretching factors s_x, s_y and s_y:

$$\bar{\boldsymbol{\varepsilon}} = \varepsilon\bar{\boldsymbol{\Lambda}}, \qquad \bar{\boldsymbol{\mu}} = \mu\bar{\boldsymbol{\Lambda}}$$

with:

$$\bar{\boldsymbol{\Lambda}} = \hat{x}\hat{x}\left(\frac{s_y s_z}{s_x}\right) + \hat{y}\hat{y}\left(\frac{s_z s_x}{s_y}\right) + \hat{z}\hat{z}\left(\frac{s_x s_y}{s_z}\right).$$

The anisotropic absorbers model of PML allows readily formulate the finite element solution. For the radiation case, the vector wave equation is:

$$\nabla \times [\bar{\boldsymbol{\mu}}^{-1} \cdot (\nabla \times \mathbf{E})] - \omega^2 \bar{\boldsymbol{\varepsilon}} \cdot \mathbf{E} = -j\omega\mathbf{J},$$

where $\mathbf{J}$ is the source of radiation. Since the associated operator is symmetric, based on the Ritz variational principle described in Section 2.3.3, the functional (2.18) is given by:

$$\begin{aligned} F(\mathbf{E}) &= \frac{1}{2}\iiint_V \left[(\nabla \times \mathbf{E}) \cdot \bar{\boldsymbol{\mu}}^{-1} \cdot (\nabla \times \mathbf{E}) - \omega^2 \mathbf{E} \cdot \bar{\boldsymbol{\varepsilon}} \cdot \mathbf{E}\right] dV \\ &+ \iiint_V \mathbf{E} \cdot \mathbf{J}\, dV. \end{aligned}$$

For the scattering case, the vector wave equation for the scattered field is given by:

$$\nabla \times [\bar{\boldsymbol{\mu}}^{-1} \cdot (\nabla \times \mathbf{E}^{\mathrm{sc}})] - \omega^2 \bar{\boldsymbol{\varepsilon}} \cdot \mathbf{E}^{\mathrm{sc}} = \mathbf{F}^{\mathrm{inc}},$$

where $\mathbf{F}^{\mathrm{inc}} = 0$ within the PML and:

$$\mathbf{F}^{\mathrm{inc}} = \nabla \times [\bar{\boldsymbol{\mu}}^{-1} \cdot (\nabla \times \mathbf{E}^{\mathrm{inc}})] - \omega^2 \bar{\boldsymbol{\varepsilon}} \cdot \mathbf{E}^{\mathrm{inc}}$$

within the physical domain. The functional then becomes:

$$\begin{aligned} F(\mathbf{E}^{\mathrm{sc}}) &= \frac{1}{2}\iiint_V \left[(\nabla \times \mathbf{E}^{\mathrm{sc}}) \cdot \bar{\boldsymbol{\mu}}^{-1} \cdot (\nabla \times \mathbf{E}^{\mathrm{sc}}) - \omega^2 \mathbf{E}^{\mathrm{sc}} \cdot \bar{\boldsymbol{\varepsilon}} \cdot \mathbf{E}^{\mathrm{sc}}\right] dV \\ &- \iiint_V \mathbf{E}^{\mathrm{sc}} \cdot \mathbf{F}^{\mathrm{inc}}\, dV. \end{aligned}$$

The implementation of PML to the Finite Element method therefore requires a special PML layer with the functional $F(\mathbf{E}^{\mathrm{sc}})$ around the free-space volume described by the functional $F(\mathbf{E})$. The full solution is obtained following procedures described in Section 2.3.3.

2.4 Simulation of the electromagnetic field structure around a metal nanoparticle

Numerous techniques allowing for the calculation of light interactions with a nanoparticle have been developed over the years (see Sections 2.3.1 and 2.3.3). As mentioned above, not all of them are applicable for the study of the optical properties of metallic nanoparticles of an arbitrary size in the vicinity the plasmon resonance. For reasons, outlined below, two approaches, constituting theoretical apparatus used for simulations in this chapter, have been selected: Mie theory and the Finite Element method.

Mie theory, described in detail in Section 2.3.1, gives an exact analytic solution of the vector wave equations on a homogeneous spherical particle

$$\bigtriangledown^2\mathbf{E} + k^2\mathbf{E} = 0, \qquad \bigtriangledown^2\mathbf{H} + k^2\mathbf{H} = 0,$$

in which every component of the electromagnetic fields, both inside the particle and in the surrounding medium is presented in the form of a series of spherical Bessel functions. The Mie theory algorithm was implemented on Mathworks Matlab software using the formulae presented in Appendix A.

Although Mie theory is well established and trusted, its results are presented in polynomial form, bringing up the question of conversion. It was decided to verify the Mie theory results (and vice versa) by comparing them with numerical solutions of the Maxwell equations by the Finite Elements method (FEM). Finite elements method is a numerical procedure for obtaining solutions to boundary-value problems defined by a governing differential equation (2.16) in a domain Ω:

$$\mathcal{L}\varphi = f,$$

together with the boundary conditions on the boundary Γ that encloses the domain. Here $\mathcal{L}$ is a differential operator, f is the excitation, and φ is the unknown quantity. In electromagnetics, the Poisson equation for the scalar potential in electrostatic field can be used as one of the examples of a governing differential equation:

$$-\nabla \cdot (\varepsilon \nabla \psi) = \rho,$$

where $\mathcal{L} = -\nabla \cdot (\varepsilon \nabla)$ is the differential operator, ψ — scalar potential (the unknown quantity φ), ε — permittivity of the medium and ρ is the electric charge density (the excitation f).

The principle of this method is to replace an entire continuous domain Ω by a number of subdomains in which the unknown function is represented by simple interpolation functions with unknown coefficients. The system of equations for the unknowns can be obtained by applying a variational method, and the solution to the boundary-value problem is therefore achieved by solving this system (see Section 2.3.3).

One of the advantages of the Finite Element method is that it could be applied to solve problems of light scattering on objects with complex geometries and various types of sources. The availability of exceptionally well developed FEM software packages makes the implementation of the method to a particular problem relatively easy. The 64-bit Comsol Multiphysics software was used for the numerical modelling of light scattering and absorption on nanoparticles, described in this chapter.

The simulation process by both Mie theory and Finite Element method consists of three major steps: *setup and discretization of the calculation volume*, analytical or numerical *simulations* according to the algorithm and *output of the results*. Each step for both Mie theory and FEM is detailed below.

Consider a spherical homogeneous particle with radius a. For Mie theory the computational domain is a free space ($4a \times 4a \times 4a$) cubic volume with the spherical nanoparticle centered inside it. The *cubic discretization* of the volume was selected using ($a/30 \times a/30 \times a/30$)-sized elements. The finite element method computational domain consisted of a free space volume of the same size as for the Mie theory with the nanoparticle in the center, and Perfectly Matched boundary conditions layer of the size $4a$, having virtually zero reflection at any angle of incidence, applied on every side of the cube. The Perfectly matched layer (PML) and its implementation for FEM is discussed in detail in Section (2.3.4). The discretization of the whole domain in the finite element method, including PML regions, was performed using *tetrahedral discretization elements* with variable sizes determined by

the convolution of the obtained solution. In the case of the oblate spheroidal nanoparticle, the computational domain was of the same size, a being a half of the long semiaxis of the spheroid. The structure and discretization of the domain for both Mie theory and FEM, for case of the spherical nanoparticle, is illustrated in Figure 2.7.

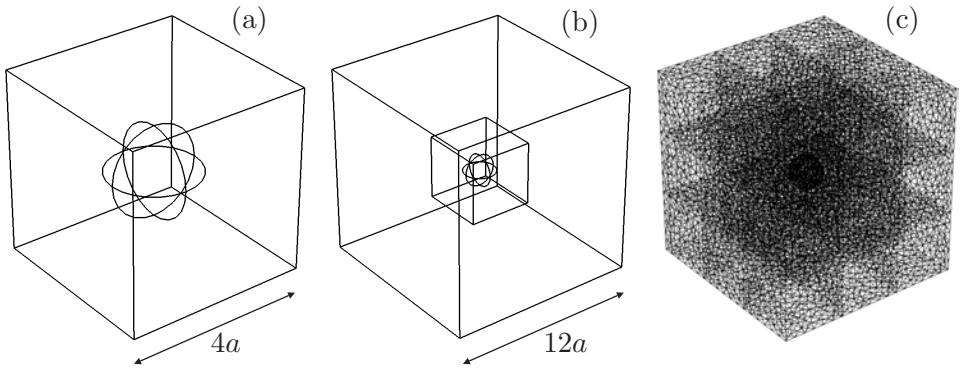

Figure 2.7: The structure and mesh of the computational domains for Mie theory and finite element method for the simulations of the light interaction with the spherical nanoparticle of radius a. For the Mie theory the computational domain consists of the free space volume and a nanoparticle in it (a). The descritization with cubic elements was used for the simulations. The free space volume, containing the nanoparticle in its centre, and surrounded by $4a$-thick layer of PML constitute the computational domain for the finite element method simulations (b). Tetrahedral discretization elements were used in the latter case (c).

Simulations of light scattering on a nanoparticle by Mie theory were performed by conversion of Cartesian (x, y, z) cubic mesh into polar spherical coordinates (r, θ, φ) and implementation of the full 3D Mie solution (see Appendix A). The upper limit of the summation in Mie formulae was determined by the convolution of the solution. Even for the cases of plasmon resonance on a nanoparticle it was enough to keep eight terms of the series. Finite element method simulations were performed using Unsymmetric MultiFrontal method for solving systems of linear equations [72–74], implemented in Comsol Multiphysics software.

To relate the parameter field for the calculations to observable values the dimensionless scattering C_{sca} and absorbtion C_{abs} *cross-sections* of the nanoparticle were used. The cross section has a clear physical interpretation:

the effect of a single arbitrary particle being interposed between a source of light and a detector is to reduce the detector area by C_{sca} or C_{abs}, depending on the process of scattering or absorption by the particle respectively. It worth mentioning that a cross section can be considerably greater — or much less — than the particle's geometrical cross section. Light interaction with a particle can be described by a process of extinction, accounting for both scattering and absorption, which can be characterized by its own cross section $C_{\text{ext}} = C_{\text{sca}} + C_{\text{abs}}$. The subject of cross section analysis of light interaction with particles, including exact formulae for spherical particles, based on Mie scattering coefficients, and general formulae for small particles, including oblate spheroid, is detailed in Section 2.3.2. In the following calculations, small particle (Rayleigh) approximation formulae for C_{abs} and C_{sca} were used (2.10)–(2.12) both for spherical nanoparticle (**??**) and oblate ellipsoid (2.13). All values for optical cross sections were normalized to geometrical cross section of the particle, so that $C_{\text{geo}} = 1$.

To illustrate the calculation results graphically, solutions in the plane of polarization of the incident light were plotted using powerflow lines and a color scale for the absolute value of the Poynting vector $\mathbf{P} = [\mathbf{E} \times \mathbf{H}]$ (red representing high values of $\mathbf{P}$ and blue representing low values). The powerflow lines are the lines to which the Poynting vector $\mathbf{P}$ is tangential. If $\mathbf{A}(t) = (x(t), y(t), z(t))$ is the Poynting vector field, the powerflow lines can be computed by integrating the differential equation: $d\mathbf{A}/dt = \mathbf{P}(\mathbf{A})$, where t is length of the path [75, 76]. Selecting a linear array of 10–15 starting points for the powerflow integration in front of the particle in the plane of polarization allows the tracing of general features of light interaction with the nanoparticle, like the formation of optical whirlpools.

It was found that the analytical results, obtained by Mie theory, and Finite Element method simulation results for the light interaction with spherical nanoparticles correlated remarkably well, giving similar energy flow patterns.

2.5 Optical whirlpools on metallic spheres

It was found that the vortex regime occurs in metallic nanoparticles in the vicinity of the plasmon absorbtion resonance. The spectral position of the plasmon resonance of a spherical particle illuminated by plane wave λ depends on the radius of the particle a and its dielectric coefficient $\varepsilon(\lambda) = \varepsilon'(\lambda) + i\varepsilon''(\lambda)$. The exact position of the absorption plasmon resonance corresponds to the maximum of the absorption cross section $C_{\text{abs}}(\lambda)$.

It was found that the existence of the vortex structure on a spherical nanoparticle and the topography of the field maps depend on the values of the real ε' and imaginary ε'' parts of the particle's complex dielectric coefficient. Figures 2.8(a) and (b) show the modification of the field structure around a hypothetical nanoparticle with $\varepsilon' = -2$, $\varepsilon'' = 10$ and $\varepsilon' = -2$, $\varepsilon'' = 1$ respectively. In the case depicted in Figure 2.8(a) the scattering and absorption cross-sections are much smaller than the geometrical cross-section and the particle is almost invisible to the external field ($C_{\text{abs}} = 0.47$, $C_{\text{sca}} = 0.03$). Most of the powerflow lines pass by the nanoparticle and only handful of them terminate at the particle, indicating small losses. In the case depicted in Figure 2.8(b) the absorption cross-section approaches the plasmon resonance ($C_{\text{abs}} = 3.6$, $C_{\text{sca}} = 0.24$). Many flow-lines terminate at the nanoparticle (entering it from the front and the back, as in a similar case considered in [41]), indicating high losses.

As the particle bypasses the plasmon resonance (which can be identified by a maximum in values of the absorbtion and scattering cross-sections), the flow lines create vortex-like structures around the nanoparticle. Figures 2.8(c) and (d) show such vortices around a silver nanoparticle at wavelengths of 354 nm (where $\varepsilon = -2.0 + i0.28$, $C_{\text{abs}} = 5.8$ and $C_{\text{sca}} = 1.8$) and 367 nm (where $\varepsilon = -2.71 + i0.25$, $C_{\text{abs}} = 4.1$ and $C_{\text{sca}} = 2.0$). These latter two pictures represent *inward* and *outward* vortices which lie in the plane of incident polarization. The calculations show that in this central cross-section, light in the vortex remains linearly polarized in the plane of incidence. In the vortex regime the energy flow is dramatically disturbed in the vicinity of the particle. For the outward vortex, energy flow lines

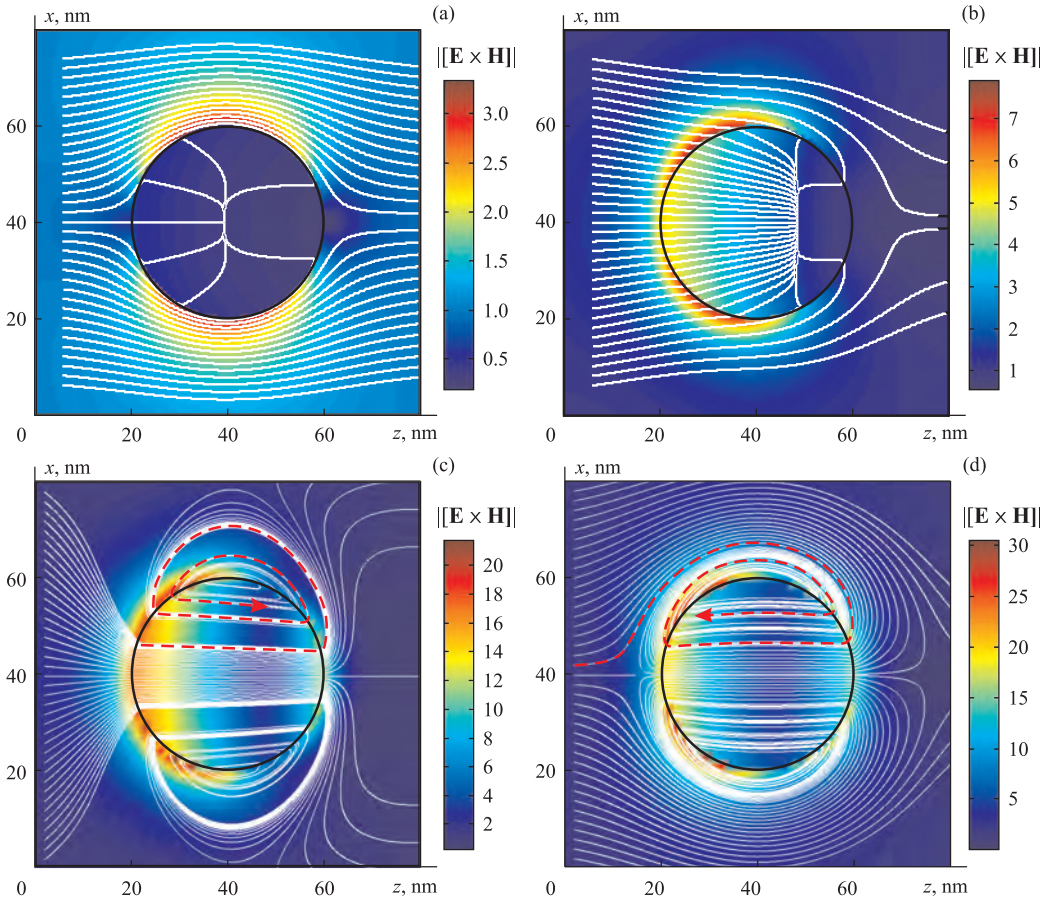

Figure 2.8: Mie Theory: powerflow distribution around a spherical nanoparticle with a radius of approximately 20 nm ($\lambda/r = 20$) in the plane containing the directions of propagation (from left to right) and polarization of the incident light. The colors indicate the absolute value of the Poynting vector, the white lines show the direction of powerflow. (a) $\varepsilon = -2.0 + i10.0$, $\lambda = 400$ nm; (b) $\varepsilon = -2.0 + i1.0$, $\lambda = 400$ nm; (c) $\varepsilon = -2.0 + i0.28$ — the dielectric coefficient of silver at $\lambda = 354$ nm. Red dashed lines indicate outward vortex structure; (d) $\varepsilon = -2.71 + i0.25$ — the dielectric coefficient of silver at $\lambda = 367$ nm. Red dashed lines indicate inward vortex structure [77].

inside the particle go along the direction of the incident wave and are nearly parallel to it. Outside the particle energy moves in the opposite direction — the energy flow lines bend around the particle and re-enter it again. The situation is reversed for the inward vortex. Here, the energy flow inside the particle is in the direction opposite to the incident wave, while the energy flow outside the nanoparticle is mainly in the direction of the incident wave. In the plane perpendicular to the plane of polarization the powerflow lines exhibit no spiral features.

The parameter field for both vortex regimes has been mapped for a hypothetical $r \approx 20$ nm nanoparticle ($\lambda/r = 20$) in the vicinity of its plasmon resonance by varying real and imaginary parts of the particle's dielectric constant ε' and ε'' (Fig. 2.9).

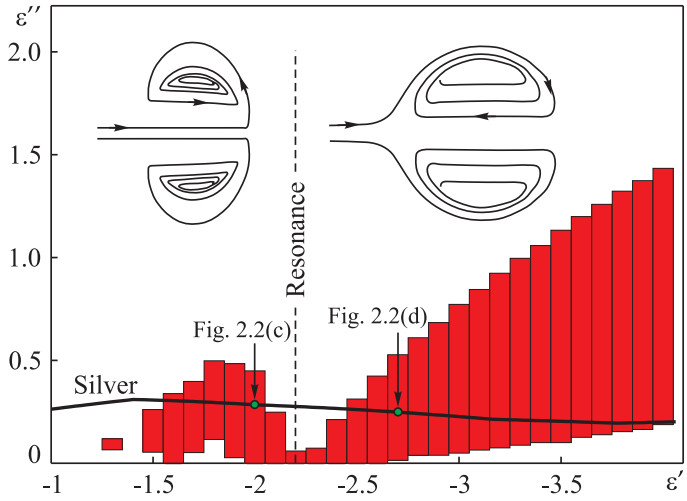

Figure 2.9: Map showing values of the real and imaginary parts of the dielectric constant (in red) at which vortex field structures appear. The dashed line at $\varepsilon' \sim -2.2$ indicates the position of the plasmon resonance in a spherical nanoparticle with $r \approx 20$ nm ($\lambda/r = 20$). The solid lines show the dispersion characteristics of the dielectric properties of silver.

Outward vortices are seen to the "left" of the the plasmon resonance i.e. for $\varepsilon' > -2.2$ (in a spherical nanoparticle with a radius of 20 nm the plasmon resonance occurs at $\varepsilon' \sim -2.2$). In the second type of vortex, denoted as an inward vortex, the powerflow lines pass around the sides of the particle before

turning towards the centerline and entering the particle to begin their spiral trajectory. Outward vortexes are seen to the "right" of the the plasmon resonance i.e. for $\varepsilon' < -2.2$.

Optical whirlpool-like vortices can be excited on nanoparticles made out of real metals (the solid black line in Figure 2.9 depicts $\varepsilon''(\varepsilon')$ dependence for silver). Therefore, silver 20 nm oblate spheroidal nanoparticles should support both inward and outward vortices in the upper ultra-violet and visible range of wavelengths.

The process of the generation of the inward vortex, conversion into outward vortex and disappearance of the vortex regime was demonstrated on a series of simulations of light interaction with a virtual $\lambda/20$-radius nanoparticle with constant imaginary part of the dielectric coefficient $\varepsilon'' = 0.1$ and real part ranging from $\varepsilon' = -1$ to -3.8 with $d\varepsilon' = 0.01$ step. The main stages of this process are depicted in Figure 2.10 using powerflow streamlines and intensity distribution. As one can see from the parameter field for the vortex regimes (Fig. 2.9), such variation in the real part of the dielectric constant of the nanoparticle allows tracing the first stages of generation of the inward vortex regime (Fig. 2.10a, b), its development through the plasmon resonance of the nanoparticle at $\varepsilon' = -2.2$ (Fig. 2.10c, d), conversion of the inward vortex regime into outward (Fig. 2.10e), and disappearance of the vortex regime with growing magnitude of $|\varepsilon'|$ (Fig. 2.10f). The number and position of the starting points for the calculations of the steamlines were kept the same.

The powerflow streamlines and intensity distributions calculated for $\varepsilon' = -1 \ldots -3.8$ with $d\varepsilon' = 0.01$ were composed into a video file available online as a supplementary material to the original publication [31] on Optics Express website: http://www.opticsexpress.org/abstract.cfm?id=85768. The video file shows the smooth transition between the excited regimes with changing ε', and the powerflow streamline and intensity distributions in Figure 2.10 represent snapshots from this video.

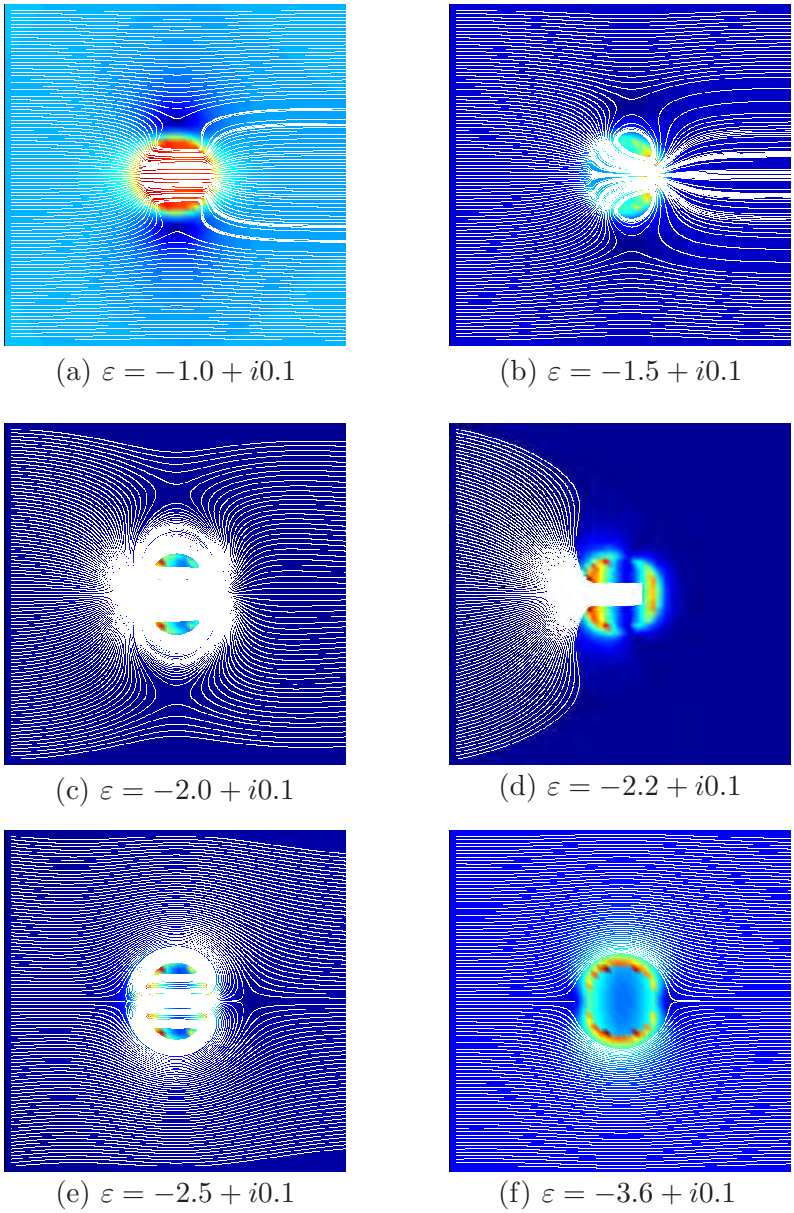

(a) $\varepsilon = -1.0 + i0.1$ (b) $\varepsilon = -1.5 + i0.1$

(c) $\varepsilon = -2.0 + i0.1$ (d) $\varepsilon = -2.2 + i0.1$

(e) $\varepsilon = -2.5 + i0.1$ (f) $\varepsilon = -3.6 + i0.1$

Figure 2.10: Power flow streamlines and intensity distributions showing evolution of optical whirlpool structure on a virtual $\lambda/20$-radius nanoparticle with $\varepsilon' = -1 \ldots -3.8$ and $\varepsilon'' = 0.1$: first stages of generation of the inward vortex regime (a, b), its development through the plasmon resonance (c, d), conversion of the inward vortex regime into outward (e) and and disappearance of the vortex regime (f). Video clip showing whole transition for $\varepsilon' = -1 \ldots -3.8$ with $d\varepsilon' = 0.01$ step is available online as a supplementary material to the original publication [31].

It has therefore been shown that a homogeneous nanoparticle of spherical shape possesses four interconnected regimes of excitation by linear polarized monochromatic electromagnetic radiation in the vicinity of its plasmon resonance: weak interaction, high-loss regime, and the creation of both outward and inward whirlpool-like vortices on the nanoparticle. The case of an oblate metallic spheroidal nanoparticles with a semiaxis ratio of 2 is considered in the following Section.

2.6 Excitation of optical whirlpools on metallic oblate spheroidal particles

Non-spherical nanoparticles are of considerable interest for applications because flattened or elongated shapes tend to reduce the plasmon resonance frequency, moving it from the blue-UV part of the spectrum to the more accessible visible-IR range. Mie theory is unsuitable (without major modifications [18, 78]) for objects without spherical symmetry, but numerical techniques, such as Finite Element method, provide an alternative to the analytical approaches and allow consideration of vortex fields around complex nanostructures.

In this section a homogeneous oblate (pancake-shaped) spheroidal nanoparticle with an aspect ratio of 2 was investigated by finite element method. It was shown that vortex fields can also exist near non-spherical nano-objects. Figure 2.11 shows the modification of the field structure around a spheroidal nanoparticle for different values of ε''. Here again, the weak interaction regime in Figure 2.11(a) ($C_{\text{abs}} = 0.42$, $C_{\text{sca}} = 0.02$), the high-loss regime in Figure 2.11(b) ($C_{\text{abs}} = 3.7$, $C_{\text{sca}} = 0.3$), the creation of outward vortexes in Figure 2.11(c) ($C_{\text{abs}} = 8.7$, $C_{\text{sca}} = 2.9$), and the creation of inward vortexes in Figure 2.11(d) ($C_{\text{abs}} = 2.9$, $C_{\text{sca}} = 1.3$) can be seen. Compared to optical whirlpool-like vortices on a spherical nanoparticle, vortices on oblate spheroid are much more pronounced due to high localization of fields at the edges of the spheroid, and larger cross sections. As for the spheres, the simulations predict the excitation of inward and outward vortices on silver nanoparticles of similar size.

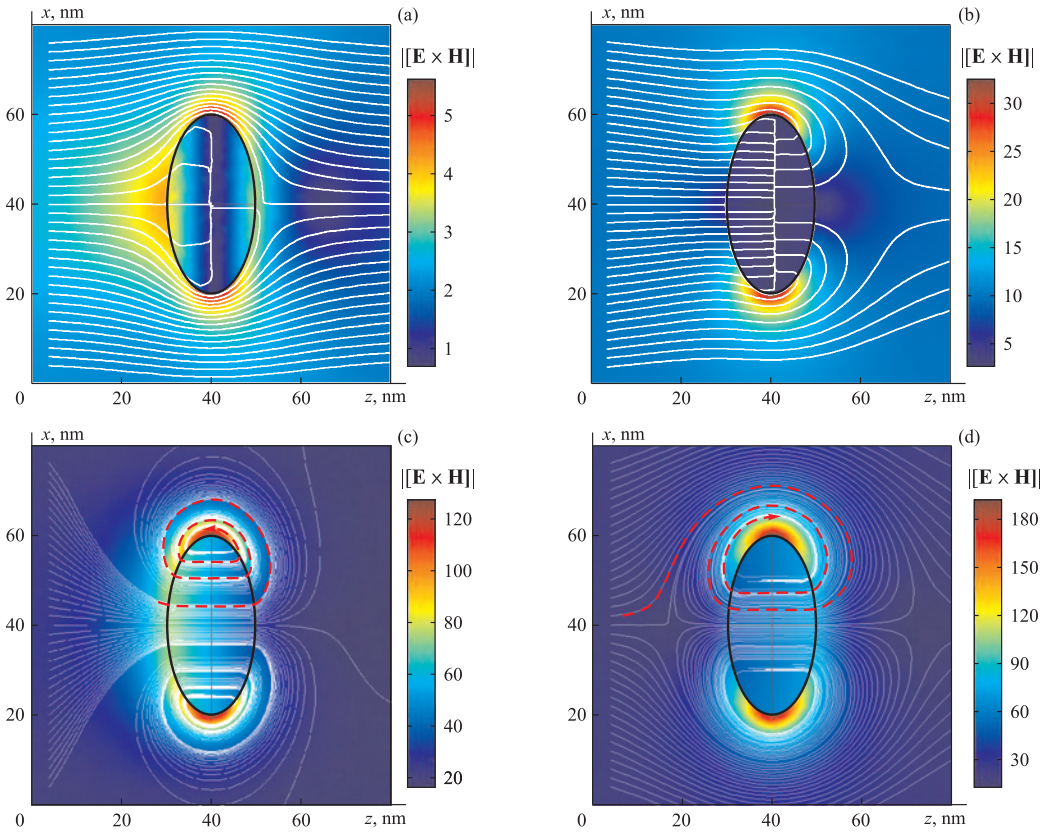

Figure 2.11: Finite element modelling: powerflow distribution around an oblate spheroidal nanoparticle (with a semi-major axial radius of approximately 20 nm ($\lambda/r = 20$) and an aspect ratio of 2 in the plane containing the directions of propagation (from left to right) and polarization of the incident light. The colors indicate the absolute value of the Poynting vector, the white lines show the direction of powerflow. (a) $\varepsilon = -3.52 + i10.0$, $\lambda = 400$ nm; (b) $\varepsilon = -3.52 + i1.0$, $\lambda = 400$ nm; (c) $\varepsilon = -3.37 + i0.2$ — the dielectric coefficient of silver at $\lambda = 380$ nm. Red dashed lines indicate outward vortex structure; (d) $\varepsilon = -4.0 + i0.2$ — the dielectric coefficient of silver at $\lambda = 392$ nm. Red dashed lines indicate inward vortex structure [77].

2.7 Summary and conclusions

Theoretical apparatus, based on Mie theory and Finite Element method, for study of optical properties of nanoparticles in the vicinity of the plasmon resonance, has been developed. Full three dimensional analytical solution of Maxwell's equations, based on Mie theory, for monochromatic linear polarized light scattering and absorption on a sphere of arbitrary size and material has been implemented. Computational domain with zero-reflection Perfectly Matched boundary conditions based on Finite Element method allowing free-space simulations of monochromatic linear polarized light scattering and absorption by objects of arbitrary material and complex geometry has been developed.

A series of calculations performed on single metallic spheres and oblate spheroids have established four different types of monochromatic linear polarized light interaction with a homogeneous spherical particle in the vicinity of its plasmon resonance: weak interaction (most of the powerflow lines bypass the particle, optical cross sections are much lower than the geometrical cross section), high-loss regime (significant amount of powerflow lines enter the particle from behind, optical cross section exceed geometrical cross section), creation of outward (powerflow lines penetrate the particle near its centerline then, on exiting the particle, the flow-lines turn away from the centerline and enter a spiral trajectory) and inward (powerflow lines pass around the sides of the particle before turning towards the centerline and entering the particle to begin their spiral trajectory) whirlpool-like vortices on the nanoparticle.

A parameter field for each type of vortex in case of light scattering on spherical nanoparticle has been established. It was found that outward vortices exist for wavelengths shorter than the plasmon resonance while inward vortices are excited on wavelengths longer that the plasmon resonance. It was also demonstrated that both types of vortices may exist on silver 20 nm nanoparticles in the upper ultra-violet and visible range of wavelengths.

There are a number of intriguing questions that may be asked in relation to the nanoscale structuring of the energy flow near and inside the nanoparticle. For instance, a vortex structure with light passing through

a nanoparticle several times backwards and forwards, resembles a standing wave in a dissipative Fabry-Perot resonator. One may therefore wonder if such a "nano-resonator" could provide conditions for a hysteresis and bistability in the nanoparticle's optical response if its dielectric properties depend on the intensity of light. The experimental observation of such hysteresis behavior would be clear evidence of the vortex energy flow. The existence of vortex structures in nanoparticles could provide a graphical interpretation of the fact that the absorbtion cross-section of a particle can be much bigger that its geometrical cross-section. When a vortex is created, powerflow lines pass through the nanoparticle several times, "multiplying" the light-matter interaction and generating the high energy losses associated with the large optical cross-section. Accurate phase and group delay measurements of light interacting with a nanoparticle near its plasmon resonance might provide further evidence for the long interaction time and thus for the existence of a vortex structure on the particle. It would also be very interesting to study the propagation of a narrow-band pulses through a media composed of spheres in one of the optical whirlpool regimes, especially time-delay and shape change of such pulses. The study should reveal even more interesting features of the interaction of light and resonance particles at the nanoscale.

The suggested theoretical approach can be further developed and improved, in particular by tracking the phase of the field components along a powerflow line in a vortex structure; introducing nonlinear materials; implementing layered and multiobject structures into the model; and introducing light with polarisation other than linear. The latter applied to shell structures can be used to design plasmonic and metamaterial structures with recently discovered extraordinary properties such as transparency and cloaking [79, 80].

Following the original publication [31] optical and microwave whirlpool-like vortices have been found at resonance conditions in meta-material fish-scale structures [81], chiral apertures [82], thin nanowires [83], microwave rectangular waveguide cavities [84] and ferrite disc particles [85], presented in Figure 2.12. The subject of optical whirlpools was further developed by the group of Professor Luk'yanchuk [86–88].

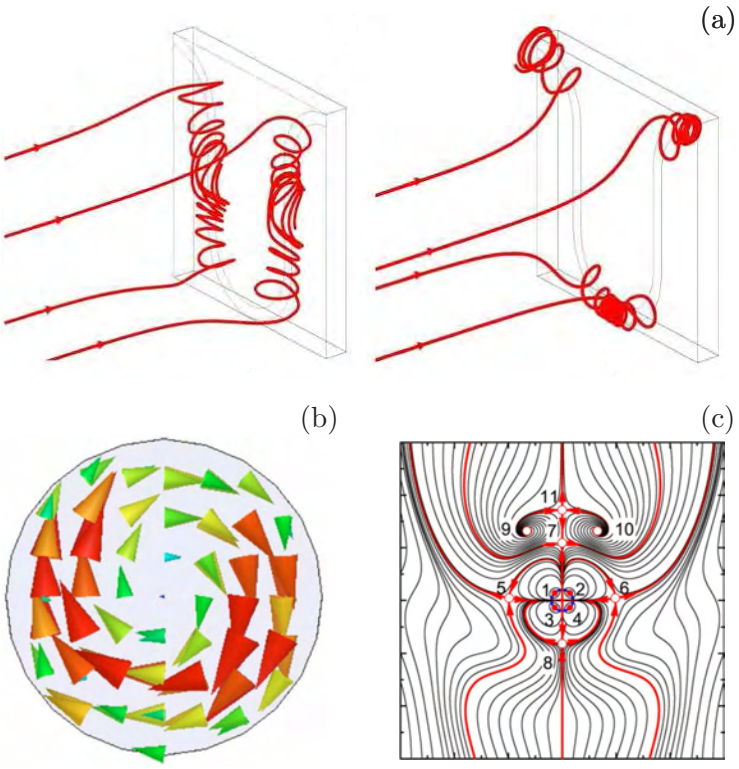

Figure 2.12: Whirlpool vortex-like structures found in different media: (a) microwave powerflow lines on metamaterial fish scale structures [81], (b) microwave Poynting vector distribution inside a ferrite disk [84], (c) optical Poynting vector field in the vicinity of the quadrupole resonance [88].

2.8 References

[1] K. Kneipp, Y. Wang, H. Kneipp, L.T. Perelman, I. Itzkan, R.R. Dasari, and M.S. Feld. Single molecule detection using surface-enhanced Raman scattering (SERS). *Phys. Rev. Lett.*, 78(9):1667, 1997.

[2] D.A. Genov, A.K. Sarychev, V.M. Shalaev, and A. Wei. Resonant field enhancements from metal nanoparticle arrays. *Nano Lett.*, 4(1):153, 2004.

[3] P. Olk, J. Renger, T. Hartling, M.T. Wenzel, and K.M. Eng. Two particle enhanced nano raman microscopy and spectroscopy. *Nano Lett.*, 7(6):1736, 2007.

[4] G. Gouadec and P. Colomban. Raman spectroscopy of nanostructures and nanosized materials. *J. Raman Spec.*, 38(6):598, 2007.

[5] B.F. Soares, M.V. Bashevoy, F. Jonsson, K.F. MacDonald, and N.I. Zheludev. Polymorphic nanoparticles as all-optical memory elements. *Opt. Express*, 14(22):10652, 2006.

[6] N.I. Zheludev. Single nanoparticle as photonic switch and optical memory element. *J. Opt. A*, 8(4):S1, 2006.

[7] B.F. Soares, F. Jonsson, and N.I. Zheludev. All-optical phase-change memory in a single gallium nanoparticle. *Phys. Rev. Lett.*, 98(15):153905, 2007.

[8] M. Quinten, A. Leitner, J.R. Krenn, and F.R. Aussenegg. Electromagnetic energy transport via linear chains of silver nanoparticles. *Opt. Lett.*, 23(17):1331, 1998.

[9] M.L. Brongersma, J.W. Hartman, and H.A. Atwater. Electromagnetic energy transfer and switching in nanoparticle chain arrays below the diffraction limit. *Phys. Rev. B*, 62(24):R16 356, 2000.

[10] N.F. van Hulst. Light in chains. *Nature*, 448:141, 2007.

[11] S.A. Maier, M.L. Brongersma, P.G. Kik, S. Meltzer, A.A.G. Requicha, and H.A. Atwater. Plasmonics — a route to nanoscale optical devices. *Adv. Mat.*, 13(19):1501, 2001.

[12] J.B. Pendry. Negative refraction makes a perfect lens. *Phys. Rev. Lett.*, 85(18):3966, 2000.

[13] R.W. Ziolkowski and A.D. Kipple. Application of double negative materials to increase the power radiated by electrically small antennas. *IEEE Trans. Ant. Prop.*, 51(10):2626, 2003.

[14] J.D. Baena, L. Jelinek, R. Marques, and F. Medina. Near-perfect tunneling and amplification of evanescent electromagnetic waves in a waveguide filled by a metamaterial: theory and experiments. *Phys. Rev. B*, 72(7):075116, 2005.

[15] M.L. Brongersma. Nanoshells: gifts in a gold wrapper. *Nat. Mat.*, 2:296, 2003.

[16] J.C. Riboh, A.J. Haes, A.D. McFarland, C.R. Yonzon, and R.P. Van Duyne. A nanoscale optical biosensor: real-time immunoassay in physiological buffer enabled by improved nanoparticle adhesion. *J. Phys. Chem. B*, 107(8):1772, 2003.

[17] A.J. Haes, S.L. Zou, G.C. Schatz, and R.P. Van Duyne. A nanoscale optical biosensor: the long range distance dependence of the localized surface plasmon resonance of noble metal nanoparticles. *J. Phys. Chem. B*, 108(1):109, 2004.

[18] H.C. van der Hulst. *Light scattering by small particles.* Wiley, New York, 1983.

[19] H.F. Schouten, T.D. Visser, and D. Lenstra. Optical vortices near sub-wavelength structures. *J. Opt. B*, 6:S404, 2004.

[20] M. Padgett and L. Allen. Light with a twist in its tail. *Contemp. Phys.*, 41(5):275, 2000.

[21] N.R. Heckenberg, R. McDuff, C.P. Smith, H. Rubinsztein-Dunlop, and M.J. Wegener. Laser beams with phase singularities. *Opt. Quant. Electr.*, 24(9):S951, 1992.

[22] W. Braunbek and G. Laukien. Features of refraction by a semi-plane. *Optik*, 9:174, 1952.

[23] N.D. Mermin. The topological theory of defects in ordered media. *Rev. Mod. Phys.*, 51:591, 1979.

[24] J.F. Nye and M.V. Berry. Dislocations in wave trains. *Proc. Royal Soc. Lond. Ser. A*, 336(1605):165, 1974.

[25] J.F. Nye. *Natural focusing and the fine structure of light.* Bristol: Institute of Physics Publishing, 1999.

[26] M.S. Soskin and M.V. Vasnetsov. Singular optics. *Progr. Opt.*, 42:219, 2000.

[27] L. Allen, S.M. Barnett, and M.J. Padgett. *Optical angular momentum.* Bristol: Institute of Physics Publishing, 2003.

[28] M.V. Berry. Exuberant interference: rainbows, tides, edges, (de)coherence... *Phil. Trans. Royal Soc. Lond.*, 360(1794):1023, 2002.

[29] M.V. Berry, M. Dennis, and M. Soskin. Special issue on singular optics. *J. Opt. A*, 6(5):S155, 2004.

[30] R. Pugatch, M. Shuker, O. Firstenberg, A. Ron, and N. Davidson. Topological stability of stored optical vortices. *Phys. Rev. Lett.*, 98:203601, 2007.

[31] M.V. Bashevoy, V.A. Fedotov, and N.I. Zheludev. Optical whirlpool on an absorbing metallic nanoparticle. *Opt. Express*, 13(21):8372, 2005.

[32] H.F. Schouten, T.D. Visser, G. Gbur, D. Lenstra, and H. Blok. The diffraction of light by narrow slits in plates of different materials. *J. Opt. A*, 6:S277, 2004.

[33] Z.B. Wang, B.S. Luk'yanchuk, M.H. Hong, Y. Lin, and T.C. Chong. Energy flow around a small particle investigated by classical Mie theory. *Phys. Rev. B*, 70:035418, 2004.

[34] G. Mie. Beitrage zur optik truber medien, speziell kolloida ler metallosungen. *Annal Physik*, 25:377, 1908.

[35] N.A. Logan. Early history of the Mie solution. *J. Opt. Soc. Am.*, 52:342, 1962.

[36] N.A. Logan. Survey of some early studies of the scattering of plane waves by a sphere. *Proc. IEEE*, 53(8):773, 1965.

[37] A. Clebsch. Ueber die reflexion an einer kugelflache. *J. fur Math.*, 61:195, 1863.

[38] L. Lorenz. Sur la lumiére réfléchie et réfractée par une sphére transparente. *Vidensk. Selsk. Skrifter*, 6:1, 1980.

[39] J.A. Stratton. *Electromagnetic theory*. John Wiley & Sons, 2007.

[40] M. Born and E. Wolf. *Principles of optics: electromagnetic theory of propagation, interference and diffraction of light*. Cambridge University Press, 1999.

[41] C.F. Bohren and D.R. Huffman. *Absorption and scattering of light by small particles*. Wiley, New York, 1983.

[42] J.V. Dave. Scattering of visible light by large water spheres. *Appl. Opt.*, 8(1):155, 1969.

[43] P.L. Marston and D.S. Langley. Glory in backscattering: Mie and model predictions for bubbles and conditions on refractive index in drops. *J. Opt. Soc. Am.*, 72(4):456, 1982.

[44] P. Laven. Simulation of rainbows, coronas, and glories by use of Mie theory. *Appl. Opt.*, 42(3):436, 2003.

[45] P. Laven. How are glories formed? *Appl. Opt.*, 44(27):5675, 2005.

[46] C. Sonnichsen, T. Franzl, T. Wilk, G. von Plessen, and J. Feldmann. Plasmon resonances in large noble-metal clusters. *New J. Phys.*, 4:93.1, 2002.

[47] J.R. Krenn, A. Dereux, J.C. Weeber, E. Bourillot, Y. Lacroute, J.P. Goudonnet, G. Schider, W. Gotschy, A. Leitner, and F.R. Aussenegg. Squeezing the optical near-field zone by plasmon coupling of metallic nanoparticles. *Phys. Rev. Lett.*, 82(12):2590, 1999.

[48] H.C. Martin and G.F. Carey. *Introduction to finite element analysis: theory and application*. New York: McGraw-Hill, 1973.

[49] D.H. Norrie and G. de Vries. *The finite element method: fundamentals and applications*. New York: Academic Press, 1973.

[50] G. Strang and G.J. Fix. *An Analysis of the Finite Element Method*. Englewood Cliffs, NJ: Prentice-Hall, 1973.

[51] O. Axelsson and V.A. Barker. *Finite element solution of boundary-value problems: theory and computation*. New York: Wiley, 1984.

[52] K.H. Huebner, E.A. Thornton, and T.G. Byrom. *The finite element method for engineers*. New York: Wiley, 1995.

[53] R.D. Cook, D.S. Malkus, M.E. Plesha, and R.J. Witt. *Concepts and applications of finite element analysis*. John Wiley & Sons, 2001.

[54] J. Jin. *The Finite Element Method in electromagnetics*. John Wiley and Sons, New York, 2002.

[55] J.T. Oden. *Historical comments on finite elements*. A History of Scientific and Numeric Computation. Addison-Wesley, Reading, 1989.

[56] K. Schellbach. Probleme der variationsrechnung. *J. Reine Angew. Math*, 41:293, 1851.

[57] T. Rado. On Plateau's problem. *Ann. of Math.*, 31(2):457, 1930.

[58] J. Douglas. Solution of the problem of Plateau. *Trans. Amer. Math. Soc.*, 33(1):263, 1931.

[59] H. Hrennikoff. Solutions of problems in elasticity by the framework method. *J. Appl. Mech.*, 8:A169, 1941.

[60] R. Courant. Variational methods for the solution of problems of equilibrium and vibration. *Bull. Am. Math. Sot.*, 49:1, 1943.

[61] J.T. Oden. *Some contibutions to the mathematical theory of mixed finite element approximations*. Univ. of Tokyo Press, Tokyo, 1972.

[62] COMSOL. *Comsol multiphysics: model library*, 1994–2005.

[63] S.G. Mikhlin. *Variational methods in mathematical physics*. New York, Macmillian, 1964.

[64] J.M. Jin and W.C. Chew. Combining PML and ABC for the finite-element analysis of scattering problems. *Microwave and Opt. Tech. Lett.*, 12(4):192, 1996.

[65] B. Engquist and A. Majda. Absorbing boundary-conditions for numerical-simulation of waves. *Math. Comp.*, 31(139):629, 1977.

[66] A. Bayliss, M. Gunzburger, and E. Turkel. Boundary-conditions for the numerical-solution of elliptic-equations in exterior regions. *SIAM J. Appl. Math.*, 42(2):430, 1982.

[67] T.G. Moore, J.G. Blaschak, A. Taflove, and G.A. Kriegsmann. Theory and application of radiation boundary operators. *IEEE J. Trans. Ant. Prop.*, 36(12):1797, 1988.

[68] J.M. Jin, J.L. Volakis, and V.V. Liepa. An engineer's approach for terminating finite element meshes in scattering analysis. *Ant. Propag. Soc. Int. Symp.*, 2:1216, 1991.

[69] J.P. Berenger. A perfectly matched layer for the absorption of electromagnetic waves. *J. Comp. Phys.*, 114(2):185, 1994.

[70] W.C. Chew and W.H. Weedon. A 3D perfectly matched medium from modified Maxwell's equations with stretched coordinates. *Microwave Opt.Tech. Lett.*, 7(13):599, 1994.

[71] Z.S. Sacks, D.M. Kingsland, R. Lee, and J.F. Lee. A perfectly matched anisotropic absorber for use as an absorbing boundary condition. *IEEE Trans. Ant. Prop.*, 43(12):1460, 1995.

[72] T.A. Davis and I.S. Duff. An unsymmetric-pattern multifrontal method for sparse LU factorization. *SIAM J. Matrix Anal. App.*, 18(1):140, 1997.

[73] T.A. Davis and I.S. Duff. A combined unifrontal/multifrontal method for unsymmetric sparse matrices. *ACM Trans. Math. Softw.*, 25(1):1, 1999.

[74] T.A. Davis. Algorithm 832: UMFPACK — an unsymmetric-pattern multifrontal method. *ACM Trans. Math. Softw.*, 30(2):196, 2004.

[75] M. Dorobantu. Efficient streamline computations on instructured grids. *Department of Numerical Analysis and Computing Science, Royal Institute for Technology, Stockholm*, 1997.

[76] D.N. Kenwright and G.D. Mallinson. A 3-D streamline tracking algorithm using dual stream functions. In *VIS '92: Proceedings of the 3rd conference on Visualization '92*, pages 62–68, Los Alamitos, CA, USA, 1992. IEEE Computer Society Press.

[77] R. Lide. *Handbook of chemistry and physics*. CRC Press, New York, 2000.

[78] F.V. Schultz. Studies in radar cross sections I: Scattering by prolate spheroid. *Willow Run Research Center, Univ. of Michigan Press*, 1950.

[79] A. Alu and N. Engheta. Erratum: Achieving transparency with plasmonic and metamaterial coatings. *Phys. Rev. E*, 73(1):019906, 2006.

[80] A. Alu and N. Engheta. Cloaking and transparency for collections of particles with metamaterial and plasmonic covers. *Opt. Express*, 15(12):7578, 2007.

[81] V.A. Fedotov, P.L. Mladyonov, S.L. Prosvirnin, and N.I. Zheludev. Planar electromagnetic metamaterial with a fish scale structure. *Phys. Rev. E*, 72(5):056613, 2005.

[82] A.V. Krasavin, A.S. Schwanecke, and N.I. Zheludev. Extraordinary properties of light transmission through a small chiral hole in a metallic screen. *J. Opt. A*, 8(4):S98–S105, 2006.

[83] B.S. Luk'yanchuk and V. Ternovsky. Light scattering by a thin wire with a surface-plasmon resonance: bifurcations of the Poynting vector field. *Phys. Rev. B*, 73(23):235432, 2006.

[84] E.O. Kamenetskii, M. Sigalov, and R. Shavit. Microwave whirlpools in a rectangular waveguide cavity with a thin ferrite disk. *Phys. Rev. E*, 74(3):036620, 2006.

[85] E.O. Kamenetskii. Vortices and chirality of magnetostatic modes in quasi-2D ferrite disc particles. *J. Phys. A*, 40(24):6539, 2007.

[86] B.S. Luk'yanchuk, Z.B. Wang, M. Tribelsky, V. Ternovsky, M.H. Hong, and T.C. Chong. Peculiarities of light scattering by nanoparticles and nanowires near plasmon resonance frequencies. *J. Phys.*, 59:234, 2006.

[87] B.S. Luk'yanchuk, M.I. Tribelsky, Z.B. Wang, Y. Zhou, M.H. Hong, L.P. Shi, and T.C. Chong. Extraordinary scattering diagram for nanoparticles near plasmon resonance frequencies. *Appl. Phys. A*, 89(2):259, 2007.

[88] B.S. Luk'yanchuk, M.I. Tribelsky, V. Ternovsky, Z.B. Wang, M.H. Hong, L.P. Shi, and T.C. Chong. Peculiarities of light scattering by nanoparticles and nanowires near plasmon resonance frequencies in weakly dissipating materials. *J. Opt. A*, 9:S294, 2007.

Chapter 3

Generation of traveling surface plasmon waves by free-electron impact

3.1 Synopsis

It has been found that the injection of a beam of free electrons into an unstructured gold surface creates a highly localized source of surface plasmon polaritons. The plasmons were detected by a controlled decoupling into light with a grating at a set distance from the excitation point.

In Section 3.3 a detailed overview of the cathodoluminescence phenomenon and the experimental technique for probing the optical properties of nanostructures with an electron beam, based on a scanning electron microscope with cathodoluminescence light collection system and a spectrum analyzer, is presented. In the following Section, the theoretical description of surface plasmon polaritons (SPPs) and the process of decoupling by a grating are detailed. A series of experiments demonstrating the excitation of SPPs on a metallic grating, is presented in Section 3.5. The generation of traveling surface plasmon polariton waves with a beam of free electrons on an unstructured metal surface, their propagation and controlled decoupling into light by a grating are detailed in Section 3.6. In the following Section, the mechanism of SPP generation with an electron beam, the power, efficiency and localization of the plasmon source are discussed.

3.2 Introduction

Surface plasmon polaritons (SPPs) are coupled transverse electromagnetic field and charge density oscillations which propagate along the interface between a conductor and a dielectric medium [1–5]. The term "surface plasmon polariton" reflects the dual nature of this particular surface wave: a bound state between a coupled photon (polariton) and electron oscillation excitation (plasmon). On one hand, coupling of photons results in resonance oscillation of electrons on a surface of the conductor. On the other hand, the oscillating charges become the source of electromagnetic waves themselves. As a result, surface plasmon polaritons can have long propagation distances along a metal–dielectric interface, exceeding their wavelength by several orders of magnitude [6, 7]. The main feature of the SPPs that currently attracts attention is that they are strongly localized, making them favored candidates as information carriers in applications such as high-density broadband interconnections and signal processing [8, 9]. Recent developments in manufacturing of metal nanostructures [10–16] and studies of a wide range of plasmon-based optical elements such as passive waveguides [17–20], active switches [21] and biosensors [22–24] led to the notion of *plasmonics*, the science and technology of metal-based optics and nanophotonics [25].

Surface electromagnetic waves have now been studied for more than a century, starting with Sommerfeld's study of radio waves propagating along the surface of a single metal wire [26] and Zenneck's description of EM propagation on a flat metal surface [27]. In the visible domain, anomalous intensity drops in spectra produced when visible light reflects on metallic gratings were observed by Robert W. Wood [28–30]. The study was not connected with the earlier theoretical work until the middle of the last century [31]. Ten years later, in 1956, energy losses experienced by fast electrons traveling through metals were theoretically described by David Pines [32]. He attributed these losses to collective oscillations of free electrons in the metals. In analogy to earlier work on plasma oscillations of free electrons in gas discharges, he called these oscillations "plasmons." Coincidentally, in that same year Robert Fano introduced the term "polariton" for the coupled oscillation of

bound electrons and light inside transparent media [33]. The first theoretical description of surface plasmons was published by Rufus Ritchie in his study on electron energy losses in thin metal films [34], in which it is shown that plasmon modes can exist near the surface of metals. In 1968, nearly seventy years after Wood's original observations, Ritchie and coworkers describe the anomalous behavior of metal gratings in terms of surface plasmon resonances excited on the gratings [35]. Since then the subject of surface plasmons has experienced a ever growing interest from a wide variety of scientists and many methods of surface plasmon generation, as discussed below, have been developed.

The excitation of surface plasmon polaritons is usually performed by optical means, and since SPPs do not couple to light illumination at a flat metal-vacuum interface (as shown in Section 3.4), the energy coupling is achieved using gratings [35, 36] or prism matching schemes [37, 38]. Although this was a great achievement in the study of the surface plasmons that made experiments on surface plasmons easily accessible to many researchers, these techniques have two major disadvantages imposing limitations on their applicability these days: generated plasmons are poorly localized, and the created source of plasmons can not be repositioned. A breakthrough in the localization of optically excited SPPs came with the application of the near field optical microscope (SNOM) techniques [39–43]. The scattering, interference, backscattering and localization of the surface plasmon polaritons have been visualized and investigated directly on the surface [44–46]. Discontinuities of a plasmon waveguide, such as a nanoparticle or a nanowire [47] have been used to improve the localization of excited SPPs even further. Although localization of the SPP source provided by techniques using optical means have significantly improved over the years, these methods are cumbersome, and do not always allow for easy repositioning of the plasmon source.

Ritchie's theoretical predictions regarding the excitation of surface plasmons in metal foils by an electron beam were confirmed by experiments by Cedric J. Powell [48, 49], implicating the electron beam of a scanning or transmission electron microscope as a perspective source of surface plasmons. This connection however was not made straight away, and the research continued

with this original focus for decades. Excitation of surface plasmons on a structured surface, a sinusoidal silver grating, has been demonstrated [50, 51] by the study of angular dependence of spectra of induced radiation. The study has been followed by investigations into gratings of different profiles [52–56] and materials [57], and electron-induced light emission from rough surfaces [58–61] and nanoparticles [62, 63]. Recently evidence of propagating surface plasmon modes was observed in the spatial distribution of optical emission of a microscale gold corral under electron excitation in a scanning tunneling microscope [64].

The idea of using an electron beam as a source of propagating surface plasmon waves on an unstructured surface has been realized in the original research [65] detailed in this Chapter. It was shown that the injection of a beam of free electrons on the unstructured metal surface results in the creation of a surface plasmon polariton source with potentially nanoscale localization, which may be easily and dynamically repositioned anywhere within a plasmonic device. In the following Section the experimental technique for probing the optical properties of nanostructures and excitation of surface plasmon polaritons with an electron beam, is presented.

3.3 Probing the optical properties of nanostructures with an electron beam

In this Section, the introduction to the phenomenon of light emission by solids as a result of electron bombardment, known as cathodoluminescence, and an outline of the vital components necessary for the implementation of an experimental system for the probing of the optical properties of nanostructures with an electron beam, is presented. The components, motivation for the selection of components, and principles of operation of the developed experimental technique, based on a scanning electron microscope with a modified cathodoluminescence system, are described. Performance estimations of the experimental setup, such as a spectral calibration curve, quantum efficiency and spatial resolution, and improvements of the system are discussed in detail.

3.3.1 Light emission from solids induced by an electron beam

The optical response of a metal film to the bombardment with free electrons is described by a general term *cathodoluminescence* [66]. This phenomenon, first reported in the middle of the nineteenth century, was observed during experiments on electrical discharges in evacuated glass tubes, which exhibit luminescence when cathode rays struck the glass. In fact, the observation of luminescence due to cathode ray bombardment led Sir Joseph John "J.J." Thomson (1856–1940) to the discovery of the electron and the determination of its charge-to-mass ratio. Other luminescence phenomena, such as, photoluminescence, have been known and studied for much longer, since they do not require a vacuum and concentrated sources of electrons, which are not readily available in the terrestrial environment. With the development of electron microscopy techniques in recent decades, cathodoluminescence has emerged as an important microcharacterization tool for the analysis of luminescent materials.

In an electron probe instrument, electron irradiation of a solid results in a variety of useful signals (Fig. 3.1). Primary (i. e. incident or beam) electrons may be backscattered from the specimen with little or no energy loss, or they lose energy to produce secondary electrons. Some primary electrons, absorbed in the bulk of the material, will dissipate their energy in various electronic excitations leading to the emission of characteristic x-rays; the generation of electron-hole pairs, which themselves may lead to the emission of photons in the ultraviolet, visible, and infrared spectral ranges (i. e. *cathodoluminescence*) or to various charge collection signals in devices; the generation of Auger electrons; and thermal effects, including electroacoustic (thermal wave) signals. In thin specimens, transmitted electrons may be scattered elastically (with no energy loss) or inelastically (with energy loss). All these processes lead to the formation of signals that can be used in the characterization of the structural, chemical, and electronic properties of the material.

The incident electron undergoes a successive series of elastic and inelastic scattering events in the material. As a result of these scattering events within the material, the original trajectories of the electrons are randomized and the energy of the electron beam is dissipated. The effective depth to which energy dissipation extends is known as the penetration range, which is much shorter than the total length of an individual electron's "random walk." The volume within which 95 % or so of the primary electrons are brought to rest is generally referred to as the *generation volume* (or excitation volume) that can be estimated analytically [67] or using Monte Carlo simulations [66, 68]. The approximate penetration range of 10–50 keV electrons bombarding a gold film is 0.3–4 μm respectively.

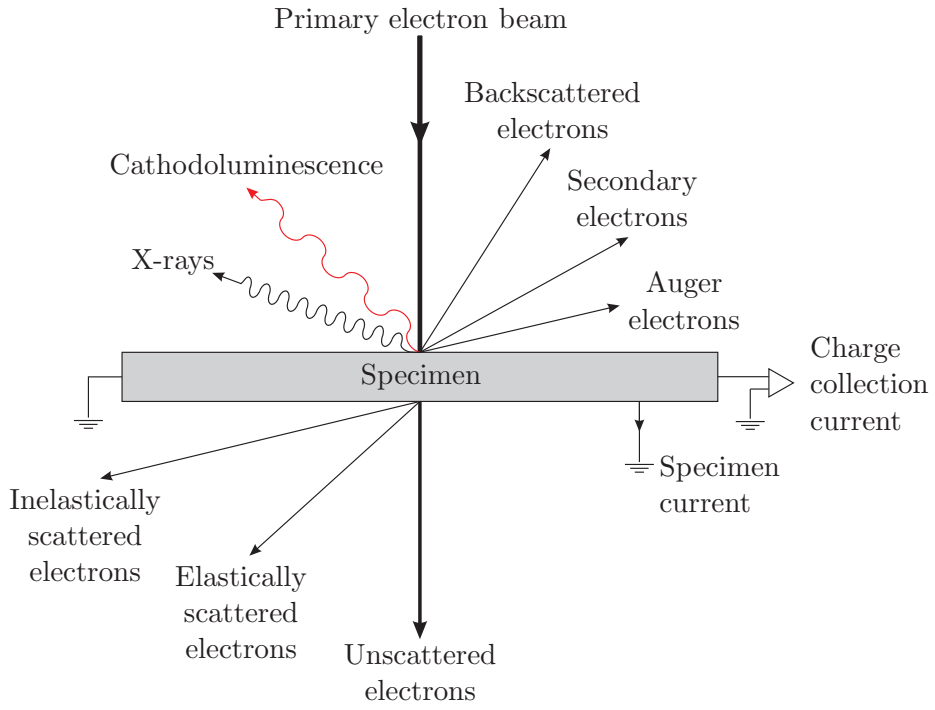

Figure 3.1: Schematic diagram of the types of interaction (or signal) available due to electron beam interactions with a solid [66].

Scanning electron microscopy (SEM) [68–70] and scanning transmission electron microscopy (STEM) [71–73] techniques are well suited for the microcharacterization of materials, since they provide high spacial resolution and the simultaneous availability of a variety of modes, such as x-ray

microanalysis; secondary (voltage contrast), backscattered, and transmitted electron images; scanning electroacoustic microscopy (SEAM); cathodoluminescence (CL) and charge collection signals. The last three modes constitute the electronic microcharacterization capability of the SEM (or STEM). Note that CL is unique among all the SEM modes in that it is the only contactless method that provides microcharacterization of the optical and electronic properties of luminescent materials. Nondestructive depth-resolved CL studies can be performed by varying the range of electron penetration, which depends on the electron beam energy, in order to excite CL from different depths in the material. Moreover, simple "flood illumination" electron bombardment can produce large total CL intensities, enabling higher spectral resolution to be attained. For this reason, a SEM intended for CL use should provide the largest possible maximum electron beam current (1 μA at least).

Cathodoluminescence offers a contactless and relatively "nondestructive" method for microcharacterization of luminescent materials. Some clarification of the term "nondestructive" is, however, required. Often an analysis is considered to be nondestructive if the physical integrity of the material remains intact. However, in certain cases electron irradiation may ionize or create defects and so alter the electronic properties of the material temporarily or permanently. Exposure of a sample to the electron beam in a scanning electron microscope, especially at high currents, results in the growth of an amorphous carbon film due to the decomposition of hydrocarbon molecules, which are always present in small quantities in the SEM chamber. This growth is induced mainly by secondary electrons backscattered by atoms of the sample. Therefore, long exposures will result in a "degradation" of the sample as the presence of the carbon film reduces the optical response from the solid. This unwanted effect of carbon film deposition was, however, used to demonstrate "nano-welding" of complex 3D objects with electron beam on a substrate [74].

The mechanisms leading to the emission of light in a solid are similar for different forms of the excitation energy. Cathodoluminescence and other luminescence phenomena, such as photoluminescence (PL), yield similar results with some possible differences associated with the details of the

excitation of electron-hole pairs, for example in the generation rate and excitation volume. Electron beam excitation in general leads to emission by *all* the luminescence mechanisms present in the solid. One of the fundamental differences between CL and PL is that, whereas a photon generates only one electron–hole pair, one 20-keV electron, for example, can generate thousands of electron–hole pairs in the generation volume, which is usually several microns in diameter. In order to clarify the specifics of the quantitative interpretation of the cathodoluminescence spectra, it is useful to compare it with another technique, utilizing the detection of electromagnetic radiation induced by a beam of electrons, the x-ray microanalysis.

Characteristic x-rays are emitted due to electronic transitions between sharp, inner-core levels (Fig. 3.2). The lines, therefore, are narrow, characteristic of the particular chemical element, and are unaffected by the environment of the atom in the lattice. In addition, there is a general rule for identifying the element using Moseley's law, which relates the frequency ν of an x-ray line to the atomic number Z ($\nu \sim Z^2$). The CL signal is formed by detecting photons of the ultraviolet, visible, and near-infrared regions of the spectrum. These photons are emitted as the result of electronic transitions between the conduction and valence bands and levels lying in the band gap of the material (Fig. 3.2).

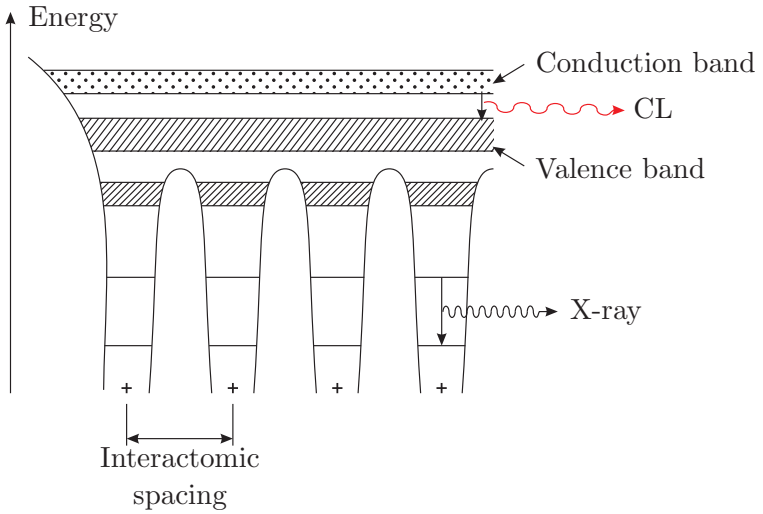

Figure 3.2: Energy band diagram of a one-dimensional lattice [66].

Many useful signals in these cases are due to transitions that involve impurities and a variety of defects. Therefore, there is no general rule, analogous to Moseley's law, that would serve to identify bands or lines in the CL spectrum. The influence of defects of the surface and various external perturbations, such as temperature, electric field, and stress, have to be considered in the analysis of the CL signal. Correction of CL signals for all the factors that may affect the emission of photons from a material is a formidable task compared with the analogous ZAF correction procedure for x-ray photons (the correction for the atomic number Z, the absorption A and fluorescence F). The ZAF correction can be easily performed in most cases using a computer. In comparison, quantitative CL analysis is still in its infancy because of the lack of any generally applicable theory for the wide variety of possible types of luminescence centers and radiative recombination mechanisms. In addition to these problems, luminescence can describe only radiative emission processes. Nonradiative recombination events, such as excitation of surface plasmon polaritons (SPP), can be deduced only from CL images, provided the contrast between radiative and nonradiative sites is sufficiently strong. However, the geometrical modification of the surface of a solid, for example, a diffraction grating, allows controlled energy transfer from the nonradiatively excited SPPs into electromagnetic radiation through the decoupling of surface plasmon polaritons into electromagnetic radiation.

To summarize, a comprehensive theoretical description of the luminescence centers and processes is complex, and thus presenting a unified theoretical description of quantitative CL analysis that can be correlated with experimental data at this junction is a formidable task. However, the cathodoluminescence technique measurements performed on a specially designed metal surface can reveal one of the nonradiative CL mechanisms of particular interest to this research — surface plasmon polaritons.

The excitation of light from a solid with a beam of electrons imposes certain conditions on the experimental setup aimed at the research of the subject. A scanning electron microscope (SEM) with high electron beam current and a wide range of energies is a favorable candidate for a base of the experimental setup allowing such measurements. As the cathodo-

luminescence is one of many energy channels to which the energy of the primary electron beam can be transferred to, the efficient light collection and analysis system is among the necessary requirements. The experiment setup according to the above mentioned requirements is described in the following Section.

3.3.2 SEM with modified CL system

The probing of the optical properties of a nanostructure with an electron beam consists of three main steps: *bombardment of the sample with the a beam of free electrons* of selected energy and current, *collection of induced radiation*, and *analysis*, i.e. acquisition and processing of the obtained spectra of the electron beam induced light emission from the nanostructure. Despite the wide variety of equipment available these days to fulfill each of these steps, the choice of the vital components for the system for the experiment, as outlined in the previous Section, is quite limited.

CamScan CS 3200 scanning electron microscope (SEM) with a LaB_6 cathode and a cathodoluminescence (CL) system was selected as a base of the experimental setup (Fig. 3.3). The electron beam generated by the SEM has a wide variety of accelerating voltages (1–50 keV) and very high beam currents (up to 15 μA). The original cathodoluminescence system of the SEM, consisting of a parabolic mirror for light collection from a sample, a transparent window in the SEM chamber and a photomultiplier was modified according to the task: the photomultiplier was replaced by a system of lenses, focusing collected light onto slits of a Horiba Jobin Yvon spectrum analyzer. The spectrum analyzer consists of a CP-140 monochromator and a Symphony 1024×256 pixels FIUV Liquid Nitrogen cooled CCD array (average quantum efficiency 40 %), allowing acquisition of spectra in 350–1150 nm region with exposure times up to 10 ms (Fig. 3.4).

The principle of the operation of the system is the following. The beam of electrons of the selected energy and current is generated at the top of the SEM column and directed by a system of magnetic lenses downwards into the chamber, onto the sample (Fig. 3.4a). The light resulting from the

bombardment of the sample with electrons is collected and analyzed by the *light collection system*: the parabolic mirror directs the light through the transparent window in the SEM chamber to the system of lenses, focusing it on the slits of the spectrum analyzer. The first part of the spectrum analyzer, the monochromator, expands the light into spectral components, with a specially designed grating, onto a 1024×256 CCD array (Fig. 3.4b). The image from the CCD array is averaged along the y-axis, giving the 1024 point spectrum of collected light. Specific details on generation, modes of operation of the electron beam and light collection by a parabolic mirror are given below.

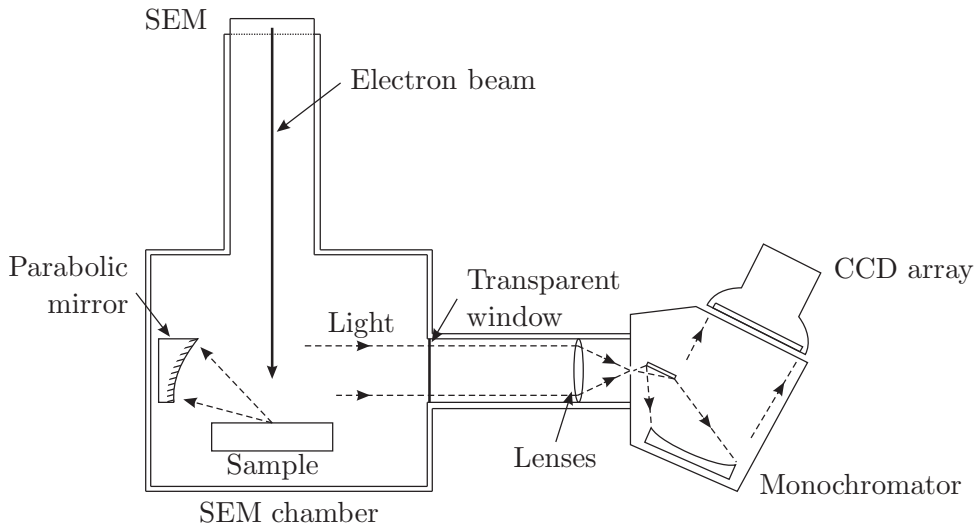

Figure 3.3: Schematic of the experimental setup for probing the optical properties of nanostructures with an electron beam. A beam of electrons, generated in the SEM column, is directed downwards to the sample. The light generated by the electrons on the sample is collected by the narrow-angle parabolic mirror and directed outside the microscope chamber through the transparent window. The system of lenses focuses the light onto slits of the monochromator connected to the CCD array, where the light is detected and its spectra acquired.

In a scanning electron microscope the beam of electrons is generated at the top of the microscope column within a cathode. Two types of cathode are supported in the scanning electron microscope used in the experimental setup: tungsten and LaB_6. The tungsten cathode is a twisted thin tungsten

wire heated by a current $\sim$ 2 A. Tungsten cathodes are inexpensive and easy to use, although they provide relatively poor electron intensity and the resulting beam diameter, determining the resolution, is significantly larger than for LaB_6 cathode. The latter consists of a pyramid-shaped microscopic crystal of lanthanum hexaboride (LaB_6) and electrodes supplying currents similar to ones used in the operation of a tungsten cathode. The operation of that type of cathode requires ultra high vacuum conditions with pressures several orders of magnitude lower than in the SEM chamber. Such low pressures are provided by a separate ion pump and are necessary in order to minimise the degradation of the crystal. The advantages of the LaB_6 cathode — high intensity and small diameter of the generated electron beam — make it the favorable candidate as a source of electrons for probing the optical properties of nanostructures.

Two modes of the SEM operation were used for the experiments: the *scanning mode* and the *spot mode*. The scanning mode is the basic mode of an electron microscope used to produce an image of the sample. In the scanning mode the position of the beam is moved in an automatic regime controlled by the SEM software. The beam continuously repositioned in an orderly fashion inside the rectangular area of a sample with the selected resolution and frequency. In this mode the imaging of the sample with the secondary electron detector along with the acquisition of the generated light spectrum is available. In the spot mode the electron beam is stationary and focused into a spot on the sample. The beam can be re-positioned manually allowing probing different areas of the sample. The imaging of the sample is not possible in the spot mode and the manual re-positioning can be done with the help of an image of the sample taken before entering the mode. The scanning electron microscope uses electron beams up to 10 nm in diameter allowing imaging and probing of structures with a nanoscale resolution.

The interaction of electrons with matter, as detailed in Section 3.3.1, is a very complex process. The energy of the primary electron beam can be transferred into the excitation of other electrons (secondary, backscattered, Auger etc.), photons (cathodoluminescence), x-rays, etc. For that reason, the probing of the optical properties of nanostructures requires an efficient

light collection system. As the light emitting region on the nanostructure excited by electron beam does not normally exceed 1×1 μm, the efficient collection of light can be realized with a *parabolic mirror*.

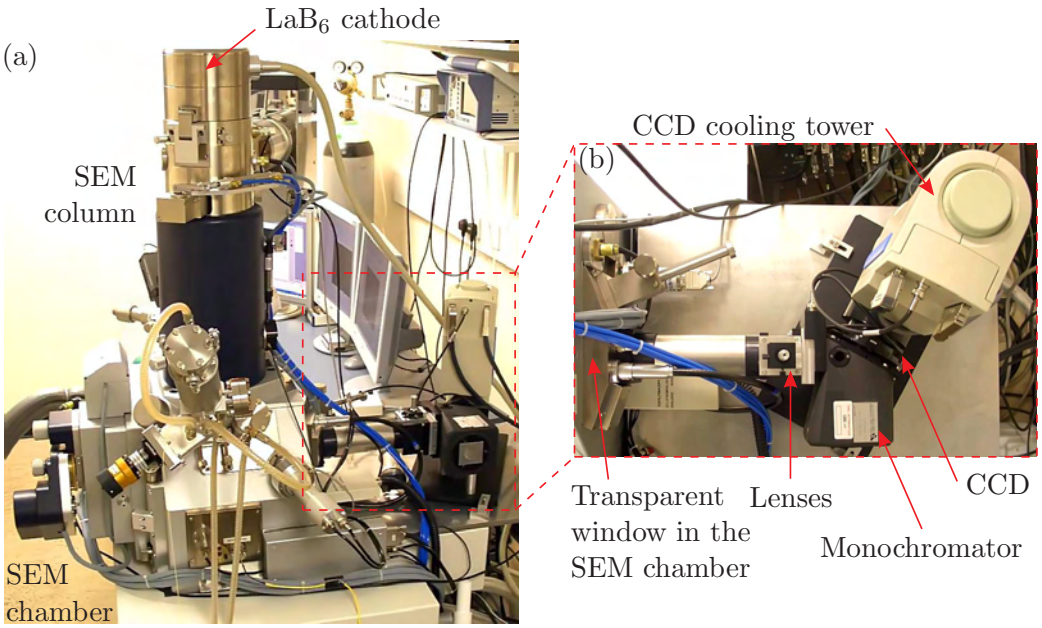

Figure 3.4: Experimental setup for probing the optical properties of nanostructures with an electron beam. Side view of the SEM with a modified light collection system (a): electron beam generated by LaB_6 cathode on top of the SEM column is directed downwards to the sample in the SEM chamber. (b) top view of the part of the light collection system outside the SEM chamber: system of lenses, monochromator and CCD array with liquid nitrogen cooling tower.

A mirror of parabolic shape operates very similarly to a convex lens. Should the point source be placed in a certain point in space, called the *focus* of the parabolic mirror, the mirror will redirect the radiation from the source into a parallel beam (Fig. 3.5a).

The alignment of the light emitting part of the sample and the focal point of the mirror is paramount for the performance of the whole light collection system. The position of the focus in the plane of the sample (x-y plane) was aligned with the centre of the electron microscope column by the manufacturer. Vertical axis alignment (z axis along the electron beam) can be performed by a motorized stage, on which the mirror is mounted (Fig. 3.5b).

The stage movements can be controlled from the outside of the SEM chamber and the optimal position of the mirror (full alignment of the focus and the emitting region of the sample) is achieved by maximizing the optical signal from the sample. The parabolic mirror in the described setup has 3×5 cm linear dimensions and a 5 cm focal distance.

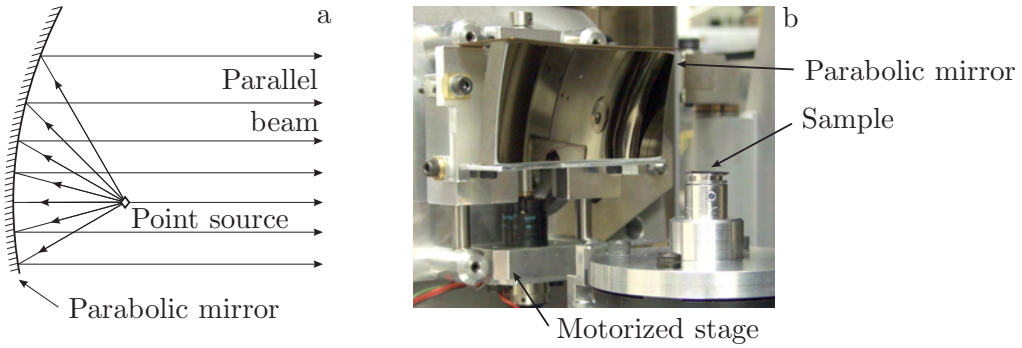

Figure 3.5: Operation of the parabolic mirror (a): light emitted by a point source located in the focus of the parabolic mirror is reflected as a parallel beam. A picture of the parabolic mirror used in the experimental setup to probe the optical properties of nanostructures with an electron beam (b).

The investigation of non-conducting samples in electron microscopes is not always possible (without major modifications of the surface of the sample, such as deposition of conducting films) due to inevitable charging of the sample which results in the distortion of the electromagnetic field in the vicinity of the sample and unpredictable variations in the results. However, the electron microscope used in this experimental setup allows for the probing of optical properties of non-conducting samples by discharging them with low-pressure gas supplied into the chamber. Although such study is far beyond the performed research, it is worth mentioning that the developed technique is not limited to the metallic nanostructures.

3.3.3 Calibration and quantum efficiency of the light collection system

The light collection system used in the experimental setup described above consists of several elements that will inevitably modify the spectrum of the

light before it reaches the CCD array of the spectrometer. Even then as the spectral efficiency of the array is non-uniform in the required range, the detected spectrum will be distorted. To avoid contributions of the components of the light collection system, it was calibrated.

The calibration of the light collection system was performed using an Ocean Optics LS-1 tungsten halogen broadband white light source. The spectrum analyzer, consisting of the spectrometer and the monochromator, was calibrated by comparing the LS-1 spectrum measured by direct illumination of the monochromator slits, with the spectral efficiency of the source provided by the manufacturer (corresponding spectra are presented in Figure 3.6a). The result was compared to a theoretical prediction of the spectrum efficiency of the spectrum analyzer obtained as a product of spectral efficiencies of the monochromator and the CCD array provided by the manufacturer. It was found that the experimental spectral efficiency of the monochromator and spectrometer, obtained in the experiment, and theoretical curve correlated remarkably well, giving similar dependency.

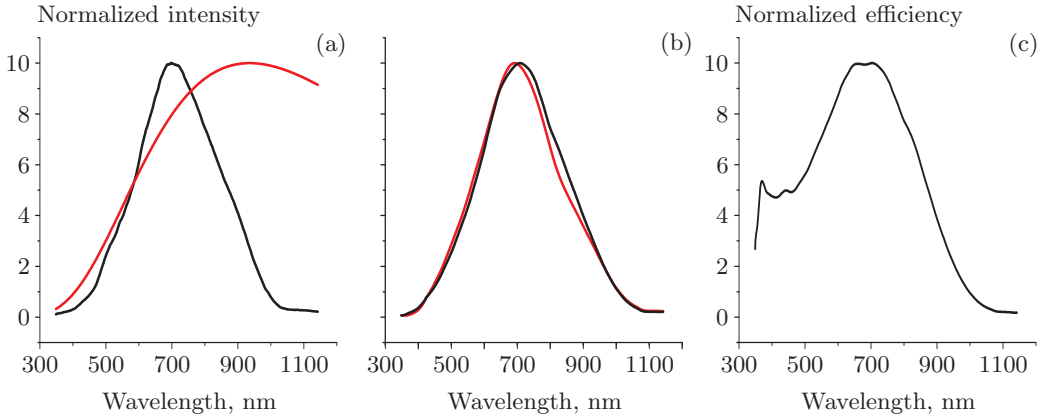

Figure 3.6: Calibration of the light collection system with broadband light source and optical fibre. Spectra of the source measured by direct illumination of the monochromator slits (black curve, a) and of the source provided by the manufacturer (red curve, a), giving the spectral efficiency of the monochromator and spectrometer. Spectra of the light collected from the end of the fibre by the light collection system (black curve, b) and of the fibre illuminating the slits of the monochromator directly (red curve, b), giving the spectral efficiency of the mirror, window and the lenses. Calibration curve of the light collection system (c).

Calibration of the part of the light collection system before the spectrum analyzer, consisting of the parabolical mirror, transparent window in the SEM chamber and a set of lenses, was performed by the LS-1 with a single mode optical fibre. The point light source, necessary for the performance of the parabolic mirror, was realized with the tip of the optical fibre, illuminated by LS-1. The spectral efficiency of the mirror, window and lenses was measured as a ratio between the spectrum of light collected from the end of the fibre by the system and the spectrum of the fibre illuminating the slits of the monochromator directly (corresponding spectra are presented in Figure 3.6b). The *spectrum calibration* curve for the whole light collection is a product of a spectral efficiency of the monochromator–spectrometer and the mirror–window–lenses parts (Fig. 3.6c). By dividing every measured spectrum by the obtained spectral efficiency of the light collection system it was possible to acquire undisturbed results.

The *quantum efficiency* of the light collection system was estimated both theoretically and experimentally. The quantum efficiency of the light collection system is the ratio between the energy of the photons leaving point-like source in the solid angle of 2π and the energy detected by the CCD array of the spectrum analyzer as the result of the collection and propagation of that light through the system. The theoretical approach takes into account geometrical properties of the mirror and narrow slits of the monochromator along with efficiencies of the spectrometer provided by the manufacturer. The experimental approach is based on the measurement of the power of the LS-1 broadband white light course with the attached single mode fibre through the light collection system of the experimental setup and by a calibrated power meter. Both estimates give the approximate value of 10^{-5} for the quantum efficiency of the system.

The *spectral resolution* of the system is defined by the size of the CCD array of the spectrum analyzer in the direction of the expansion of light by the monochromator grating. The spectrum analyzer allows measuring spectra in 350–1150 nm region and the measured spectra consist of 1024 points. Therefore, the spectral resolution is roughly 0.8 nm.

One of the main disadvantages of the light collection system described above, is the long focal distance of the parabolic mirror allowing only narrow-angle light collection. This decreases the quantum efficiency of the system. However, the narrow angle of light collection can be turned into an advantage when it comes to the interpretation of the results: the fact that the light decoupled by a diffraction grating is collected in a narrow range of angles allows for distinguishing between different orders of decoupling, which otherwise would be complicated by overlapping of orders (see Section 3.5). The quantum efficiency of this system was sufficient enough to perform the work described in this Chapter. For the next stage of the research, presented in Chapters 4 and 5, the parabolic mirror was replaced by a more efficient one with 1 mm focal distance. In those Chapters the parabolic mirror described in this Section is denoted as a "narrow-angle" parabolic mirror, as opposed to a "wide-angle" mirror with a short focal distance.

Despite the fact that the spectrum analyzer is capable of resolving spectra in 350–1150 nm wavelength range, the wavelength interval for the obtained spectra had to be reduced to 350–1000 nm. This was done due to an extremely poor singal/noise ratio in the resulting differential spectra for the wavelengths above 1 μm from the samples used in the study.

3.3.4 Spatial resolution of the system

The *spatial resolution* of the experimental setup, described above, is largely affected by the electron beam size, the size of the generation volume, which is related to the beam penetration range in the material, and the minority carrier diffusion. Additional factors such as a low signal-to-noise ratio, vibrations, and electromagnetic influence may degrade the resolution in practice.

A minimal signal-to-noise ratio is required for the probing of the optical properties with the electron beam. This depends on detector sensitivities and electronic system noise levels. This, in turn, determines the minimum signal intensity necessary to get pixel brightness above the noise level for

reliable data processing. A certain beam power will be necessary in order to excite that level of signal for any given specimen.

The size of the electron beam decreases with the decrease of the beam current and the increase of the beam voltage. For example, the electron beam diameter for a 30 keV beam generated by the LaB_6 cathode is approximately 4 nm for an electron probe current of 10^{-5} μA, increasing to about 25 nm for 10^{-3} μA and to about 300 nm for 1 μA [66]. Secondary electrons have the smallest generation volume, with a diameter little larger than the probe diameter. Thus, the secondary electron images of the sample can be used to determine the size of the electron beam [68], following the simple procedure described below.

The *size of the electron beam* can be estimated by imaging the "test sample": a metallic film with structures of a known range of sizes on it, with the minimal geometrical feature size less than that of the electron beam. The smallest resolved feature in the image would give an estimate of the beam size. In the absence of such sample, this can be done by analyzing the secondary electron image of a step-like structure (Fig. 3.7). The edge of one of the 50 nm high ribs of the 400 nm period diffraction grating manufactured on a gold surface can be used as a step-like structure. Consider the area A in the vicinity of the edge of the rib (Fig. 3.7a). By averaging the signal along the y-axis, one can obtain a distribution of the signal along axis x_A. Assuming that the edge of the grating is ideal and is indeed a sharp step, the obtained curve would represent the integral of the step by an electron beam of a finite size. The size of the electron beam d_{beam} can be determined as the distance between the minimum (the bottom part of the step) and maximum (the top part of the step) values of the curve (Fig. 3.7b). For the electron beam used for imaging (electron beam energy 40 keV, current 0.01 μA) the obtained estimate of the electron beam size is $d_{\text{beam}} = 150$ nm.

In practice, at low electron currents, the spatial resolution of the cathodoluminescence is determined by the size of the excitation volume necessary to satisfy the signal-to-noise ratio requirement. Increasing the electron beam energy improves the signal-to-noise ratio, but it also produces a larger excitation volume. For larger values of the electron probe current (approximately

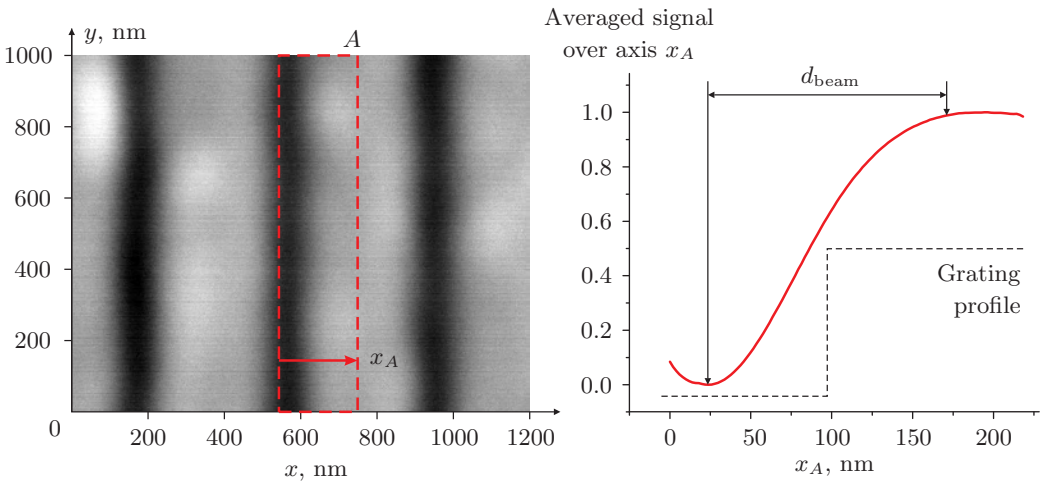

Figure 3.7: Determination of the size of the electron beam from a secondary electron image of the step. Secondary electron image of the 400 nm period grating with area A in the vicinity of the edge of the rib, representing the step (a). White areas correspond to ribs of the grating, and black areas are spaces between ribs. Average signal distribution in the area A along axis x_A (b) is the step-like profile of the grating integrated by the electron beam of size d_{beam}, which can be determined as the distance between points of minimum and maximum signal in the averaged signal curve: $d_{\text{beam}} = 150$ nm (electron beam energy 40 keV, current 0.01 μA).

0.1 μA and greater), the incident beam diameter becomes larger, comparable to that of the generation volume. In most inorganic solids, a CL spatial resolution of the order of 1 μm or less can be achieved.

The *electron beam current* can be determined using a Faraday cup built into the microscope. A Faraday cup is a retractable conducting metal chamber in the SEM column which intercepts the electron beam before it hits the sample. The electric charge, induced by the electrons on the metal surface of the chamber is measured giving the current of the electron beam. The equipped Faraday cup allows for measuring beams with currents as low as 1 pA (10^{-12} A).

The experimental setup presented in this Section, allows for probing the optical properties of nanostructures with the resolution of the scanning electron microscope. The system was used to demonstrate that a beam of free electrons creates a highly localized source of propagating surface plasmon polaritons on both a diffraction grating (Section 3.5) and an unstructured

metal film (Section 3.6). The theoretical description of the surface plasmon polaritons (SPPs) and the decoupling of SPPs by a diffraction grating, vital for the interpretation of the experimental results, is presented in the following Section.

3.4 Theory of surface plasmon polaritons

Theoretical description of surface plasmon polaritons and localized surface plasmons on a metal–dielectric interface is provided in this Section following [75, 76]. It is shown that only p-polarized surface plasmon polaritons can exist on a metal–dielectric interface, and the conditions of the SPP are found. The impossibility of direct light decoupling into SPP is demonstrated and the decoupling of the SPPs into light by a diffraction grating is discussed. Parameters of surface plasmon polariton propagation along a metal–dielectric interface, decay length and depth of propagation into metal, are derived.

3.4.1 The surface plasmon polariton condition

Consider a system consisting of a dielectric material characterized by an isotropic, real and positive dielectric constant ε_1, occupying half space $x > 0$. The half space $x < 0$ consists of a metal, characterized by an isotropic, frequency-dependent and complex dielectric function $\varepsilon_2(\omega) = \varepsilon_2'(\omega) + i\varepsilon_2''(\omega)$, as shown in Figure 3.8. Both media are considered to be non-magnetic.

The electromagnetic field of a surface plasmon polariton at the interface of such dielectric-metal system can be obtained from the solution of Maxwell's equations in each medium:

$$\nabla \times \mathbf{H}_i = \varepsilon_i \frac{1}{c}\frac{\partial}{\partial t}\mathbf{E}_i \tag{3.1}$$

$$\nabla \times \mathbf{E}_i = -\frac{1}{c}\frac{\partial}{\partial t}\mathbf{H}_i \tag{3.2}$$

$$\nabla \cdot (\varepsilon_i \mathbf{E}_i) = 0 \tag{3.3}$$

$$\nabla \cdot (\mathbf{H}_i) = 0, \tag{3.4}$$

and the associated boundary conditions:

$$\mathbf{n} \times (\mathbf{E}_2 - \mathbf{E}_1) = 0, \qquad \mathbf{n} \times (\mathbf{H}_2 - \mathbf{H}_1) = 0 \tag{3.5}$$

along with the normalization to the infinity condition:

$$\mathbf{E}_1|_\infty = \mathbf{E}_2|_\infty = 0, \qquad \mathbf{H}_1|_\infty = \mathbf{H}_2|_\infty = 0. \tag{3.6}$$

Here index i describes the media: $i = 1$ for the dielectric and $i = 2$ for the metal. Pairs of $(\mathbf{E}_i, \mathbf{H}_i)$ denote electric and magnetic fields in the corresponding media. The boundary conditions express the continuity of the tangential components of the electric and magnetic fields across the interface, and the vanishing of these fields infinitely far from the interface is guaranteed by the equation (3.6).

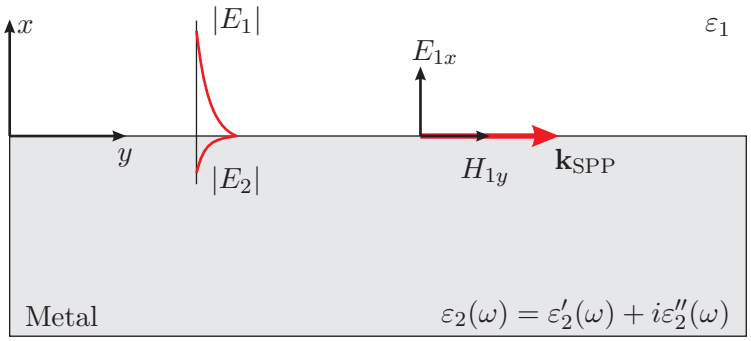

Figure 3.8: Surface plasmon polariton wave $\mathbf{k}_{\mathrm{SPP}}$ exists only in TM configuration of electromagnetic field (electric field $\mathbf{E}$ perpendicular and magnetic field $\mathbf{H}$ parallel to the surface), often referred to as p-polarization, on the metal–dielectric interface. The amplitude of the SPP wave $|E_i|$ decays exponentially on each side of the interface.

First consider a p-polarized (transverse magnetic or TM) wave in this structure that propagates along the metal–dielectric interface in the y direction. For a wave of this polarization the magnetic vector is perpendicular to the plane of incidence — the plane defined by the direction of propagation and the normal to the surface. The solutions of Maxwell's equations that are wavelike in the x-direction and whose amplitudes decay exponentially with increasing distance into each medium from the interface $y = 0$ can be

written as:

$$\mathbf{E}_i = (E_{ix}, 0, E_{iz})\, e^{-k_i|x|} e^{-iq_i y - i\omega t}, \tag{3.7}$$

$$\mathbf{H}_i = (0, E_{iy}, 0)\, e^{-k_i|x|} e^{-iq_i y - i\omega t}. \tag{3.8}$$

Here q_i is the magnitude of a wave vector that is parallel to the surface. Magnitude of vectors k_1 and k_2 determine the decay of the electromagnetic field with increasing distance from the surface. Introducing equations (3.7) and (3.8) into Maxwell's equations for each media (3.1)–(3.4), one can obtain:

$$ik_1 H_{1y} = +\frac{\omega}{c}\varepsilon_1 E_{1x}, \qquad ik_2 H_{2y} = -\frac{\omega}{c}\varepsilon_2 E_{2x} \tag{3.9}$$

and:

$$k_i = \sqrt{q_i^2 - \varepsilon_i \frac{\omega^2}{c^2}} \tag{3.10}$$

Using boundary conditions (3.5) and Equations (3.9), the following system of equations can be derived:

$$\begin{aligned} \frac{k_1}{\varepsilon_1} H_{1y} + \frac{k_2}{\varepsilon_2} H_{2y} &= 0, \\ H_{1y} - H_{2y} &= 0, \end{aligned}$$

which has a solution only if the determinant is zero, i. e.

$$\frac{k_2}{k_1} = -\frac{\varepsilon_2}{\varepsilon_1}. \tag{3.11}$$

This equation is the *surface plasmon condition*.

If, for the moment, we assume that the dielectric function of the metal $\varepsilon_2(\omega)$ is real ($\varepsilon_2(\omega) = \varepsilon_2'(\omega)$), then wave vectors k_1 and k_2 must be real and positive in order for equations (3.7) and (3.8) to describe a surface electromagnetic wave. It follows, therefore from equation (3.11) that $\varepsilon_2'(\omega)$ must be *negative* for this surface plasmon wave to exist. For these frequencies ω the wave vector of a volume electromagnetic wave is purely imaginary. Thus such surface electromagnetic waves exist only in the frequency range where volume electromagnetic waves cannot propagate in a metal.

From the boundary conditions (3.5) it also follows that the surface wave vector $\mathbf{q}$ should be continuous, i. e. $q_1 = q_2 = q$. Hence, the explicit expression for the wave number of the surface plasmon polariton $k_{\mathrm{SPP}} = q$ as a function of ω can be obtained from equations (3.10) and (3.11):

$$k_{\mathrm{SPP}}(\omega) = \frac{\omega}{c}\sqrt{\frac{\varepsilon_1\varepsilon_2(\omega)}{\varepsilon_1 + \varepsilon_2(\omega)}}, \tag{3.12}$$

where ω/c represents the magnitude of the light wave vector. The obtained relation (3.12) is valid even when $\varepsilon_2(\omega)$ is complex. Although dielectric functions $\varepsilon_2(\omega)$ are available for many metals, it is easier to illustrate the preceding result using the free electron model of the dielectric function:

$$\varepsilon_2(\omega) = 1 - \frac{\omega_{\mathrm{p}}^2}{\omega^2}.$$

Here ω_{p} is the frequency of bulk longitudinal electron excitations, the plasma frequency. The corresponding dispersion curve of the surface plasmon polariton $k_{\mathrm{SPP}}(\omega)$, calculated for a gold–dielectric interface in the wavelength range $\lambda = 0.3$–6 μm assuming $\omega_{\mathrm{p}} = 1.38 \times 10^{16}$ s^{-1} and ($\varepsilon_1 = 2.6$), is shown in Figure 3.9.

It can be seen that the propagating surface plasmon wave *can not radiate* into the dielectric medium as the wave vector k_{SPP} exceeds the wave vector $\omega\sqrt{\varepsilon_1}/c$ of light at all frequencies as the curve $k_{\mathrm{SPP}}(\omega)$ always lies below $\omega = ck_{\mathrm{SPP}}/\sqrt{\varepsilon_1}$. The reverse statement is also true: surface plasmon polaritons *can not be excited* on a metal surface with conventional illumination from the adjacent dielectric due to the mismatch between the wave vectors of incident radiation and SPPs.

The dispersion curve for surface plasmon polaritons (Fig. 3.9) also shows that at high values of $ck_{\mathrm{SPP}}/\omega_{\mathrm{p}}$ the dispersion curve has an asymptote $\omega = \omega_{\mathrm{p}}/\sqrt{(1+\varepsilon_1)}$. It corresponds to an important subclass of surface plasmon polaritons — *surface plasmons*. These can be viewed as the limiting case of surface plasmon polaritons when the speed of light is allowed to become infinitely large. Alternatively, and equivalently, they are obtained from solutions of Laplace's equation for a scalar potential that propagate in a wavelike fashion along a planar dielectric–metal interface, and whose

amplitudes decay exponentially with increasing distance from the interface into each medium. Surface plasmons are therefore *electrostatic surface waves*. One can think of them as related to non-propagating collective vibrations of the electron plasma near the metal surface.

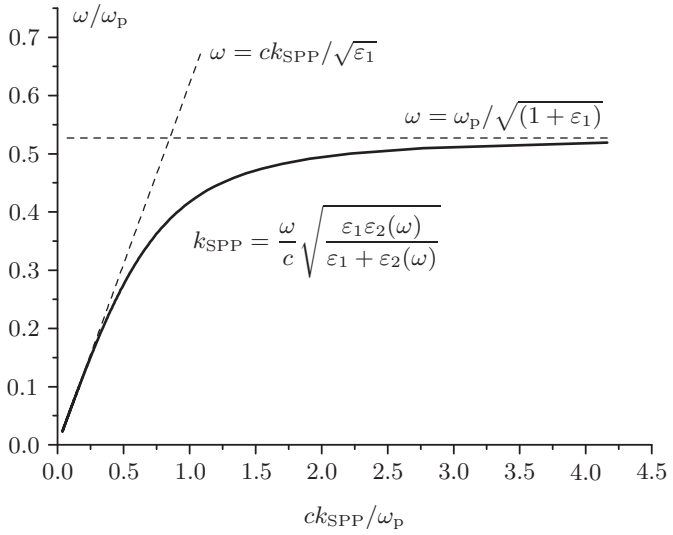

Figure 3.9: Dispersion curve $k_{SPP}(\omega)$ of a surface plasmon polariton propagating on a gold–dielectric ($\varepsilon_1 = 2.6$) interface in the range of wavelength $\lambda = 0.3$–6 μm. The free electron model of the dielectric constant $\varepsilon_2(\omega)$ was used for gold ($\omega_p = 1.38 \times 10^{16}$ s^{-1}). Also plotted is the dispersion of light ($\omega = \omega_p/\sqrt{(1+\varepsilon_1)}$) in the dielectric medium, and the corresponding surface plasmon frequency.

Due to ohmic losses in the metal, characterized by the imaginary part of the dielectric function of the metal ($\varepsilon_2'' > 0$), the energy carried by a surface plasmon polariton decays exponentially as the SPP propagates along the planar dielectric-metal interface. The $1/e$ decay length, called the the energy propagation length L_{SPP}, is determined by the imaginary part of the magnitude of the SPP wave vector:

$$L_{SPP} = \frac{1}{2\,\mathrm{Im}k_{SPP}}. \tag{3.13}$$

The decay length of surface plasmon polaritons strongly depends on its wavelength and dielectric function of the metal and ranges from nanometers to tens of microns.

Equations (3.7), (3.8) and (3.10) allow defining another important characteristic of the surface plasmon polaritons — the depth of propagation into the conductor, also known as skin depth:

$$\delta = \frac{1}{2\mathrm{Re}k_2} = \left(2\mathrm{Re}\left\{ \sqrt{k_{\mathrm{SPP}}^2 - \varepsilon_2 \left(\frac{\omega}{c}\right)^2} \right\} \right)^{-1}. \tag{3.14}$$

The intensity of the SPP wave decays exponentially on both sides of the metal–dielectric interface, therefore one can consider surface plasmon polaritons localized along the axis, perpendicular to the interface, in the skin depth region δ of the metal. Typical values of δ for most metals used in optics (such as gold, aluminium or silver) do not exceed a hundred nanometers in the visible range of the spectrum.

Now consider an *s*-polarized (transverse electric or TE) wave in the structure depicted in Figure 3.8. In a wave of this polarization it is the electric vector that is perpendicular to the plane of incidence. Following the procedure described for the TM mode, one can obtain the surface plasmon condition for that polarization:

$$k_1 + k_2 = 0. \tag{3.15}$$

Real parts of k_1 and k_2 are required to be positive in order for the electromagnetic wave to be localized at the metal–dielectric interface. Therefore, condition (3.15) can not be fulfilled and *s*-polarized surface plasmon polariton cannot exist in the structure depicted in Figure 3.8.

3.4.2 Decoupling of surface plasmon polaritons by a diffraction grating

Consider a surface plasmon polariton with a wave vector $\mathbf{k}_{\mathrm{SPP}}$ propagating along a metal–dielectric interface. At any given frequency the magnitude of $\mathbf{k}_{\mathrm{SPP}}$ will be greater than of $\mathbf{k}_{\mathrm{light}}$ — the wave vector of light propagating in the dielectric part of the system (Fig. 3.9). This mismatch between wave vectors of SPP and light makes direct decoupling of surface plasmon polaritons into light impossible. However, the mismatch ($\mathbf{k}_{\mathrm{SPP}} - \mathbf{k}_{\mathrm{light}}$) can be

compensated by a modification of the metal–dielectric surface, a diffraction grating, and by that grating the SPPs can be decoupled into light in a controlled way.

A grating fabricated on a metal surface facilitates decoupling of light by providing a wave vector mismatch equal to an integer multiple of the grating vector $|\mathbf{k}_{\mathrm{G}}| = 2\pi/a$ where a is the grating period:

$$\mathbf{k}_{\mathrm{SPP}} - n\mathbf{k}_{\mathrm{G}} = \mathbf{k}_{\mathrm{light}} \sin\theta, \tag{3.16}$$

where θ is the angle of the surface plasmon polariton decoupling with wave vector $\mathbf{k}_{\mathrm{SPP}}$ into light $\mathbf{k}_{\mathrm{light}}$. The process of decoupling in the *forward* direction, for positive angles of decoupling $\theta > 0$, is illustrated in Figure 3.10a. The *backward* decoupling will correspond to negative values of θ or, equally, to the SPPs characterized by $-\mathbf{k}_{\mathrm{SPP}}$ wave vector (and negative orders of decoupling n). As before, the surface plasmon polariton propagating on the interface between a dielectric and metal is characterized by dielectric functions ε_1 and $\varepsilon_2(\omega)$ respectively (see Section 3.4.1).

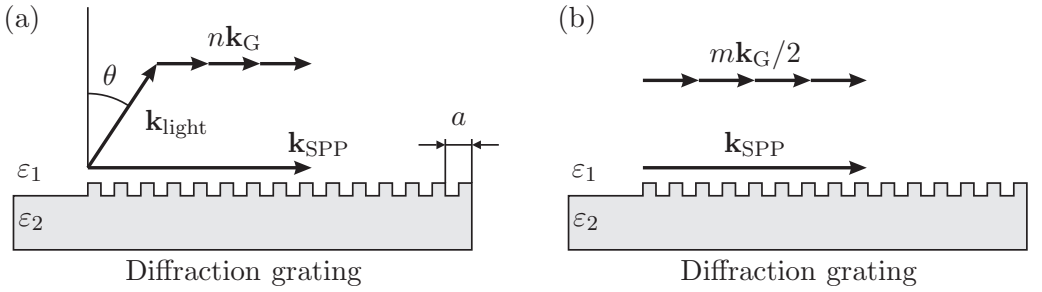

Figure 3.10: Decoupling of SPP with a diffraction grating in a forward direction, for the negative angles of decoupling $\theta < 0$ (a): the grating compensates the mismatch between SPP and light wave vectors by a wave vector equal to an integer multiple of the grating vector $|\mathbf{k}_{\mathrm{G}}| = 2\pi/a$ (a is the grating period). Excitation of Bragg resonances on a diffraction grating by surface plasmon polaritons (b): the grating modifies plasmon dispersion at frequencies $\omega = \omega_{\mathrm{res}}$ given by the Bragg condition $\mathbf{k}_{\mathrm{SPP}} = m\mathbf{k}_{\mathrm{G}}/2$. At those frequencies the decoupling of SPPs into light should be inhibited by the grating.

The angle of decoupling as a function of frequency can be derived from equations (3.12) and (3.16):

$$\theta(\omega) = \frac{c}{\omega} \arcsin\left(\mathrm{Re}\left\{ \frac{\omega}{c} \sqrt{\frac{\varepsilon_1 \varepsilon_2(\omega)}{\varepsilon_1 + \varepsilon_2(\omega)}} \right\} - n\frac{2\pi}{a} \right), \tag{3.17}$$

where ε_1, $\varepsilon_2(\omega)$ are dielectric functions of the dielectric and metal respectively, a is the period of the grating and n is an integer number denoting the order of diffraction (decoupling). The $\theta(\omega)$ allows calculating directions of the decoupling of SPPs by the grating and therefore allowing controlled decoupling of SPPs of certain frequency in the selected direction varying the period of the grating a. Unfortunately, a simple analysis of the efficiency of the decoupling, depending on the height and ratio between high and low elements of the grating, can not be performed in a way similar to equation (3.17), and numerical methods should be applied to this problem.

The decoupling of propagating SPPs with a grating is also affected by Bragg diffraction, intrinsic to the interaction of periodic structures with waves of any kind. The grating modifies plasmon dispersion at frequencies $\omega = \omega_{\mathrm{res}}$ given by the Bragg condition $\mathbf{k}_{\mathrm{SPP}} = m\mathbf{k}_{\mathrm{G}}/2$, which can be written as:

$$mk_{\mathrm{G}}/2 = \mathrm{Re}\{k_{\mathrm{SPP}}(\omega_{\mathrm{res}})\} = \frac{\omega_{\mathrm{res}}}{c} \mathrm{Re}\left[\left(\frac{\varepsilon_1 \varepsilon_2(\omega_{\mathrm{res}})}{\varepsilon_1 + \varepsilon_2(\omega_{\mathrm{res}})} \right)^{1/2} \right]. \tag{3.18}$$

At frequencies $\omega = \omega_{\mathrm{res}}$ the decoupling of SPPs into light is expected to be inhibited by the grating. Excitation of Bragg resonances by surface plasmon polaritons on a diffraction grating is illustrated in Figure 3.10b.

It has, therefore, been shown that only p-polarized surface plasmon polaritons can exist on a metal–dielectric interface, and the conditions of the SPP were found. Two major mechanisms controlling the decoupling of surface plasmon polaritons by a diffraction grating have been identified and described. The formulae allowing the prediction of peaks and troughs in the decoupled spectra were derived.

3.5 Light emission from a metal grating stimulated with an electron beam

Interpretation of the cathodoluminescence spectra, as detailed in Section 3.3.1, is extremely difficult due to the lack of any generally applicable theory for the wide variety of possible types of luminescence centers and radiative recombination mechanisms. The influence of defects, the surface, and many other factors have to be considered in the analysis of the cathodoluminescence spectra. However, modifying the geometry of the surface of a conductor in a certain way, allows extracting one of the energy channels of cathodoluminescence that is of particular interest to this research: *surface plasmon polaritons* (SPPs).

These SPPs can be decoupled into light by a microscopic grating manufactured on the metal film (Fig. 3.11), as described in the previous Section. The decoupled light is then collected and analyzed by the light collection

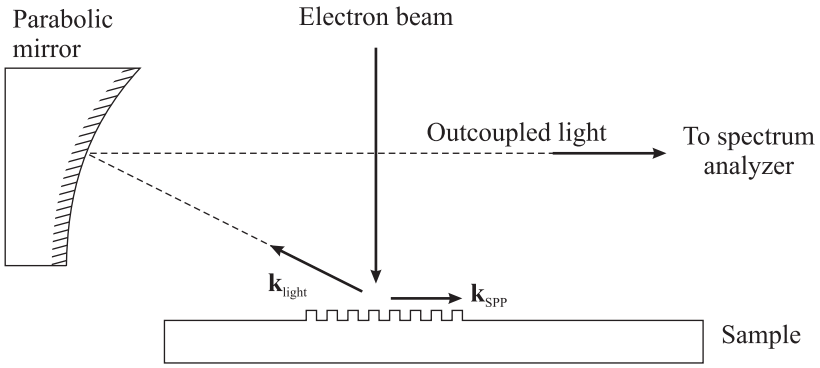

Figure 3.11: Excitation of surface plasmon polaritons on a microscopic grating manufactured on the metal film. An injection of a beam of free electrons on the grating results in the excitation of SPPs with wave vector $\mathbf{k}_{\mathrm{SPP}}$ and their decoupling as light $\mathbf{k}_{\mathrm{light}}$ by a grating.

system of the experimental setup (see Section 3.3). The evidence of the excitation of the surface plasmon polaritons can be seen by comparing the spectrum of the electron beam-induced light emission from an unstructured metal surface, to that of the grating.

The samples used were 250 nm thick gold films on a silicon substrate which incorporated gratings with a period of 4.25 μm and 300 nm[1]. The silicon substrates were first spin-coated with two polymer resins for lift-off processing, then patterned using electron beam lithography and developed, leaving the exposed areas clean down to the silicon substrate. This was followed by molecular beam epitaxial deposition of a buffer layer of 10 nm chromium and a 50 nm gold film, which after lift-off provided gold ribs matching the design of the grating structure on the bare silicon. Finally a 200 nm layer of gold was sputtered onto the substrate, to provide a continuous gold film, with the grating formed at the positions of the underlying array of gold ribs. The rib height of the final gold grating was found to be 50 nm. The gratings consisted of 30 periods for 4.25 μm and 300 periods for 300 nm grating of 1 mm long ribs. The gratings were designed to maximize decoupling of light in the backward direction (see Section 3.4.2), as shown in Figure 3.11. The optimization of the design of the gratings was performed by finite element simulations by Dr. A.V. Krasavin [77–79].

The experiments were first performed on a 4.25 μm period grating using the scanning mode of the microscope (see Section 3.3.2), with 50 kV electron beam of current 10 μA and a scan area of about 130 $\times$ 100 μm. Optical emission of the unstructured gold surface was clearly seen in the experiments. This is a combination of the *d*-band luminescence, as previously seen in femtosecond photoluminescent experiments [80], transient radiation of the collapsing dipoles formed by the electrons approaching the metal surface and their oppositely charged mirror image, and the fluorescence of any residual contaminants on the sample. These mechanisms of emission create a smooth spectrum centered at about 700 nm ($\sim$ 1.8 eV), shown as curve B in the inset of Figure 3.12.

The emission spectrum of an unstructured gold surface was identical to that of the grating with its ribs parallel to the direction towards the collection mirror. However, when the grating was oriented with its ribs perpendicular to the direction to the mirror, the emission was stronger than that of the

[1]The gratings were kindly manufactured by Dr. Yifang Chen, Rutherford Appleton Laboratory Didcot, Oxon, OX11 0QX, United Kingdom

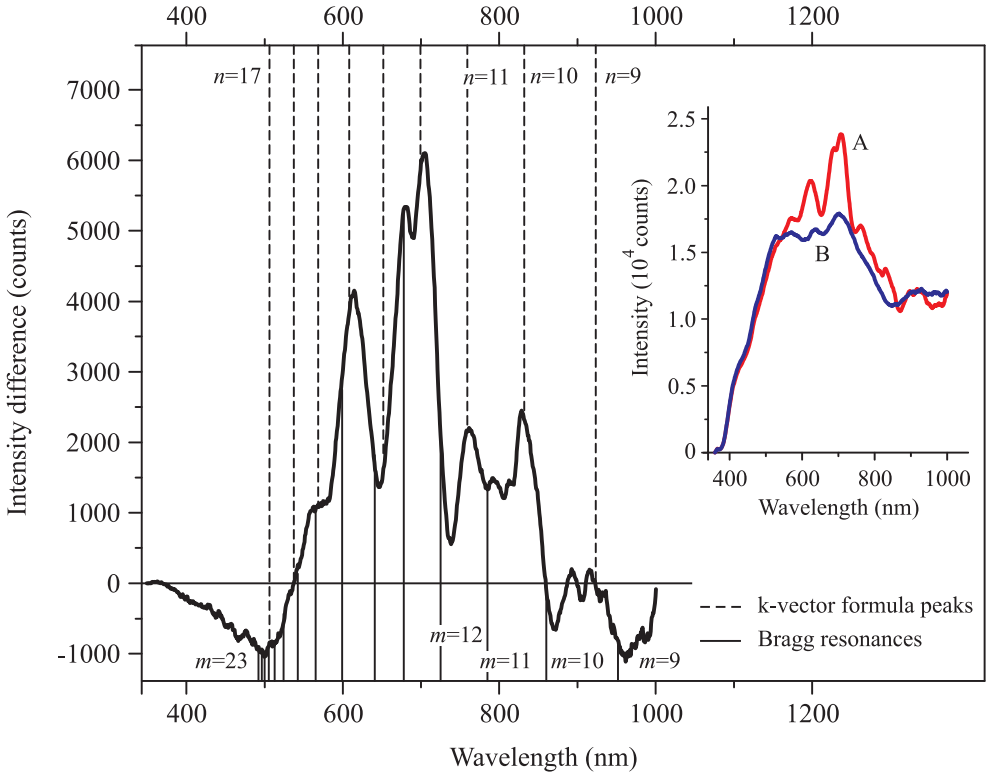

Figure 3.12: Differential spectrum of light emission of a gold grating of period $a = 4.25$ μm, oriented with its ribs perpendicular to the direction of the mirror and excited by a beam of electrons of 50 keV energy at a beam current of 10 μA. The inset shows non-normalized emission spectrum of (A) the grating and (B) the unstructured gold surface. The differential spectrum is obtained by subtracting spectrum B from spectrum A, hence implying that the differential spectrum only consists of the impact of the grating, eliminating transient radiation and luminescence of the gold film. Theoretical predictions of wavelengths at which optimum detection of the decoupled radiation occur are indicated with the corresponding diffraction orders n; Bragg resonances, at which the decoupling is expected to be inhibited by the gratings, are indicated with corresponding resonance orders m.

unstructured gold and its spectrum showed some pronounced modulations (curve A in the inset of Figure 3.12). The difference (solid black curve in Figure 3.12) in detection of emission is explained by the directionality of the decoupling of the traveling SPPs, which only in the latter case are decoupled into light directed towards the detection system.

The detected spectra of decoupled surface plasmon polaritons can be interpreted using theoretical approach described in Section 3.4.2. Equation (3.16) allows obtaining spectral distribution of decoupling angles for surface plasmon polaritons on a grating with period a. It can be written as:

$$\mathrm{Re}\{k_{\mathrm{SPP}}(\omega)\} - nk_{\mathrm{G}} = \frac{\omega}{c}\sin\theta(\omega). \tag{3.19}$$

Here k_{SPP}, $k_{\mathrm{G}} = 2\pi/a$ and ω/c are wave vectors of the surface plasmon polariton, the grating and electromagnetic radiation decoupled at angle θ, respectively. Equation (3.19) is a momentum conservation law applied to the decoupling of surface plasmon polaritons by a grating, illustrated in Figure 3.13a. The orientation of wave vectors in Figure 3.13a was changed, as compared to Figure 3.10, to reflect the geometry of the experimental setup and the process of decoupling, which predominately occurs in the backward direction (see Section 3.4.2).

Equation (3.19) allows determining the angle of decoupling θ for wavelength $\lambda = 2\pi c/\omega$ and diffraction order n. However, as can be seen from Figure 3.13a, the decoupled electromagnetic radiation can not be detected at all angles: the parabolic mirror allows detection in the $-82° < \theta < -57°$ range with optimum angle of detection $\theta_{\mathrm{max}} = 70°$. By plotting $\theta(\lambda)$ dependence together with acceptance window of the mirror one can predict the position of the peak in the decoupled spectra: the intersection between $\theta_n(\lambda)$ and θ_{max} gives the wavelength λ_n at which a maximal plasmon emission is expected for the nth order of diffraction, as illustrated for the $a = 4.25$ μm grating in Figure 3.13b.

White areas in the $\theta(\lambda)$ axis represent the acceptance windows for both backward ($\mathbf{k}_{\mathrm{SPP}}$) and forward ($-\mathbf{k}_{\mathrm{SPP}}$) decoupling (see Section 3.4.2). The red horizontal line in the middle of each acceptance area is the optimal angle of detection $\theta_{\mathrm{max}} = -70°$. Grey areas correspond to angles of decoupling not accessible by the parabolic mirror, and therefore, the decoupled radiation is not detected for these $\theta(\lambda)$. Colored curves in Figure 3.13b are spectral dependencies $\theta(\lambda)$ for angles of decoupling n = 1–22 of the diffraction grating $a = 4.25$ μm, according to equation (3.19).

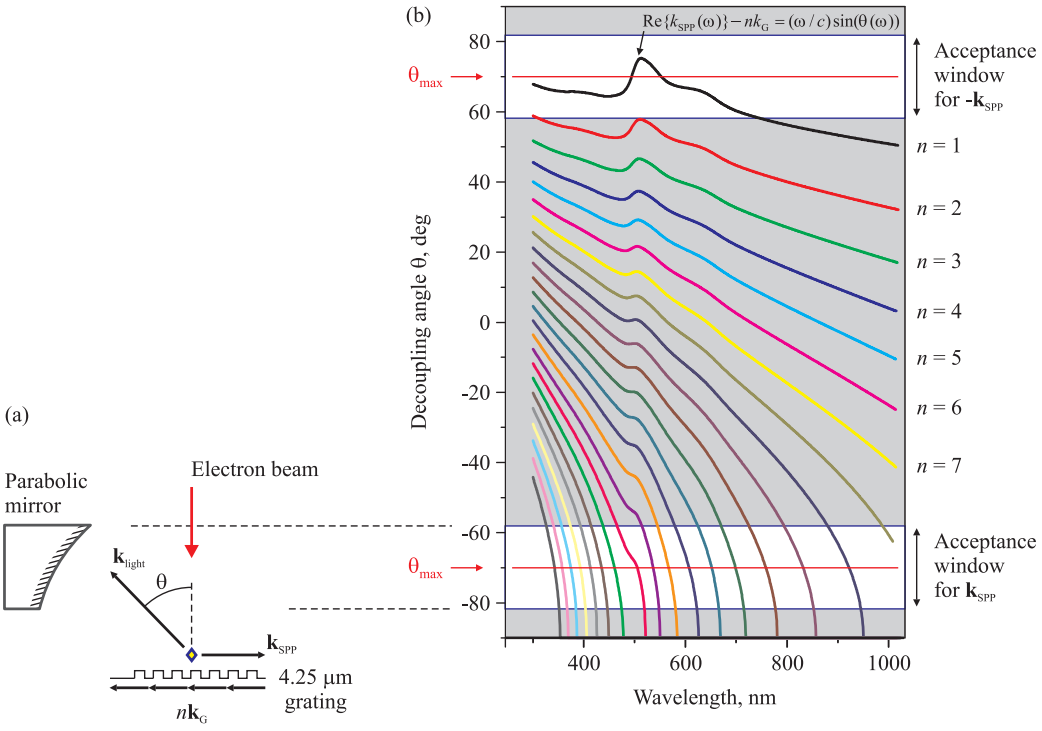

Figure 3.13: Prediction of the peaks in a detected spectrum of surface plasmons generated with the electron beam and decoupled by a 4.25 μm period gold grating. The grating facilitates decoupling of light by providing a wave vector mismatch equal to an integer multiple of the grating vector $\mathbf{k}_G$ so that $\mathbf{k}_{SPP} - \mathbf{k}_G = \mathbf{k}_{light} \sin\theta$ (a). The parabolic mirror, collecting light decoupled by the grating, has an acceptance angle in the range of $-82° < \theta < -57°$, limiting the frequencies at which decoupled SPPs can be detected (a). The wavelengths at which the interception of the $\theta_n(\lambda)$ curve with the red horizontal line in the acceptance window, which denotes the optimum angle of decoupling $\theta_{max} = 70°$, occurs, should correspond to the wavelengths of local maxima in the detected plasmon spectra (b).

It can be seen that orders $n = 1$–8 do not contribute to the detected spectra of backward decoupled SPPs, and only the first order of the forward decoupled SPPs contributes to the detected spectrum. Most of the intersections between $\theta_n(\lambda)$ and $\theta_{\max}$ in the backward decoupling acceptance window occur for diffraction orders $n = 9$ onwards. Each of those intersections gives a position of the peak which is likely to be observed in the experimental spectrum of surface plasmon polaritons decoupled by the grating.

In the spectrum shown in Figure 3.12, the peak wavelengths at which optimum detection of the decoupled radiation occur are indicated with the corresponding diffraction orders n. One can clearly see that, as expected, peaks in the emission spectrum to a high degree coincide with the predicted values for efficient SPP emission. One also can also observe several dips in the emission spectrum and even wavelengths at which the emission from the grating is less intense than that of unstructured gold. This is believed to result from the modification of the plasmon dispersion by the grating at frequencies $\omega = \omega_{\text{res}}$ given by the Bragg condition (see Section 3.4.2):

$$mk_{\text{G}}/2 = \text{Re}\{k_{\text{SPP}}(\omega)\} = \frac{\omega}{c}\text{Re}\left[\left(\frac{\varepsilon(\omega)}{1+\varepsilon(\omega)}\right)^{1/2}\right], \tag{3.20}$$

where m is a positive integer describing the resonance order. Here $\varepsilon(\omega)$ is the complex-valued permittivity of gold. Corresponding wavelengths of Bragg resonance are in Figure 3.12 presented for various values of m, indicating that the SPPs at Bragg resonance are either badly coupled to light or their generation by the electron beam is inhibited by the grating.

The excitation of surface plasmon polaritons by an electron beam has also been performed on a 300 nm period grating using the electrons of the same energy and current as for the 4.25 μm grating. A much shorter period of the grating results in the dramatic reduction of the number of diffraction orders in the spectra of the decoupled surface plasmons in the selected spectral range, as illustrated in Figure 3.14. The described theoretical method for finding peaks in the detected spectra predicts a single peak at 601 nm for the grating, as confirmed by the experiment (Fig. 3.15). Here again, the spectrum of decoupled plasmons (black curve) was obtained as the difference between

the light emission from the grating (curve A on the inset) and unstructured gold film (curve B on the inset). The peak wavelength at which optimum detection of the decoupled radiation occur is indicated with the corresponding diffraction order $n = 1$ and corresponding wavelengths of Bragg resonance presented for various values of m.

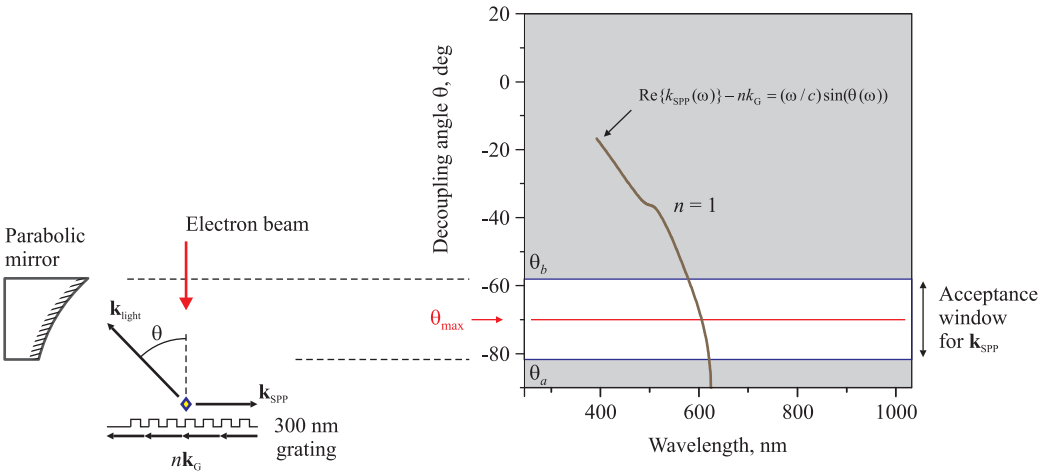

Figure 3.14: Prediction of the peaks in a detected spectrum of surface plasmons generated with an electron beam and decoupled by a 300 nm period grating. The grating facilitates decoupling of light by providing a wave vector mismatch equal to an integer multiple of the grating vector $\mathbf{k}_G$ so that $\mathbf{k}_{SPP} - \mathbf{k}_G = \mathbf{k}_{light} \sin\theta$ (a). The parabolic mirror, collecting light decoupled by the grating, has an acceptance angle in the range of $-82° < \theta < -57°$, limiting the frequencies at which decoupled SPPs can be detected (a). The wavelengths at which the interception of the $\theta_n(\lambda)$ curve with the red horizontal line in the acceptance window, which denotes the optimum angle of decoupling $\theta_{max} = 70°$, occurs, should correspond to the wavelengths of local maxima in the detected plasmon spectra (b).

It has therefore been indirectly demonstrated that the electron beam indeed creates propagating surface plasmon polaritons on a structured metal film. The experimental results are supported by theory predictions considering the decoupling of SPPs by a grating into a certain direction. The direct excitation of propagating surface plasmon polaritons with electron beam is detailed in the following Section.

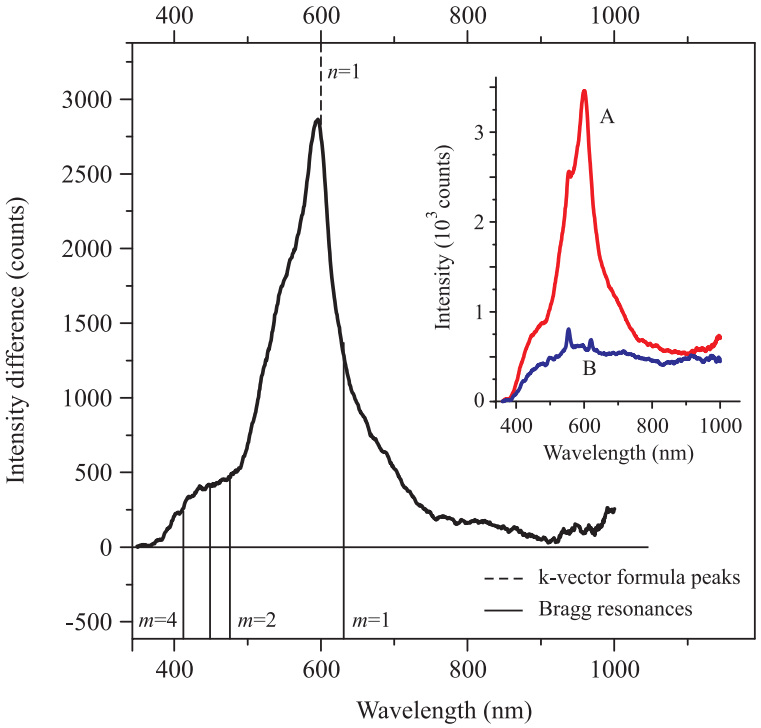

Figure 3.15: Differential spectrum of light emission of a gold grating of period $a = 300$ nm, oriented with its ribs perpendicular to the direction of the mirror and excited by a beam of electrons of 50 keV energy at a beam current of 10 μA. The inset shows non-normalized emission spectrum of (A) the grating and (B) the unstructured gold surface. The differential spectrum is obtained by subtracting spectrum B from spectrum A, hence implying that the differential spectrum only consists of the impact of the grating, eliminating transient radiation and luminescence of the gold film. Theoretical predictions of wavelengths at which optimum detection of the decoupled radiation occur are indicated with the corresponding diffraction orders n; Bragg resonances, at which the decoupling is expected to be inhibited by the gratings, are indicated with corresponding resonance orders m.

3.6 Excitation of surface plasmons on an unstructured metal surface

In order to demonstrate the generation of traveling surface plasmon polariton waves on an unstructured metal surface, their propagation and controlled decoupling into light by a grating was studied, namely the dependence of the

optical emission as a function of distance R between the excitation point and the grating edge, as illustrated in Figure 3.16. This series of experiments was performed using the spot mode of excitation (see Section 3.3), with a spot diameter of about 1 μm (estimated using the technique described in Section 3.3.4), on the same 4.25 μm and 300 nm period gratings. The large spot size was used in order to allow higher beam current and more intense peaks in decoupled light. The spectrum of the signal detected by placing the electron beam at the edge of the 4.25 μm grating facing the mirror is essentially the same as in the scanning mode over the grating, with the only difference being that the negative values in the differential spectrum seen in Figure 3.12 at about $\lambda = 500$, 870 and 950 nm do not appear, corroborating with the idea that they are indeed relevant to the Bragg frequencies.

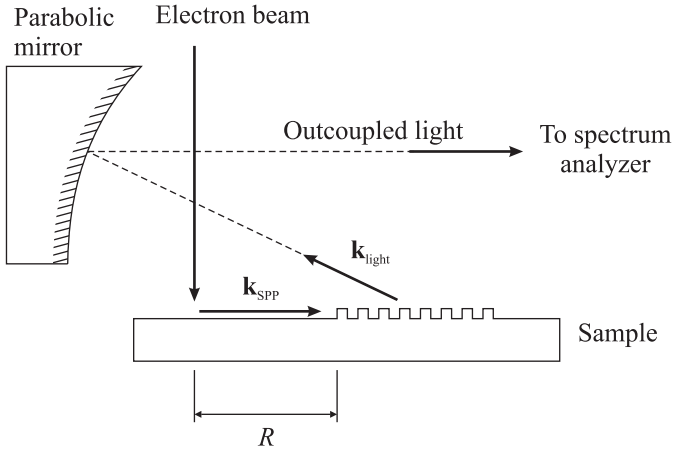

Figure 3.16: An injection of a beam of free electrons at a distance R from a grating on a metal film results in the excitation of surface plasmons $\mathbf{k}_{\mathrm{SPP}}$, propagating towards the grating and decoupling into light $\mathbf{k}_{\mathrm{light}}$. As the point of excitation is moved away from the grating, the spectrum should gradually change and the SPP component of emission diminish.

As the point of excitation is moved away from the grating, the spectrum gradually changes and the SPP component of emission diminishes, as shown in Figure 3.17 for 4.25 μm grating. The electron beam creates a source of surface plasmon polaritons at a distance R from the grating, and the diminishing of the SPP component in the detected spectra is due to SPP decay

over the distance R. For distances $R > 50$ μm the surface plasmon polariton component disappears as SPPs dissipate before they can be decoupled by the grating.

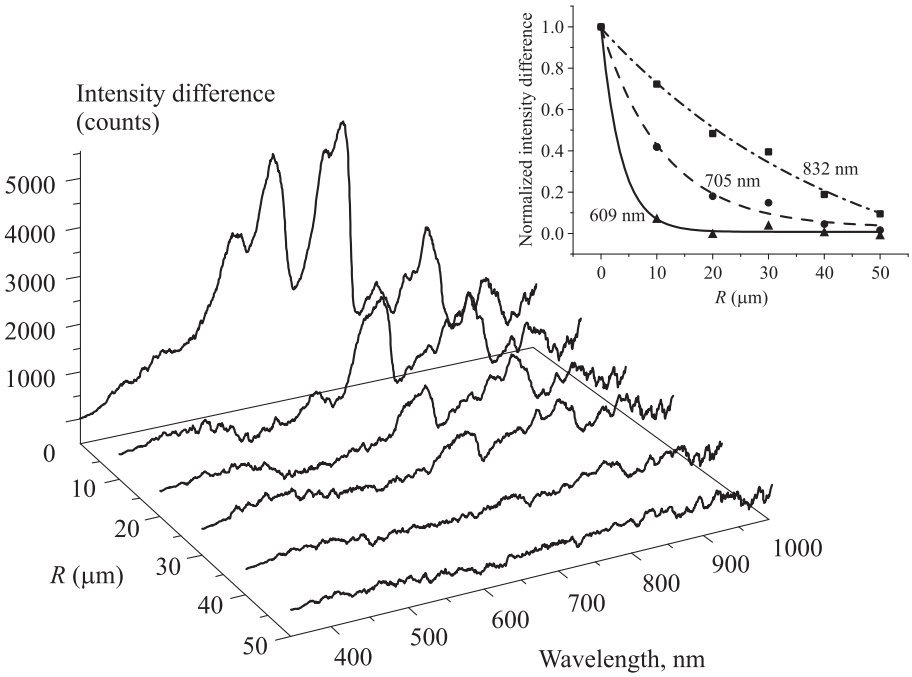

Figure 3.17: Decay of the SPPs as a function of distance R between the 4.25 μm grating edge and the electron injection point. The differential spectra were obtained by subtracting the spectrum sampled at $R = 60$ μm from the spectra sampled at shorter distances. The inset shows normalized intensities of decoupled SPP signal at different peak wavelengths as a function of distance R between the edge of the grating and the point of excitation.

This graph also illustrates that SPP waves corresponding to different parts of the emission spectrum decay with different pace (see inset into Figure 3.17). For a point-like source, the in-plane plasmon intensity is proportional to $\exp(-R/\xi)/R$. Due to the detection system, collecting light in a range of in-plane azimuthal angles, this leads to an $\exp(-R/\xi)$ dependence for the decoupled and detected signal, giving the experimental attenuation lengths $\xi_{609} = 5$ μm, $\xi_{705} = 11$ μm, and $\xi_{832} = 45$ μm. Indeed, plasmons corresponding to the vacuum wavelength of 609 nm shall be strongly attenuated by losses in gold with damping length rapidly increasing towards the infrared

part of the spectrum. This is also what was found in the experimental data. However, the experimentally derived energy attenuation lengths are somewhat shorter than predicted from the formula $\xi^t = (2|\mathrm{Im}\{k_{\mathrm{SPP}}\}|)^{-1}$, derived in Section 3.4, and the bulk values of the dielectric coefficient of gold (theoretical plasmon decay length are $\xi^t_{609} = 5.3$ μm, $\xi^t_{705} = 21$ μm, and $\xi^t_{832} = 54$ μm). This is explained by imperfections and granulation of the gold surface, providing an additional source for plasmon scattering losses.

The excitation, propagation and decoupling of the plasmons has also been demonstrated on a 300 nm grating. Plasmon emission spectra, obtained in spot mode at different distances from the grating, are depicted in Figure 3.18. The obtained value of the plasmon decay length (see inset in Figure 3.18) on $\lambda = 601$ is 4 μm and is consistent with the value $\xi^t_{601} = 4.9$ μm obtained from the formula $\xi = (2|\mathrm{Im}\{k_{\mathrm{SPP}}\}|)^{-1}$.

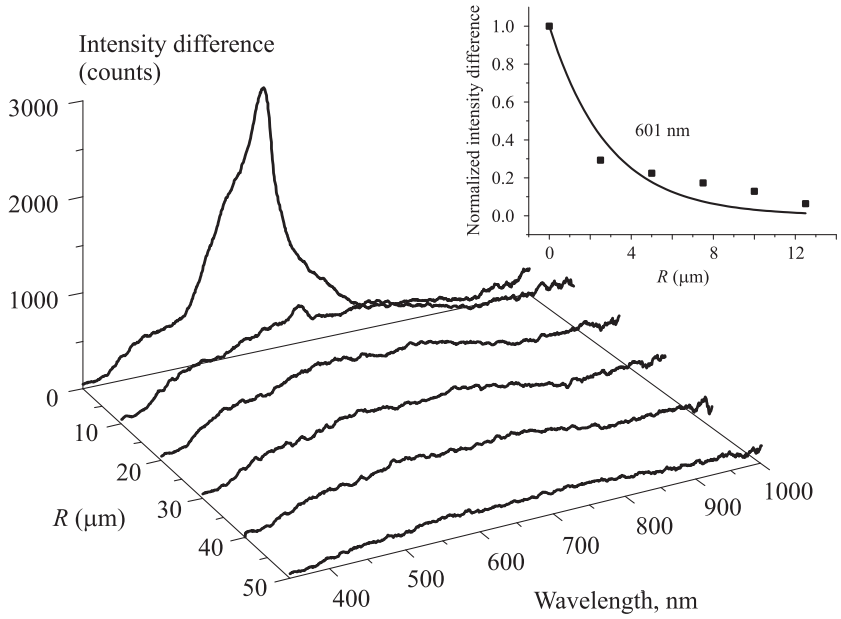

Figure 3.18: Decay of the SPPs as a function of distance R between the 300 nm grating edge and electron injection point. The differential spectra were obtained by subtracting the spectrum sampled at $R = 60$ μm from the spectra sampled at shorter distances. The inset shows normalized intensity of decoupled SPP signal $\lambda = 601$ nm as function of distance R between the edge of the grating and the point of excitation.

Therefore it has been demonstrated that an electron beam indeed creates a source of surface plasmon polaritons on an unstructured metal film. The plasmons were detected by a controlled decoupling into light with a grating at a distance from the excitation point. It was shown that the spectra of the decoupled SPPs dissipates as the distance between the electron beam and the grating increases. Moreover, SPP waves corresponding to different parts of the emission spectrum decay with differing pace, allowing plasmon decay length estimation. Obtained values of SPP decay lengths are consistent with the ones predicted by theory, although experimental values were shorter than theoretical. This is explained by imperfections and granulation of the gold surface, providing an additional source for plasmon scattering losses. The properties of the surface plasmon polariton source generated on an unstructured metal surface by an electron beam, such as the mechanism of generation, the power, the efficiency and the localization of the source are detailed in the following Section.

3.7 SPP source generated on a metal surface by an electron beam

All the observations, in particular the wavelength dependent decay of the emission spectrum with the distance between the excitation point and the grating, prove that electron beam excitation indeed provides a source of SPPs. In this Section the main characteristics of the source are described in detail.

3.7.1 Mechanism, efficiency and power of the SPP source

The plasmon emission spectrum largely correlates with the spectrum of unstructured gold emission as shown in graph B of Figure 3.12, suggesting that the dominant contribution to SPP generation comes from the recombination of *d*-band holes created by electron beam excitation [81], rather than from

direct scattering of free electrons [82]. Therefore, it appears that the plasmon emission spectrum, as is the case of the spectrum of luminescence, is also strongly connected to the energy separation between d holes and the Fermi surface [80]. The *mechanism* of the generation of surface plasmons using Fermi surface formalism is depicted in Figure 3.19.

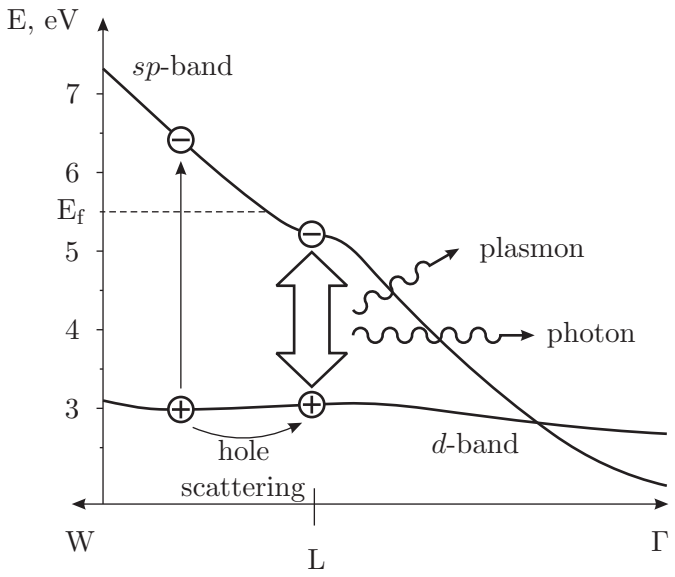

Figure 3.19: Schematic representation of $d \rightarrow sp$ interband excitation and subsequent hole relaxation close to the L point of the band structure of gold. Electrons are promoted from the d-band into the sp-band well above the Fermi level. The holes in the d band undergo Auger scattering and hole–phonon scattering. Direct radiative recombination of a d-band hole with an electron in the sp-band below the Fermi surface or emission of a plasmon may occur. The PP subsequently decays either radiatively or nonradiatively [81].

The bombardment of the metal film with free electrons results the in generation of holes in the d-band of the film as a result of promotion of the conducting electrons in the film to the sp-band. Subsequent recombination of the d-band holes with the sp-band electrons occurs due to the Auger and hole-phonon scattering of the holes in the d band and relaxation of the electrons below Fermi energy. This recombination can result in the emission of a photon or the generation of a plasmon, which can decay radiatively or nonradiatively. At high excitation energy a large number of transitions

near X and L points may be involved in forming the emission spectrum [83, 84], which also depends on the quality of the surface [85].

The *efficiency* of the generated plasmon source has been measured as a ratio between the energy of the generated plasmons and the energy of the corresponding electron beam. In a series of experiments performed in spot mode on a 300 nm period grating the acceleration voltage of the electron beam has been varied in the 5–45 keV range and the energy of the generated plasmon source estimated. The results, depicted in Figure 3.20, show an exponential decrease of the efficiency of the plasmons source with increasing acceleration voltage that can be explained by reduction in the number of electrons depositing energy in the skin layer of the metal film.

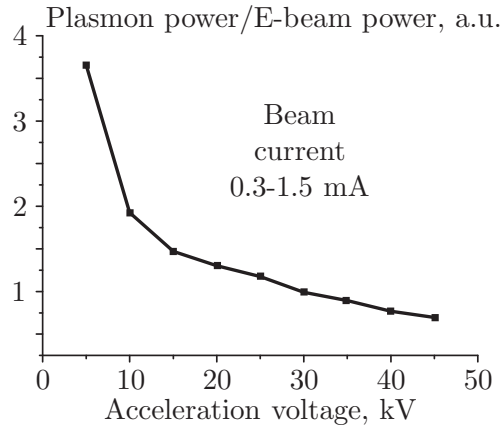

Figure 3.20: Efficiency of plasmon generation by an electron beam as a function of acceleration voltage measured as a ratio between a power of the plasmon source generated on a 300 nm grating and the power of the electron beam.

From the experimental data, one can obtain an estimate of the order of magnitude of the total *power* of the SPP source at the point of excitation. At the electron beam current of 10 μA, or equivalently 6×10^{13} electrons per second, the plasmon-related photons were detected at the rate of 5×10^5 s^{-1} across the spectrum. A rough estimate of the quantum efficiency of the light decoupling, collection and detection system performed in Section 3.3, is about 10^{-5}. This corresponds to a SPP source with a total power of 10 nW, generating 3×10^{10} SPPs per second at the point of excitation. The

corresponding probability for a single electron to excite a SPP is then 3×10^{-4}, which is consistent with references [82, 86].

3.7.2 SPP source localization

Surface plasmon polaritons propagate on a metal–dielectric interface and are tightly coupled to the boundary between two media. In the metal (as well as in a dielectric) the intensity of the SPPs decays exponentially from the interface. Therefore it can be assumed that the generation of surface plasmon polaritons by an electron beam occurs in the top layer of the metal, characterized by skin depth δ (see Section 3.4).

The localization of the source of SPPs created by a beam of electrons on a metal surface largely depends on the size of the electron beam. However, even if the incident electron beam was focused into a point, the SPPs would still be generated at a distance from the point where it hits the surface. Three factors leading to this can be considered.

First of all, the *broadening* of the electron beam inside the sample due to the electron scattering (see Figure 3.21a). The amount b_{br} by which the beam of energy E_0 is expanded passing through a sample of thickness t, the atomic number Z and the density ρ can be estimated [87] using the equation:

$$b_{\mathrm{br}} \approx (0.47\ \mathrm{nm})(\rho Z)^{1/2}(100\ \mathrm{keV}/E_0)[t/50\ \mathrm{nm}]^{3/2}. \tag{3.21}$$

The amount of electron beam broadening in the skin depth layer of the gold film ($t = 20$ nm at $\lambda = 500$ nm) and 50 keV electron beam is $b_{\mathrm{br}} \approx 10$ nm. The beam broadening can be made insignificant by using high acceleration voltages or metals with small skin depths.

The second factor to be considered is the *delocalization* of electrons, a well-known subject [88–91] in energy electron loss spectroscopy (EELS). The problem can be illustrated by the following example: how far from a silicon atom must the electron probe be before the Si edge can be detected? The classical explanation was offered by Niels Bohr in 1913 [92]. The incident electron is represented as a particle e^- that interacts via the Coulomb force with a bound atomic electron e_b^-, represented as a classical oscillator of

angular frequency ω (see Figure 3.21b). Several pages of non-relativistic mechanisms led to an expression for the energy loss ΔE of the incident electron when the latter moves at speed v along an approximately linear path with impact parameter b:

$$\Delta E(b) = E_R(b\omega/v)^2\{[K_0(b\omega/v)]^2 + [K_1(b\omega/v)]^2\}. \tag{3.22}$$

Here $E_R = (k_c^2 e^4/E_0)(1/b^2)$ is the Rutherford recoil energy that would be imparted to a stationary free electron, $k_c = (4\pi\varepsilon_0)^{-1}$ is the Coulomb constant and K_0 and K_1 are modified Bessel functions. For $b \ll v/\omega$, the energy exchange is approximately E_R: the atomic electron has sufficient time to move during transit of the incident electron and receives the same momentum as a free electron. For $b \gg v/\omega$, however, the atomic eletron moves in response to the electric field of the incident electron, resulting in very little energy exchange, represented by the rapidly falling modified-Bessel terms in Equation (3.22). Therefore the inelastic scattering is often taken to be confined to impact parameters below v/ω and a localization range taken as:

$$b_{\text{del}} = v/\omega. \tag{3.23}$$

according to these classical physics arguments.

At distances beyond the Bohr's cutoff b_{del} the target is "dynamically screened". The dynamical screening arises from the more slowly varying electric field seen at large distances, rather than any property of the intervening medium and so will be expected in free space as well. Rigorous theoretical considerations of the problem show that the classical model overestimates the delocalization, although values of b_{del} given by Equation (3.23) are still practical. In the considered case of broadening the SPP source, ω in the Equation (3.23) is the frequency of the excited surface plasmon polariton. For 50 keV electron beam and $\lambda = 500$ nm the delocalization parameter is $b_{\text{del}} \approx 30$ nm. The delocalization is a fundamental factor representing a basic limit of the size of the generated source of surface plasmon polaritons, imposed by the properties of the electron. Unlike the broadening of the electron beam, it does not depend on the design of the microscope.

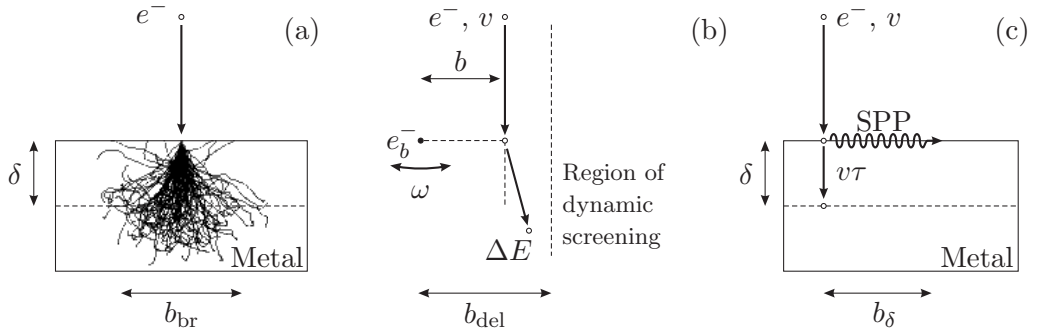

Figure 3.21: Mechanisms contributing to the localization of the source of surface plasmon polaritons generated by an electron beam on a metal surface. Broadening of the beam of electrons e^- in skin depth layer δ of the metal due to scattering b_{br} (a). Inelastic scattering of a fast moving incident electron e^- on a bound atomic electron e_b^-, according to the classical particle analysis of Bohr [92], is confined to impact parameters below $b_{\mathrm{del}} = v/\omega$ (b). The incident electron is therefore delocalized due to the Coulomb interaction with bound atomic electrons. Broadening of the SPP source due to the finite speed of the electron in the skin depth layer of the metal (c). Within the time $\tau = \delta/v$ it takes the electron e^- propagating with speed v to reach the bottom interface of the skin depth layer, the SPP generated at the top interface propagates to the distance $b_\delta = c\tau$.

The third mechanism relates to the finite speed of the electron, generating SPPs, in the skin depth layer of the metal δ. Consider an electron propagating at speed v and generating surface plasmon polaritons at both top and bottom interfaces of the skin depth layer whilst losing an insignificant part of its energy. By the time $\tau = \delta/v$ it will take the electron to propagate through the skin depth layer of the metal, the surface plasmon polaritons generated at the top interface of the layer will have propagated to the distance:

$$b_\delta = c\tau = c\frac{\delta}{v}, \tag{3.24}$$

which will lead to the broadening of the SPP source, as illustrated in Figure 3.21c. If the speed of the electron was infinite, the surface plasmon polaritons generated at top and bottom interfaces of the skin depth would start propagating at the same time, so the broadening of the SPP source is zero. For a 50 keV beam the speed of the electrons is $v \approx 0.41c$, so the broadening of the SPP source due to the finite speed of the electron in the skin depth is $b_\delta \approx 48$ nm.

The contribution of the beam scattering inside the sample, delocalization of the electrons due to Coulomb interaction and broadening due to the finite electron speed mechanisms to the localization of the source of surface plasmon polaritons generated by the beam of free electrons on the gold film as a function of electron beam energy is presented in Table 3.1. It should be noted that the Equations (3.21), (3.23) and (3.24) used to estimate the corresponding values were derived by elementary assumptions resulting in overestimations of the input of each factor.

E, keV	b_{br}, nm	b_{del}, nm	b_{δ}, nm
5	93	11	144
10	47	16	103
20	23	22	74
30	15	26	61
40	12	29	53
50	10	33	48

Table 3.1: Parameters of SPP source localization on a gold film as a function of electron beam energy E: broadening of the electron beam in the skin depth layer b_{br} [Eq. (3.21)], delocalization of the electrons due to Coulomb interaction b_{del} [Eq. (3.23)] and broadening of the source due to the finite speed of electron in the skin depth layer b_{δ} [Eq. (3.24)]. The presented values overestimate the contribution of these mechanisms.

The broadening and the delocalization of the electron beam are the basic limiting factors not only for the problem of SPP generation, but for all scanning and transmission electron microscopy techniques. However, subnanometer measurements with these techniques has been demonstrated suggesting that those basic limits can be either overcome or made negligible. It can, therefore, be suggested that the demonstrated localization of the SPP source, roughly 1 μm, can be significantly improved.

The size of the generated source of SPPs can be measured experimentally by imaging the plasmonic excitations on the nanostructure with features of known size. This can be done by repositioning the electron beam in spot mode across the structure in a regular manner (scanning) and recording the plasmon spectral response from each point at one or several wavelengths.

The resolution of the obtained "plasmonic image" would give an estimate of the localization of the SPP source similarly to the way that the secondary electron image gives an estimate to the size of the electron beam, as shown in Section 3.3.4. The technique allowing acquisition of "plasmonic images" at different wavelengths, and estimation of the localization of the SPP source generated by a free electron beam, has been realized, and is described in the following Chapter. The localization of the SPP source generated by a beam of free electrons on a gold film up to 30 nm is demonstrated.

It has therefore been demonstrated that the mechanism of SPP generation by an electron beam is a recombination of *d*-band holes and *sp*-electrons. The power of the source at the point of excitation was estimated to be ~ 10 nW. It was demonstrated that the efficiency of the plasmon source decreases with the increasing acceleration voltage due to the reduction of the number of electrons in the skin layer of the metal film. The main factors defining the localization of the source have been identified and the contribution of each factor to the broadening of the SPP source estimated.

3.8 Summary and conclusions

An experimental setup, allowing for probing the optical properties of metallic and dielectric structures with a nanoscale resolution in the 350–1150 nm spectral range, was built. The setup is based on a scanning electron microscope with a cathodoluminescence light collection system and a spectrum analyzer. The system was used to demonstrate the excitation of propagating surface plasmon waves on an unstructured metal surface by a beam of free electrons.

It was shown that the electron beam-induced spectrum of light emission from a grating manufactured on a gold surface has specific features, as compared to the emission spectrum from an unstructured metal film, due to the excitation of surface plasmon polaritons. The position of peaks and dips in the plasmon-related emission spectrum was predicted by a theoretical approach based on k-vector formula for the outcoupling of plasmons by a grating and Bragg resonances. The theoretical values correlate remarkably well with the experimental results.

The generation of traveling surface plasmon polariton waves on an unstructured gold surface by a beam of free electrons has been demonstrated by the study of the dependence of the optical emission as a function of distance between the excitation point and the grating edge. As the point of excitation is moved away from the grating, the plasmon-related spectrum gradually changed and the SPP component of emission diminished.

Decay lengths of propagating surface plasmon polaritons generated by a beam of free electrons on an unstructured gold surface were measured. The experimental values appeared to be less than ones predicted by theory. This is explained by imperfections and granulation of the gold surface, providing an additional source for plasmon scattering losses.

The dominant mechanism of the generated source of surface plasmon polaritons was identified as the recombination of the *d*-band holes with the *sp*-band electrons due to the large correlation between the spectrum of decoupled surface plasmon polaritons and the spectrum of the unstructured surface of a gold film excited by an electron beam.

The power of the source of surface plasmons generated by a beam of free electrons on an unstructured gold surface was estimated to be $\sim$ 10 nW, which is consistent with the data found in literature. It was demonstrated that the efficiency of the plasmon source decreases with the increasing acceleration voltage due to the reduction of the number of electrons in the skin layer of the metal film.

The experimental setup, described in this Chapter, was improved for further research by the introduction of a more efficient parabolic mirror with a short focal distance. This modification enabled the development of the a imaging technique of plasmonic nanostructures: Hyperspectral imaging with an electron beam, described in the following Chapter.

Shortly after the original publication [65], the excitation of surface plasmon polaritons with an electron beam has been demonstrated by the groups of Professor H. A. Atwater and Professor P. Polman [93]. The scanning electron microscope with a cathodoluminescence system was used to demonstrate plasmon damping and propagation on both silver and gold films. Theoretical estimates of loss mechanisms, such as absorption and leakage radiation, were

made. It was confirmed that the electron beam generates propagating surface plasmons on a metal film, and plasmon decay lengths have been obtained for different wavelengths. As in the described research, the measured decay lengths were found to be shorter than the ones predicted by the theory.

To summarize, it has been shown that electron beam excitation of an unstructured gold surface provides a potentially highly localized source of propagating surface plasmons. This may be the technique of choice for creating the high density of plasmons necessary for demonstrating nonlinear regimes of SPP propagation, and also for achieving a high density of plasmons in the active media of SPASER applications [94].

3.9 References

[1] V.M. Agranovich and D.L. Mills, editors. *Surface polaritons*. North Holland Co, 1982.

[2] A.D. Boardman, editor. *Electromagnetic surface modes*. Wiley, 1982.

[3] H. Raether. *Surface plasmons on smooth and rough surfaces and gratings*. Springer-Verlag, 1988.

[4] V.M. Shalaev and S. Kawata, editors. *Nanophotonics with surface plasmons*. Elsevier Science, 2007.

[5] S.A. Maier. *Plasmonics: fundamentals and applications*. Springer, 2007.

[6] S.I. Bozhevolnyi, V.S. Volkov, E. Devaux, J.Y. Laluet, and T.W. Ebbesen. Channelling surface plasmons. *Appl. Phys. A*, 2007.

[7] P. Berini, R. Charbonneau, and N. Lahoud. Long-range surface plasmons on ultrathin membranes. *Nano Lett.*, 2007.

[8] W.L. Barnes, A. Dereux, and T.W. Ebbesen. Surface plasmon subwavelength optics. *Nature*, 424:824, 2003.

[9] A.V. Zayats and I.I. Smolyaninov. Near-field photonics: surface plasmon polaritons and localized surface plasmons. *J. Opt. A*, 5:S16, 2003.

[10] F. Caruso. Nanoengineering of particle surfaces. *Adv. Mat.*, 13(1):11, 2001.

[11] Y. Xia, P. Yang, Y. Sun, Y. Wu, B. Mayers, B. Gates, Y. Yin, F. Kim, and H. Yan. One-dimensional nanostructures: synthesis, characterization, and applications. *Adv. Mat.*, 15(5):353, 2003.

[12] E. Hutter and J.H. Fendler. Exploitation of localized surface plasmon resonance. *Adv. Mat.*, 16(19):1685, 2004.

[13] F. Patolsky and C.M. Lieber. Nanowire nanosensors. *Mat. Today*, 8(4):20, 2005.

[14] Y. Li, F. Qian, J. Xiang, and C.M. Lieber. Nanowire electronic and optoelectronic devices. *Mat. Today*, 9(10):18, 2006.

[15] P. Avouris and J. Chen. Nanotube electronics and optoelectronics. *Mat. Today*, 9(10):46, 2006.

[16] L.J. Guo. Nanoimprint lithography: Methods and material requirements. *Adv. Mat.*, 19(4):495, 2007.

[17] S.I. Bozhevolnyi, V.S. Volkov, E. Devaux, J.Y. Laluet, and T.W. Ebbesen. Channel plasmon subwavelength waveguide components including interferometers and ring resonators. *Nature*, 440(7083):508, 2006.

[18] S.A. Maier, M.D. Friedman, P.E. Barclay, and O. Painter. Experimental demonstration of fiber-accessible metal nanoparticle plasmon waveguides for planar energy guiding and sensing. *Appl. Phys. Lett.*, 86(7), 2005.

[19] B. Wang and G.P. Wang. Plasmonic waveguide ring resonator at terahertz frequencies. *Appl. Phys. Lett.*, 89(13), 2006.

[20] J.C. Weeber, A.L. Baudrion, A. Bouhelier, A. Bruyant, G.C.D. Francs, R. Zia, and A. Dereux. Efficient surface plasmon field confinement in one-dimensional crystal line-defect waveguides. *Appl. Phys. Lett.*, 89(21), 2006.

[21] A.V. Krasavin, A.V. Zayats, and N.I. Zheludev. Active control of surface plasmon-polariton waves. *J. Opt. A*, 7:S85, 2005.

[22] B. Liedberg, C. Nylander, and I. Lundstrum. Surface plasmon resonance for gas detection and biosensing. *Sensors and Actuators B*, 4:299, 1983.

[23] M. Malmqvist. Biospecific interaction analysis using biosensor technology. *Nature*, 361:186, 1993.

[24] D. Habauzit, J. Chopineau, and B. Roig. SPR-based biosensors: a tool for biodetection of hormonal compounds. *Anal. Bioanal. Chem.*, 387(4):1215, 2007.

[25] M.L. Brongersma and P.G Kik, editors. *Surface plasmon nanophotonics*. Springer, 2007.

[26] A. Sommerfeld. *Ann. Phys. Chem*, 67:233, 1899.

[27] J. Zenneck. *Ann. Phys.*, 23:846, 1907.

[28] R.W. Wood. On a remarkable case of uneven distribution of light in a diffraction grating spectrum. *Phil. Mag.*, 4:396, 1902.

[29] R.W. Wood. *Phil. Mag.*, 23:310, 1912.

[30] R.W. Wood. *Phys. Rev.*, 48:928, 1935.

[31] U. Fano. The theory of anomalous diffraction gratings and of quasi-stationary waves on metallic surfaces (Sommerfeld's waves). *J. Opt. Soc. Am.*, 31:213, 1941.

[32] D. Pines. Collective energy losses in solids. *Rev. Mod. Phys.*, 28:184, 1956.

[33] U. Fano. Atomic theory of electromagnetic interactions in dense materials. *Phys. Rev.*, 103:1202, 1956.

[34] R.H. Ritchie. Plasma losses by fast electrons in thin films. *Phys. Rev.*, 106(5):874, 1957.

[35] R.H. Ritchie, E.T. Arakawa, J.J. Cowan, and R.N. Hamm. Surface-plasmon resonance effect in grating diffraction. *Phys. Rev. Lett.*, 21(22):1530, 1968.

[36] D. Beaglehole. Coherent and incoherent radiation from optically excited surface plasmons on a metal grating. *Phys. Rev. Lett.*, 22(14):708, 1969.

[37] A. Otto. Excitation of nonradiative surface plasma waves in silver by the method of frustrated total reflection. *Z. Physik A*, 216(4):1431, 1968.

[38] E. Kretschmann and H. Raether. Radiative decay of nonradiative surface plasmons excited by light. *Z. Naturforsch*, 23:2135, 1968.

[39] R.C. Reddick, R.J. Warmack, and T.L. Ferrell. New form of scanning optical microscopy. *Phys. Rev. B*, 39(1):767, 1989.

[40] D. Courjon, K. Sarayeddine, and M. Spajer. Scanning tunneling optical microscopy. *Opt. Comm.*, 71(1):23, 1989.

[41] U.Ch. Fischer and D.W. Pohl. Observation of single-particle plasmons by near-field optical microscopy. *Phys. Rev. Lett.*, 62(4):458, 1989.

[42] F. de Fornel, J.P. Goudonnet, L. Salomon, and E. Lesniewska. An evanescent field optical microscope. *Proc. SPIE*, 1139:77, 1989.

[43] O. Marti, H. Bielefeldt, B. Hecht, S. Herminghaus, P. Leiderer, and J. Mlynek. Near-field optical measurement of the surface plasmon field. *Opt. Comm.*, 96(4):225, 1993.

[44] D.P. Tsai, J. Kovacs, Zh. Wang, M. Moskovits, V.M. Shalaev, J.S. Suh, and R. Botet. Photon scanning tunneling microscopy images of optical excitations of fractal metal colloid clusters. *Phys. Rev. Lett.*, 72(26):4149, 1994.

[45] S.I. Bozhevolnyi, I.I. Smolyaninov, and A.V. Zayats. Near-field microscopy of surface-plasmon polaritons: localization and internal interface imaging. *Phys. Rev. B*, 51(24):17916, 1995.

[46] S.I. Bozhevolnyi, B. Vohnsen, I.I. Smolyaninov, and A.V. Zayats. Direct observation of surface polariton localization caused by surface roughness. *Opt. Comm.*, 117(5):417, 1995.

[47] J.R. Krenn, H. Ditlbacher, G. Schider, A. Hohenau, A. Leitner, and F.R. Aussenegg. Surface plasmon micro- and nano-optics. *J. Microscopy*, 209:167, 2003.

[48] C.J. Powell and J.B. Swan. Origin of the characteristic electron losses in aluminum. *Phys. Rev.*, 115(4):869, 1959.

[49] C.J. Powell and J.B. Swan. Origin of the characteristic electron energy losses in magnesium. *Phys. Rev.*, 116(1):81, 1959.

[50] Y.Y. Teng and E.A. Stern. Plasma radiation from metal grating surfaces. *Phys. Rev. Lett.*, 19(9):511, 1967.

[51] D. Heitmann. Radiative decay of surface plasmons excited by fast electrons on periodically modulated silver surfaces. *J. Phys. C*, 10:397, 1977.

[52] D. Heitmann. Theory and experiment of light-emission of surface-plasmons induced by fast electrons on modulated surfaces. *Physica Status Solidi B*, 88(2):493, 1978.

[53] H. Raether. Surface-plasmons on smooth and rough surfaces and on gratings. *Springer Tracts In Modern Physics*, 111:1, 1988.

[54] D. Heitmann. Surface-dimensional and two-dimensional plasmon excitations in microstructured metal-films and semiconductor heterostructures. *Physica Scripta*, T25:294, 1989.

[55] P. Tran, V. Celli, and A.M. Marvin. K gaps for surface-polaritons on gratings: Excitation by fast electrons. *Phys. Rev. B*, 42(1):1, 1990.

[56] B. Fischer, T.M. Fischer, and W. Knoll. Dispersion of surface-plasmons in rectangular, sinusoidal, and incoherent silver gratings. *J. Appl. Phys.*, 75(3):1577, 1994.

[57] Z. Szentirmay. Surface-plasmon assisted electron photon interaction in metal-oxide metal layered structures. *Progr. Quant. Electr.*, 15(3):175, 1991.

[58] D. Heitmann and V. Permien. Transition radiation from rough surfaces. *Opt. Comm.*, 25(2):196, 1978.

[59] D.G. Hall and A.J. Braundmeier. Dispersion-relation for surface-plasmons on randomly rough surfaces — quantum-mechanical approach. *Phys. Rev. B*, 17(10):3808, 1978.

[60] D. Heitmann, N. Kroo, C. Schulz, and Z. Szentirmay. Dispersion anomalies of surface-plasmons on corrugated metal-insulator interfaces. *Phys. Rev. B*, 35(6):2660, 1987.

[61] K.D. Zhu and S.W. Gu. Quantum-theory of surface-polaritons on a rough-surface. *Comm. Theor. Phys.*, 17(3):291, 1992.

[62] H.D. Hattendorff. Transition radiation from gold and silver films bombarded with 80 keV electrons. *Physica Status Solidi A*, 42(2):489, 1977.

[63] N. Yamamoto and A. Toda. Imaging of Cherenkov and transition radiation from thin-films and particles. *Scanning Microscopy*, 9(3):669, 1995.

[64] S. Egusa, Y.H.L. Liau, and N.F. Sherer. Imaging scanning tunneling microscope-induced electroluminescence in plasmonic corrals. *Appl. Phy. Lett.*, 84(8):1257, 2004.

[65] M.V. Bashevoy, F. Jonsson, A.V. Krasavin, N.I. Zheludev, Y. Chen, and M.I. Stockman. Generation of traveling surface plasmon waves by free-electron impact. *Nano Lett.*, 6(6):1113, 2006.

[66] B.G. Yacobi and D.B. Holt. *Cathodoluminescence microscopy of inorganic solids*. Springer, 1990.

[67] K. Kanaya and S. Okayama. Penetration and energy-loss theory of electrons in solid targets. *J. Phys. D*, 5(1):43, 1972.

[68] P.J. Goodhew, J. Humphreys, and R. Beanland. *Electron microscopy and analysis*. London: Taylor and Francis, 2001.

[69] J.I. Goldstein, D.E. Newbury, P. Echlin, D.C. Joy, C. Fiori, and E. Lifshin. *Scanning electron microscope and x-ray analysis*. New York: Plenum Press, 1981.

[70] L. Reimer. *Scanning electron microscopy*. Berlin: Springer-Verlag, 1998.

[71] D.B. Williams and C.B. Carter. *Transmission electron microscopy: a textbook for materials science*. New York: Plenum Press, 1996.

[72] D. Chescoe and P.J. Goodhew. *The operation of transmission and scanning microscopes*. Oxford: BIOS, 1990.

[73] R.J. Keyse, A.J. Garratt-Reed, P.J. Goodhew, and G.W. Lorimer. *Introduction to scanning transmission electron microscopy*. Oxford: BIOS, 1998.

[74] A.V. Moskalenko, D.J. Burbridge, G. Viau, and S.N. Gordeev. Electron-beam-induced welding of 3D nano-objects from beneath. *Nanotechnology*, 18(2):025304, 2007.

[75] A.V. Zayats, I.I. Smolyaninov, and A.A. Maradudin. Nano-optics of surface plasmon polaritons. *Phys. Rep.*, 408:131, 2005.

[76] J.M. Pitarke, V.M. Silkin, E.V. Chulkov, and P.M. Echenique. Theory of surface plasmons and surface-plasmon polaritons. *Rep. Progr. Phys.*, 70(1):1, 2007.

[77] A.V. Krasavin, K.F. MacDonald, N.I. Zheludev, and A.V. Zayats. High-contrast modulation of light with light by control of surface plasmon polariton wave coupling. *Appl. Phys. Lett.*, 85(16):3369, 2004.

[78] A.V. Krasavin and N.I. Zheludev. Active plasmonics: controlling signals in Au/Ga waveguide using nanoscale structural transformations. *Appl. Phys. Lett.*, 84(8):1416, 2004.

[79] A.V. Krasavin, K.F. MacDonald, and N.I. Zheludev. *Active plasmonics*. Nanophotonics with Surface Plasmons. Elsevier Science, 2007.

[80] M.R. Beversluis, A. Bouhelier, and L. Novotny. Continuum generation from single gold nanostructures through near-field mediated intraband transitions. *Phys. Rev. B*, 68:115433, 2003.

[81] E. Dulkeith, T. Niedereichholz, T.A. Klar, J. Feldmann, G. von Plesse, D.I. Gittins, K.S. Mayya, and F. Caruso. Plasmon emission in photoexcited gold nanoparticles. *Phys. Rev. B*, 70:205424, 2004.

[82] R.H. Ritchie. The interaction of swift electrons with surface excitations. *J. Physics*, 5:A17, 1993.

[83] G.T. Boyd, Z.H. Yu, and Y.R. Shen. Photoinduced luminescence from the noble metals and its enhancement on roughened surfaces. *Phys. Rev. B*, 33(12):7923, 1986.

[84] P. Apell, R. Monreal, and S. Lundqvist. Photoluminescence of noble metals. *Physica Scripta*, 38:174, 1988.

[85] M.L. Theye. Investigation of the optical properties of Au by means of thin semitransparent films. *Phys. Rev. B*, 2(8):3060, 1970.

[86] R.A. Ferrell. Predicted radiation of plasma oscillations in metal films. *Phys. Rev.*, 111(5):1214, 1958.

[87] R.F. Egerton. Limits to the spatial, energy and momentum resolution of electron energy-loss spectroscopy. *Ultramicroscopy*, 107(8):575, 2007.

[88] R.F. Egerton. *Electron energy-loss spectroscopy in the electron microscope*. New York: Plenum, 1996.

[89] M. Isaacson and J.P. Langmore. Determination of the non-localization of the inelastic scattering of electrons by electron microscopy. *Optik*, 41(1):92, 1974.

[90] D.A. Muller and J. Silcox. Delocalization in inelastic scattering. *Ultramicroscopy*, 59:195, 1995.

[91] M.P Oxley, E.C. Cosgriff, and L.J. Allen. Nonlocality in imaging. *Phys. Rev. Lett.*, 94(20):203906, 2005.

[92] N. Bohr. *Philos. Mag.*, 25:10, 1913.

[93] J.T. van Wijngaarden, E. Verhagen, A. Polman, C.E. Ross, H.J. Lezec, and H.A. Atwater. Direct imaging of propagation and damping of near-resonance surface plasmon polaritons using cathodoluminescence spectroscopy. *Appl. Phys. Lett.*, 88:221111, 2006.

[94] D.J. Bergman and M.I. Stockman. Surface plasmon amplification by stimulated emission of radiation: Quantum generation of coherent surface plasmons in nanosystems. *Phys. Rev. Lett.*, 90(2):027402, 2003.

Chapter 4

Hyperspectral imaging of plasmonic nanostructures with nanoscale resolution

4.1 Synopsis

The hyperspectral imaging technique for surface plasmon polaritons on metallic nanostructures has been implemented for the first time. This technique uses a scanning electron beam and allows for simple visualization of light emission from decoupled plasmons, providing information on decay lengths and feature sizes with nanometer resolution.

The concept of the hyperspectral imaging technique (HSI) of plasmonic nanostructures with an electron beam, and the requirements imposed on the experimental setup by HSI are outlined in Section 4.3. The description of the experimental setup used to realize HSI, including the implementation of a wide-angle parabolic mirror, spectral calibration of a new system and estimates of efficiency, are provided in the following Section. The results obtained for two different gratings and two light collection geometries, one with a narrow-angle and another with a wide-angle parabolic mirror, are presented and discussed in Section 4.5. The estimation of the delocalization (broadening of the source compared to the size of the electron beam) of the SPP source, generated by an electron beam, with the hyperspectral imaging of the diffraction grating, is detailed in Section 4.6.

4.2 Introduction

Surface plasmon polariton (SPP) waves are electromagnetic field oscillations propagating at metal–dielectric interfaces, which currently attract considerable interest in the fields of optics and surface science due to their ability to concentrate and channel radiation in the visible and near infrared spectral ranges using sub-wavelength structures [1–5]. In particular, SPP's are seen to have great potential for application as information carriers in highly integrated plasmonic devices and next-generation computer processor architectures. The ability to visualize surface plasmon polariton propagation or localized plasmon fields on nanostructures is essential for the development of such devices [6].

With the development of scanning probe techniques it became possible to study the properties of surface plasmon polaritons virtually at the surface along which the SPP propagates with a resolution in the nanometer range [7]. The first scanning probe technique applied to study SPPs was an electron scanning tunnelling microscope (STM) relying on the detection of the additional tunnelling current induced by surface polaritons [8–11] or the far-field scattered light due to the local SPP interaction with the STM tip [12]. In another approach, a dielectric SiN probe of an atomic force microscope (AFM) was used instead of an STM tip [13, 14]. It was realized later that although such approaches provide, in a first approximation, information on the SPP field in the probe tip position, the metal or silicon tips introduce significant perturbations in the SPP field due to the field enhancement effects related to excitation of localized surface plasmons and the lightning-rod effect (geometrical field enhancement at a surface of large curvature) at the tip–surface junction [15, 16]. These effects, depending in a complex non-linear manner on both the tip and surface defect topology and size as well as on their mutual position and orientation, prevent the direct measurement of the local SPP field on a surface [15].

A scanning nearfield optical microscope (SNOM) with uncoated optical fibre tips provides the possibility to probe the surface polariton field directly over a surface [10]. The low dielectric constant of glass (compared with silicon

or metal), as well as having a distance between the probe tip and the surface that is more than two orders of magnitude larger than in the STM, ensures minimal perturbation of the SPP field.

SNOM applications in studies of surface plasmon polaritons brought forth a new technique which provides the possibility to excite SPP locally at a given place on a surface [17]. Using illumination through a SNOM fibre tip, circular SPP waves can be locally launched at the surface. A number of fascinating phenomena resulting from SPP scattering by surface inhomogeneities has been studied with SNOM techniques over the years [18]: localization by random roughness [19], local SPP excitation and scattering [17, 20], SPP manipulation with a specially configured set of microscatterers [21], individual surface defects [22] and lithographically created microstructures [23]. Recently the SNOM technique has been used to map the surface plasmon intensity on nanostructured gold [24–26] and nanoparticle dimers and trimers [27, 28]. However, the question of what is actually seen on SNOM images has yet to be properly clarified [29]. Even the formation of the SNOM images, which are related to scattered SPPs that have the same spatial frequency in the imaging plane, is not that simple.

As an alternative, electron energy-loss spectroscopy (EELS) in a scanning transmission electron microscope (STEM) has been used for decades to detect surface plasmons, usually by focusing the electron beam on a metal surface and measuring the energy lost by the beam. Unlike light, an electron beam can excite both surface and bulk plasmons from planar surfaces. EELS has been used to detect plasmons from single spheres [30], coupled spheres [31] and supported spheres [32]. Recently EELS was used to demonstrate the excitation of various localized plasmon modes on a single nanoparticle [33, 34]. One major limitation of the EELS technique is that the low-energy part of the spectrum is usually masked by the tail of the so-called zero-loss peak, that is, the peak of electrons interacting elastically or encountering losses too small to be experimentally resolved.

A scanning transmission electron microscope with a cathodoluminescence system was used by the group of Professor Naoki Yamamoto to study plasmonic excitations [35, 36]. This technique was first applied to the study of

localized luminescence properties originating from defects and nanostructures in semiconductors [37, 38]. Recently, the technique was applied to the study of plasmonic excitations on metallic nanoparticles [39], coupled nanoparticles, metallic whiskers and nanostructured metallic surfaces [40]. This technique allows obtaining monochromatic cathodoluminescence images of structures with nanoscale resolution and study the optical response of different parts of the nanostructures to the excitation of the focused electron beam.

In the previous Section it has been demonstrated that a focused free-electron beam impacting on an unstructured metal surface can act as an efficient, broadband, nano-scale SPP source. This SPP generation technique has several advantages over traditional methods, such as high spatial localization (significantly below the diffraction limit of light), a high degree of source mobility, and the elimination of (typically large) coupling structures.

The technique of SPP source generation by an electron beam was used to develop a new "hyperspectral" imaging (HSI) technique for the visualization of plasmon excitations in metal nanostructures [41]. HSI utilizes high localization of the source to excite nanostructures and record optical response from every point of excitation in a wide range of wavelengths thereby acquiring both spectral and spatial information. The main advantage of hyperspectral imaging with an electron beam is that it allows obtaining photonic and plasmonic maps in a wide range of wavelengths, plasmonic decay lengths and localized plasmonic spectral and spatial mode structures from a nanostructured sample in a single measurement.

HSI was realized in a experimental setup for probing the optical properties of nanostructures with an electron beam, described in the previous Chapter, with the improved efficiency of the light collection system due to the introduction of a wide-angle parabolic mirror. The concept of the hyperspectral imaging of plasmonic excitations on nanostructures with an electron beam and the experimental setup used to realize this technique, is detailed in the following Section.

4.3 The concept of hyperspectral imaging (HSI)

In this Section the underlying ideas behind the hyperspectral imaging technique, in comparison to conventional imaging, are presented. The HSI technique is illustrated for a grating manufactured on a metal film probed by an electron beam. Applications for the study of the plasmonic properties of nanostructures are discussed.

4.3.1 Conventional imaging versus HSI

A pixel in a conventional image obtained by a single-shot digital camera typically contains information on the intensities of three primary additive color channels: red, green, and blue. By mixing these colors in a proportion defined by the intensity of light emitted from a photographed object and detected by a CCD array in each channel, a two dimensional full color image is created (Fig. 4.1).

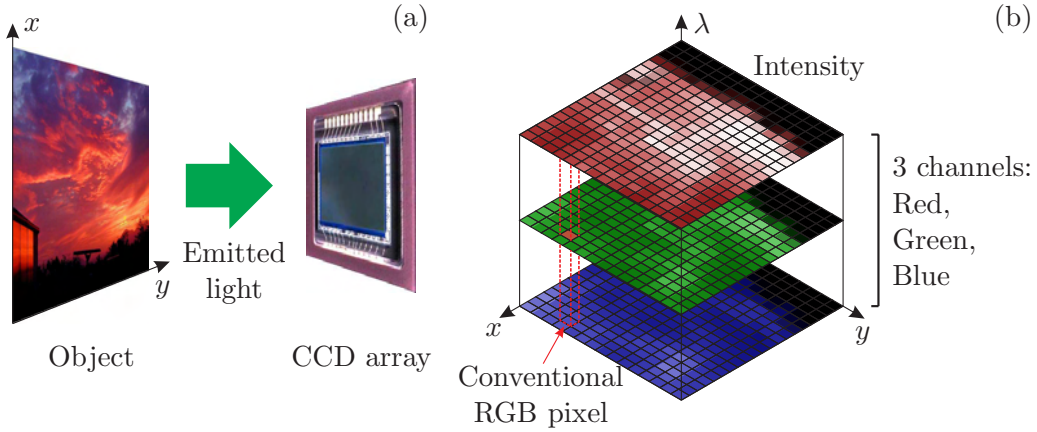

Figure 4.1: The concept of conventional imaging with a single shot digital camera. The image from an object is acquired by the CCD array of the camera by detecting the light emitted from the object (a). The data used for the formation of the output image consists of three channels: red, green and blue, each containing the image of the object in a narrow range of the wavelengths (b).

In a hyperspectral image each sampled pixel contains an entire spectrum of data — the intensities of hundreds if not thousands of individual wavelength channels. This concept is well known in airborne reconnaissance [42, 43] and surveillance [44], geological [45, 46], mineralogical [47, 48], and atmospheric research [49, 50].

In the realization of hyperspectral imaging of plasmonic excitations on nanostructures with an electron beam, the hyperspectral image is formed by scanning a structure with a focused electron beam and synchronously recording the light emission spectrum from the decoupling of the plasmons generated at every pixel (see Figure 4.2a). This decoupling can occur either through scattering at random surface imperfections or, as in the experiments described in this Chapter, via a nearby purposely engineered decoupling grating.

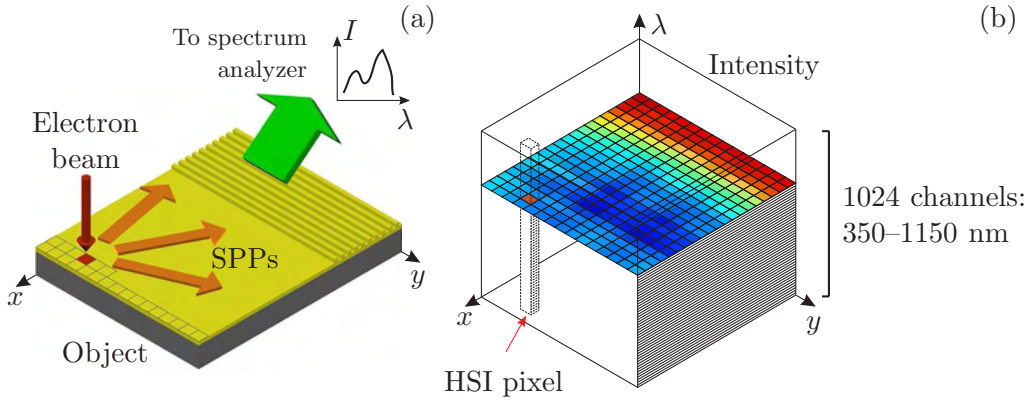

Figure 4.2: (a) The hyperspectral imaging concept illustrated for a grating on a gold film. At each electron beam injection point in the sample (x-y) plane, i.e. each image pixel, the entire emission spectrum from decoupled surface plasmons is sampled simultaneously at a number of discrete wavelengths λ_k. (b) The data cube generated can be mined to produce single-wavelength spatial intensity distributions of plasmonic emission (x-y planes), point spectra (vertical lines), and wavelength-specific linear emission intensity profiles (horizontal lines).

The HSI technique generates a three-dimensional "data cube," as illustrated in Figure 4.2(b), with two spatial axes, defining the co-ordinates of the electron beam injection points in the sample plane, and a spectral axis. The number of channels in the hyperspectral imaging data cube is defined by a

spectral resolution of the spectrum analyzer. This cube can be "mined" in a number of ways (see Figure 4.3) to obtain, for example, single-wavelength spatial intensity distributions of plasmonic emission, point spectra, and wavelength-specific linear emission intensity profiles (from which, under certain conditions, SPP decay lengths can be derived).

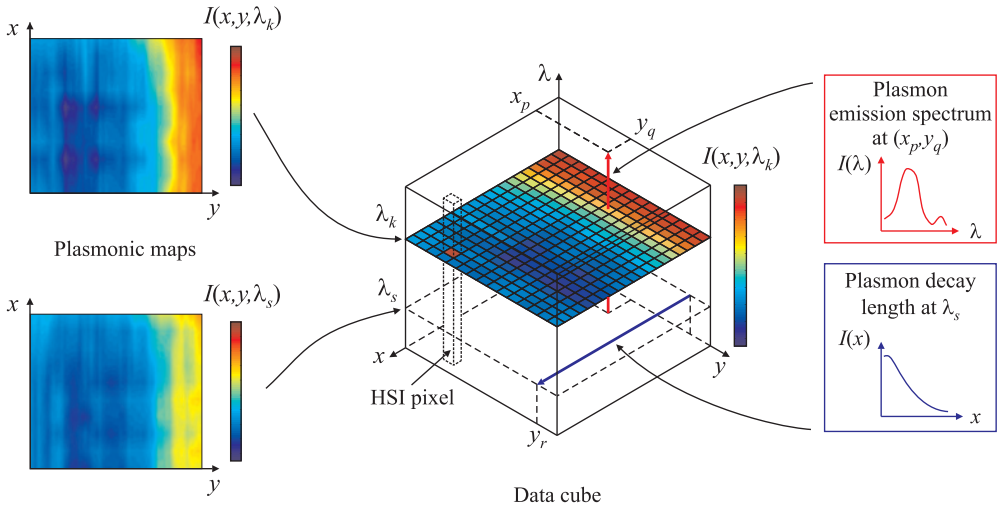

Figure 4.3: The hyperspectral imaging technique generates a three-dimensional "data cube" with two spatial axes, defining the co-ordinates of the electron beam injection points in the sample plane, and a spectral axis. This cube can be "mined" to obtain, for example, single-wavelength spatial intensity distributions of plasmonic emission (plasmonic maps), point spectra, and wavelength-specific linear emission intensity profiles (from which, under certain conditions, SPP decay lengths can be derived).

The plasmonic maps can be obtained by "slicing" the data cube the horizontal planes. The intensity in each plane gives the plasmonic response of the nanostructure to the electron beam excitation at wavelength λ_k. The spectral response of a particular point (x_p, y_p) of the sample is the linear distribution parallel to the vertical axis λ extracted from this point. Linear distributions of intensity in the plane perpendicular to axis λ can be used to determine the SPP decay length at the wavelength λ_s.

Therefore, the hyperspectral imaging technique for surface plasmon polaritons on metallic nanostructures allows collecting a substantial amount of information on plasmonic properties of the sample in a single measurement.

This technique can be used for simple visualization of light emission from decoupled plasmons, providing information on decay lengths and feature sizes with nanometer resolution. The requirements of the experimental setup for the realization of the HSI are outlined in the following Section.

4.3.2 Experimental requirements for HSI realization

At first glance, the concept of hyperspectral imaging of plasmonic nanostructures can be realized on any experimental setup, consisting of a scanning electron microscope equipped with a light collection system and a spectrum analyzer, similar to the one described in the previous Chapter. However, before going any further, the following considerations should be taken into account.

The imaging of the nanostructures requires the use of the electron beam of an appropriate size. The size of the electron beam (1 μm), that was used to demonstrate SPP generation, is only applicable for imaging microstructures and in order for the method be applicable to use in HSI, it should be significantly reduced. However, the reduction in size will reduce the current of the beam, and consequently, the amount of light emitted from the sample. Therefore, the efficiency of light collection should be increased accordingly.

The algorithm of data acquisition in HSI directs the electron beam to scan through the sample in an orderly fashion through a set of points, the positions of which are predefined. The repositioning of the electron beam should be synchronized with the acquisition of spectra. The manual implementation of the algorithm can hardly be efficient, especially for images with high spatial resolution. Therefore, the way that the electron beam induced light is collected and analyzed should be revised and automated.

A simple 10×10 points HSI scan will result in acquisition of 100 spectra, which should be composed into a data cube. This three dimensional array should then be "mined" to extract all the plasmonic maps, spectral and spatial distributions. Completion of all these tasks for every sample manually is a formidable task. However, HSI analysis can be automated with the

appropriate software. Therefore, a program for the collection of the acquired spectra into the data cube and subsequent "mining" must be developed.

The experimental technique fulfilling all these requirements and therefore capable of realizing the hyperspectral imaging of plasmonic properties of nanostructures with an electron beam, is described in the following Section.

4.4 SEM–CL system with improved light collection efficiency

The concept of hyperspectral imaging of plasmonic nanostructures has been realized on the experimental setup for probing the optical properties with an electron beam, described in Section 3.3, with the improved efficiency of the light collection system. To improve the efficiency of the light collection system, a new wide-angle parabolic mirror was introduced as an upgrade of the narrow-angle mirror. The possibility to interchange mirrors has been preserved.

4.4.1 Wide-angle parabolic mirror

One of the main disadvantages of the system, described in Section 3.3, from the point of view of the light collection efficiency, was the narrow-angle parabolic mirror. Although the narrow angle of light collection is useful in certain experimental situations, the efficiency of the light collection can be significantly improved by the use of a wide-angle parabolic mirror. Such mirror, with a focal distance of 1 mm, has been designed and incorporated into the light collection system as a substitute for the narrow-angle mirror.

In mathematics, a parabola can be defined as a locus of points in a plane which are equidistant from a given point (the focus) and a given line (the directrix). The focal distance of the vertical parabola, described by the general equation $4p(x - x_0) = (y - y_0)^2$, is located at a distance p along x axis from the vertex of the parabola (x_0, y_0).

The physical interpretation of this mathematical definition of the parabola is that all rays of light emitted from the focus reflect off the

parabola and travel parallel to each other. A close analogy between a parabolic mirror and a convex lens can be seen through this interpretation. Therefore, it is reasonable to redefine the term focal distance in this context.

The point where all rays which enter the convex lens parallel to its axis are brought to a focus is called the principal focus, or simply the focus. Due to the reversibility of light waves, if the point source is placed in the focus, part of the radiation directed towards the lens will be converted into a parallel beam. The distance between the lens and the focus is called the focal distance of the lens. Similarly, the focal distance of the parabolic mirror can be defined as a distance between the mirror and the focus. This re-definition is only vital for the wide-angle parabolic mirror, as for the narrow-angle geometry the mathematical and physical focal distances coincide.

The selected parabolic curve for the mirror was part of an $x(y) = y^2/12$ parabola in the range of $y = 1$–10 mm, defined in a conventional Cartesian system of coordinates. For this parabola, depicted in Figure 4.4a, $x_0 = y_0 = 0$ and the mathematical focus of the parabola has coordinates $(3, 0)$. The focal distance for this parabolic mirror, following the physical interpretation, is 1 mm. The selection of the cutoff coordinates along the y axis defines the focal distance and the solid angle in which the light is collected by the mirror.

A three dimensional prototype of the wide angle parabolic mirror based on the calculated curve was developed using AutoCAD Inventor computer-aided design (CAD) software[1]. The prototype was then processed by Path-trace EdgeCAM computer aided manufacturing (CAM) software and turned using a Computer Numerically Controlled (CNC) Multi Function Bridgeport ITL400 Lathe from aluminium. A picture of the wide-angle parabolic mirror is presented in Figure 4.4b.

The light collection part of the mirror is a part of a three dimensional paraboloid obtained by a 180° rotation of the selected part of the $x = y^2/12$ parabola around the line $y = 0$. As this geometry completely isolates the sample from the electron beam, a cylindrical hole of 2 mm in diameter aligned

[1]The final design and the manufacturing of the wide-angle mirror was done by Mr. P. Connell, Mechanical workshop, School of Physics and Astronomy, University of Southampton, Southampton, UK

with the focal point was drilled in the top part of the mirror (Fig. 4.4b). The dimensions of the light collecting part of the mirror are 18×9 mm and the focus of the mirror is located 1 mm under the mirror and 7 mm from the open edge. As shown in Figure 4.5a, the collection of light by a wide-angle mirror is significantly better, although less angle-resolved, than by the narrow-angle mirror (Fig. 3.5a).

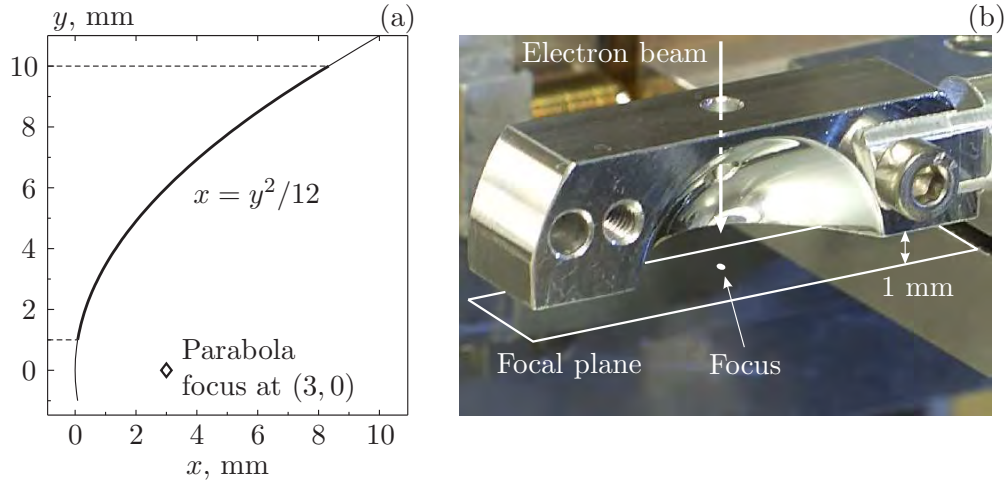

Figure 4.4: Wide-angle parabolic mirror. The selected parabolic curve for the mirror was part of an $x(y) = y^2/12$ parabola in the range of $y = 1 \ldots 10$ mm (a). The electron beam illuminates the sample, located in the focal plain of the mirror, through a 2 mm hole in the top part of the mirror (b).

The alignment of the focal point of the parabolic mirror with the light emitting part of the sample, as mentioned before, is paramount for the performance of the whole light collection system. The mirror was mounted on a manually controlled two dimensional xy-stage allowing fine positioning of the mirror in the plane of the sample (Fig. 4.5b). The xy-stage was attached to the motorized linear stage, remotely operated from outside the SEM, that controlled the distance between the mirror and the sample in the direction perpendicular to the plane of the sample (along z-axis)[2]. The optimal position of the mirror (full alignment of the focus and the emitting

[2]The stage allowing mirror repositioning in three dimensions was designed and manufactured by Mr. A. Denisyuk, Optoelectronic Research Centre, Southampton, UK

region of the sample) is achieved by maximizing the optical signal from the sample.

The xy-stage with the wide-angle parabolic mirror can be easily removed from the supporting linear motorized stage and the narrow-angle mirror can be installed in its place (Fig. 3.5). This was done to preserve functionality of the original setup and exploit superior angle resolution of the narrow-angle mirror when required by experimental conditions.

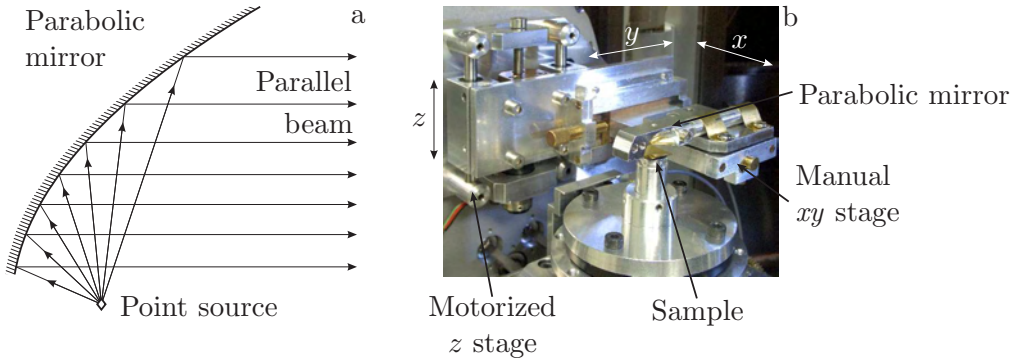

Figure 4.5: Operation of the parabolic mirror (a): light emitted by a point source located in the focus of the parabolic mirror is reflected as a parallel beam. The picture of the parabolic mirror used in the experimental setup to probe the optical properties of nanostructures with an electron beam (b). The sample is located 1 mm below the mirror, and the alignment of the focus of the mirror with the part of the sample excited by the electron beam is provided by a two dimensional manually controlled xy-stage mounted on a remotely controlled linear stage (z axis).

The calibration of the light collection system with the wide-angle parabolic mirror was performed using the same technique as for the narrow-angle mirror, described in Section 3.3. Only the part of the light collection system before the spectrum analyzer, consisting of the wide-angle parabolical mirror, transparent window in the SEM chamber and a set of lenses, needed recalibration as the spectral efficiency of the spectrum analyzer has already been measured (corresponding spectra of the Ocean Optics LS-1 tungsten halogen broadband white light source spectrum measured by direct illumination of the monochromator slits and the spectral efficiency of the source provided by the manufacturer of the source are presented in Figure 4.6a).

The spectral efficiency of the wide-angle mirror, window and the lenses was measured as a ratio between the spectrum of the light collected from the end of the fibre, illuminated by the LS-1, by the system and the spectrum of the fibre illuminating the slits of the monochromator directly (corresponding spectra are presented in Figure 4.6b). The *spectrum calibration* curve for the whole light collection is a product of a spectral efficiency of the monochromator–spectrometer and the mirror–window–lenses parts (Fig. 4.6c). By dividing every measured spectrum by the obtained spectral efficiency of the light collection system it was possible to acquire undisturbed results.

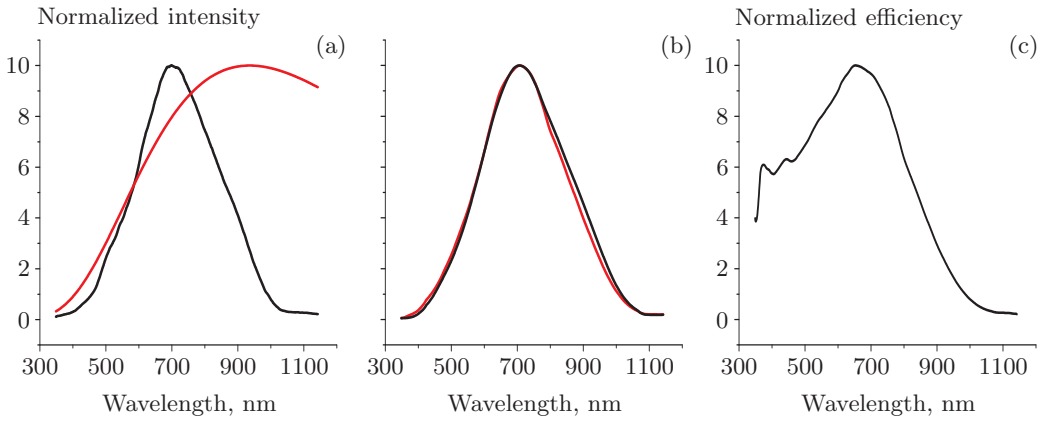

Figure 4.6: Calibration of the light collection system with a broadband light source and optical fibre. Spectra of the source measured by direct illumination of the monochromator slits (black curve, a) and provided by the manufacturer (red curve, a), giving the spectral efficiency of the monochromator and spectrometer. Spectra of the light collected from the end of the fibre by the light collection system (black curve, b) and of the fibre illuminating the slits of the monochromator directly (red curve, b), giving the spectral efficiency of the wide-angle mirror, window and the lenses. Calibration curve of the light collection system (c).

The improvement in the efficiency of the light collection system due to the wide-angle mirror was estimated by measuring the energy of the light emitted from a phosphor screen, as a result of electron beam excitation, by each mirror. The same number of counts over the whole spectral range 350–1150 nm was registered by the system with the wide-angle mirror at acquisition times roughly 1/100 shorter compared to the case when the light

was collected by the narrow-angle mirror. Therefore, due to shorter focus distance, significantly larger solid angle of light collection and better focusing, the implementation of the wide-angle mirror improved the efficiency of the whole system by up to two orders of magnitude to the value of 10^{-3} (see Section 3.3).

The interchange of a narrow-angle parabolic by a more efficient wide-angle one has not changed the principle of the operation of the experimental setup. The beam of electrons of the selected energy and current is generated at the top of the SEM column and directed by a system of magnetic lenses downwards into the chamber to the sample through the hole in the top part of the mirror (Fig. 4.4). The light resulting from the bombardment of the sample with electrons is collected and analyzed by the light collection system: the wide-angle parabolic mirror directs the light through the transparent window in the SEM chamber to the system of lenses, focusing it on the slits of the spectrum analyzer. Due to poor signal–noise ratio in the infrared region for the samples used in this Chapter, the measurements were performed in the 350–950 nm spectral region.

Two modes of SEM operation can still be used for the experiments: the *scanning mode* and the *spot mode*. In the scanning mode the position of the beam is performed in an automatic regime controlled by the SEM software. The beam is raster scanned inside the rectangular area of sample with the selected resolution and frequency. The acquisition of the spectrum of light, induced by the electron beam on the sample, is not synchronized with the repositioning of the beam. In the spot mode the electron beam is stationary and focused into a spot on the sample. The repositioning of the beam can be done manually using the secondary electron image of the sample taken before entering the mode as a reference. The acquisition of spectra can also be performed manually after each repositioning.

Neither of these modes can be used for the realization of the HSI. In order to perform hyperspectral imaging with an electron beam, a special mode, in which the microscope and the spectrum analyzer are remotely controlled, has to be developed.

4.4.2 Acquisition, processing and analysis of the hyperspectral image

The hyperspectral imaging technique, described in the previous Section, requires focusing of the electron beam to the predefined points on the sample with acquisition of the spectrum induced by the electron beam at each point — functionality provided by neither the SEM, nor by the spectrum analyzer software. In order to implement HSI on the existing experimental setup, both the electron microscope and the spectrum analyzer had to be controlled remotely and the required tasks, electron beam repositioning, synchronized spectra acquisition and storage, had to be performed centrally. For that purpose special software, denoted hereinafter as the HSI program, has been developed[3].

The HSI program, controlling both the SEM and the spectrum analyzer, that allows collection of spectral information according to the hyperspectral imaging technique, has been realized in the National Instruments Labview environment. Both the microscope and the spectrum analyzer support TCP connection and contain sets of commands providing the functionality of the hardware, controlled remotely, to the same extent as the original software.

The Labview environment is specialized software for data acquisition from various instruments, its analysis, processing and presentation. The software uses an original graphical dataflow language and a block diagram interface for the development of programs. The user interface controls are mapped to the block diagram "code" allowing control over the data acquisition and processing.

The interface of the HSI program allows interactive control and monitoring of all vital properties of the spectrum analyzer, such as exposure time, acquired spectrum, temperature of the CCD array, etc., properties of the SEM, such as acceleration voltage, mode of operation (scanning or spot mode), electron beam current, and properties of the hyperspectral image acquisition. Apart from instrumental properties (parameters of the electron

[3]The HSI program was developed in collaboration with Dr. F. Jonsson during his stay in the University of Southampton, UK

beam and exposure time of the spectrum analyzer), HSI acquisition has only one parameter: the resolution of the image, i. e. number of points along the horizontal and vertical axes.

The main limitation to the spatial resolution of the HSI image is the time limit imposed by the stability of the electron beam and position of the sample. As sensitive spectral measurements are performed on a nanoscale, the consistency of the image can be easily compromised during the process of acquisition. In practise, the acquisition time was kept under 60 minutes, allowing 60×60 point HSI images with dwell time 1 sec at each point. Most of the images were taken at resolution 21×17 or 41×33 points with dwell times 1–5 seconds. The best achieved resolution is 81×65 points HSI image of a grating with exposure time 0.5 sec per point. The ratio between the number of points in the HSI image along the horizontal and vertical axes corresponds to the 5:4 ratio of secondary electron images acquired by the scanning electron microscope.

The lower limit of the exposure time at every point of the image during HSI acquisition is defined by the contrast in the optical signal obtained from distinctive features of the sample. This can be denoted as "signal-to-signal" ratio as opposed to the commonly used "signal-to-noise" ratio. For example, in the case of a grating on a gold film the difference in the amount of counts at the maximum of spectra emission by the grating (the first "signal") and the film (the second "signal") should be no less than 50, otherwise the consistency of the image is compromised due to instrumental noise and variation of the signal from point to point. The upper limit of the dwell time is defined by the spatial resolution of the HSI image and the stability time of the electron beam and the position of the sample, as discussed above.

The process of image acquisition with the HSI program is the following. Upon starting the program, the connection to the SEM and the spectrum analyzer is established and current operating parameters of both instruments are acquired. The alignment of the sample for the imaging and parameters of the electron beam are set using the original SEM software. The spatial resolution of the HSI image and the exposure time is set using the HSI

program. The SEM is switched onto spot mode and of the hyperspectral image is acquired according to the algorithm.

The acquisition of the HSI image is performed by an automatic regime by continuous focusing of the beam into the spot on the sample, defined by the set spatial resolution, and synchronized acquisition of the induced spectra by the spectrum analyzer. The process of hyperspectral imaging is illustrated in Figure 4.7 for the case of a 4×3 HSI image of the grating on the metal film.

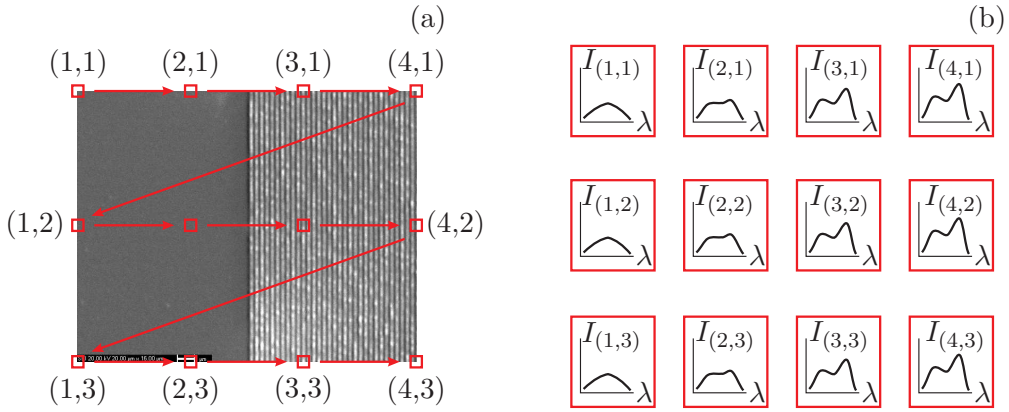

Figure 4.7: Acquisition of the hyperspectral image by the HSI program illustrated on a 4×3 image of the grating on a gold film. The grating grooves occupy the right half of the image, the left half corresponds to the gold film. The predefined positions of the electron beam are denoted by red squares. The acquisition starts in the top left corner and ends in the bottom right corner (a). The acquisition results in 12 spectra of electron beam induced emission, each corresponding to the certain point of the sample (b).

The beam is positioned in the top left corner of the image at the point with coordinates $(1, 1)$. After the acquisition of the spectrum of this point, the beam is repositioned to point $(2, 1)$ along the horizontal axis, and the next spectrum is acquired. The process is repeated until the right edge of the imaged area is reached. After that the electron beam is positioned at point $(1, 2)$ to start the acquisition of the spectral information along the horizontal line separated by the size of the vertical step from the first point. The scanning is completed when the bottom right point of the sampled area $(4, 4)$ is reached (Fig. 4.7a).

The result of the measurement is 12 spectra of electron beam induced emission, each corresponding to a certain point of the sample (Fig. 4.7b). After the acquisition of the image, all spectra and parameters of the experiment (electron beam acceleration voltage and current, magnification and working distance of SEM, dwell time and spatial resolution) are stored in a text file ready for further processing and analysis.

In order to eliminate spatial distortion of the image caused by inhomogeneous light collection by the parabolic mirror, another HSI image with the same parameters should taken on a part of the sample, that can be considered as a background. In case of the grating on a gold film, depicted in Figure 4.7, the background HSI image is taken from the gold film away from the grating. For the discussed case of the grating, the subtraction of these two images will result in a spatially resolved spectral data related to plasmonic properties of the grating. Similar normalization of the detected spectra has been performed in a "one dimension HSI," conducted manually in the experiments on generation of SPP source by an electron beam in spot mode to identify the part of the emission related to the decoupling of plasmons as a difference between the electron beam-induced emission spectrum and the spectrum of an unstructured gold film (Section 3.6).

The acquired spectral data is not suitable for analysis without rigorous processing, for the following reasons. Any spectrum measured by the spectrum analyzer might contain random high intensity narrow peaks, the result of CCD array excitation by cosmic rays. These peaks have to be eliminated automatically to allow further processing (in the previous spectral measurements this task was performed manually). After that the spectra should be smoothed, to reduce instrumental noise, and assembled into a three dimensional array, denoted earlier as the "data cube."

The same manipulations have to be performed with the background HSI image in order to obtain the data cube corresponding to the background signal. Only the final data cube, obtained by subtraction of a background image from the image of the sample, can further be analyzed to obtain the information on plasmonic properties of the sample: plasmon emission maps, linear and point distributions of electron beam induced SPP intensity, etc.

The processing and analysis of the HSI experimental data was performed by a program realized in the Mathworks Matlab environment. The developed program automatically processes the acquired HSI image (cosmic rays peaks removal, smoothing and background subtraction) and analyzes the data cube. Output results of the analysis can be presented in one of the following forms. Two dimensional distributions of plasmonic emission can be presented as intensity images at certain wavelengths, or composed into a video, containing these intensity distributions for all available wavelengths. The visualization and analysis of the obtained linear spectral and spatial intensity distributions, such as estimates of surface plasmon polariton decay lengths, is performed using Matlab built-in graphical functions and data curve fitting algorithms.

To summarize, the efficiency of the light collection system of the experimental setup for probing the optical properties of nanostructures with an electron beam has been significantly improved with the introduction of a wide-angle collection mirror. The functionality of the setup with a narrow-angle mirror has been preserved. The software, allowing hyperspectral image acquisition, processing and analysis has been developed. The analysis of the experimental data consists of the composition of the HSI data cube, extraction of plasmonic or photonic maps, spectral point and spacial linear distributions.

4.5 HSI of gold gratings

The spectra obtained by HSI are determined primarily by the material properties and nanoscale topography of the nanostructure under investigation and the geometry of the light-collection system. To illustrate this, experiments were performed on gold grating samples using wide- and narrow-angle parabolic light-collection mirrors to direct decoupled light out of the SEM chamber, via a fused silica window, to a spectrometer (Fig. 4.8).

Gratings facilitate SPP decoupling to light by compensating for the mismatch between their wave vectors with an integer multiple of the grating vector $k_{\mathrm{G}} = 2\pi/a$, where a is the grating period (see Section 3.4.2).

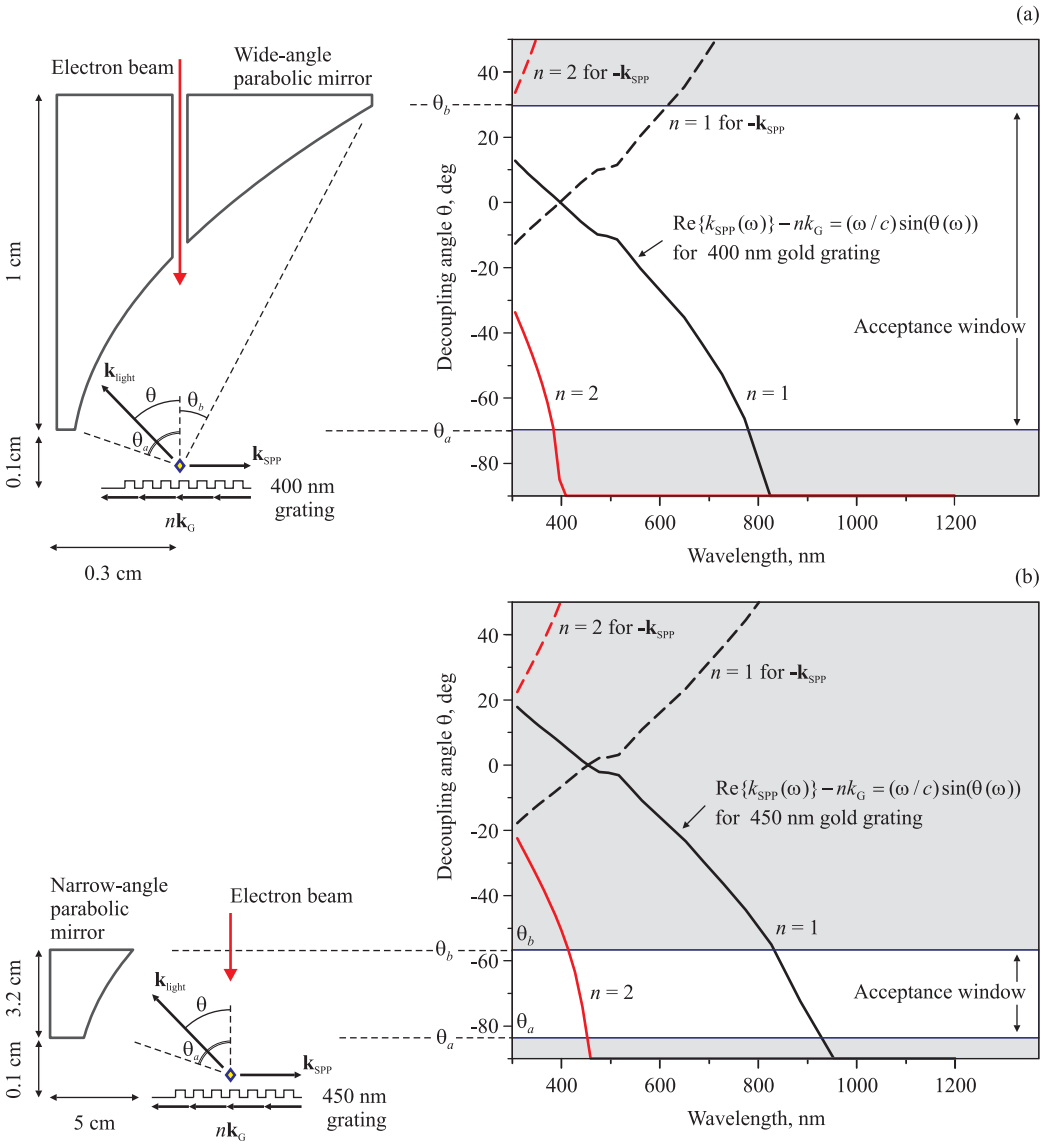

Figure 4.8: Hyperspectral imaging light-collection geometries and angular decoupling diagrams for the gratings imaged in each configuration. (a) The wide-angle light-collection geometry with its acceptance window, $-70° < \theta < 30°$, mapped onto the 400 nm period grating's decoupling diagram. (b) The narrow-angle collection geometry with its acceptance window, $-82° < \theta < -67°$, mapped onto the 450 nm period grating's decoupling diagram. (Note that the two mirrors are drawn to different scales to achieve the correct schematic mapping of their acceptance windows onto the decoupling diagrams).

The wavelength dependence of the decoupling angle θ is described by the equation:

$$\mathrm{Re}\{k_{\mathrm{SPP}}(\omega)\} - nk_{\mathrm{G}} = (\omega/c)\sin(\theta(\omega)), \tag{4.1}$$

where n is a positive integer and $k_{\mathrm{SPP}}(\omega)$ is the SPP wave vector, which at a metal/vacuum interface depends on the complex permittivity $\varepsilon(\omega)$ of the metal according to the equation:

$$\mathrm{Re}\{k_{\mathrm{SPP}}(\omega)\} = \frac{\omega}{c}\mathrm{Re}\left[\left(\frac{\varepsilon(\omega)}{1+\varepsilon(\omega)}\right)^{1/2}\right].$$

Only wavelengths decoupled at angles within the light-collection system's "acceptance window" (defined by the mirror's dimensions and its position relative to the sample) can be detected by the spectrometer. For the purposes of the present demonstrations, a comparatively small wide-angle mirror located just 1 mm above the sample provided an acceptance window extending from $\theta_a = -70°$ to $\theta_b = 30°$ (Fig. 4.8(a)), while a larger narrow-angle mirror located ~ 5 cm to one side of the sample provided a window between $\theta_a = -82°$ and $\theta_b = -67°$ (Fig. 4.8(b)).

The samples studied were 400 and 450 nm period gratings, each comprising thirty lines with a height of 50 nm (Fig.'s 4.9(a) and 4.10(a)), prepared by electron beam lithography on 200 nm thick evaporated gold films on silicon (a sufficient film thickness to exclude any influence from SPP's excited on the metal/substrate interface). The wide-angle mirror was employed to image the 400 nm grating sample and the narrow-angle mirror to image the 450 nm sample. Mapping the mirrors' angular acceptance windows onto the gratings' decoupling diagrams (plots of decoupling angle vs. wavelength, calculated using optical constants for gold from [51]) as shown in Figure 4.8, illustrates the effect that light-collection geometry has on recorded spectra: both gratings generate first- ($n = 1$) and second-order ($n = 2$) decoupled light within the wavelength range of the spectrometer. With the narrow-angle mirror the two orders are expected to generate separate narrow signal peaks at different wavelengths, but with the wide-angle mirror there can be no such separation because the spectral range of the first-order extends to the lower limit of the detection range (completely overlapping the second

order). However, at the expense of angular resolution, the wide-angle mirror offers a smaller minimum working distance for the SEM (enabling higher resolution imaging), and is found in practice to provide a light-collection efficiency up to two orders of magnitude higher than the narrow-angle mirror (allowing for shorter imaging times and the use of lower beam currents). When the electron beam injection point lies within a grating (rather than to one side of it), both the positive and negative directions of k_{SPP} must be considered. In the narrow-angle configuration, the acceptance window is such that light decoupled from plasmons with negative k_{SPP} values (dashed decoupling curves in Figure 4.8) cannot be detected. However, in the wide-angle configuration, first-order decoupling from SPP's with negative k_{SPP} values contributes to the detected signal at wavelengths up to ~ 620 nm.

Hyperspectral imaging was performed on rectangular sample areas encompassing, in each case, the grating and an adjacent area of unstructured gold surface (Fig.'s 4.9(a) and 4.10(a)), using a 40 kV electron beam with a spot size of ~ 75 nm. In the wide-angle configuration the pixel size (distance between adjacent electron beam injection points) was 0.6 μm, and the dwell time per pixel was 2 s. In the narrow-angle configuration, injection point spacings of 0.5 μm in the x-direction and 2.4 μm in the y-direction were used (larger in the y-direction because all sample cross-sections parallel to x are the same), with a dwell time of 5 s. By subtracting background emission spectra for areas of unstructured gold (far outside those shown in Figures 4.9(a) and 4.10(a)) from the HSI spectra, normalized spectra relating only to emission from SPP decoupling at the gratings were obtained [52]. This normalization aims to eliminate luminescence (from the recombination of d-band holes created by the electronic excitation), dipole radiation (from the coming together of incident electrons and their mirror images in the sample), light decoupled from SPP's by scattering at random surface imperfections, and fluorescence from any residual contaminants on the sample.

By "slicing" the normalized hyperspectral data cube at a fixed wavelength (such as λ_k in Figure 4.2(b)), one obtains the spatial intensity distribution of light decoupled from SPP's at that wavelength, as a function of the electron beam injection coordinate. Sequences of such images reveal the evolution

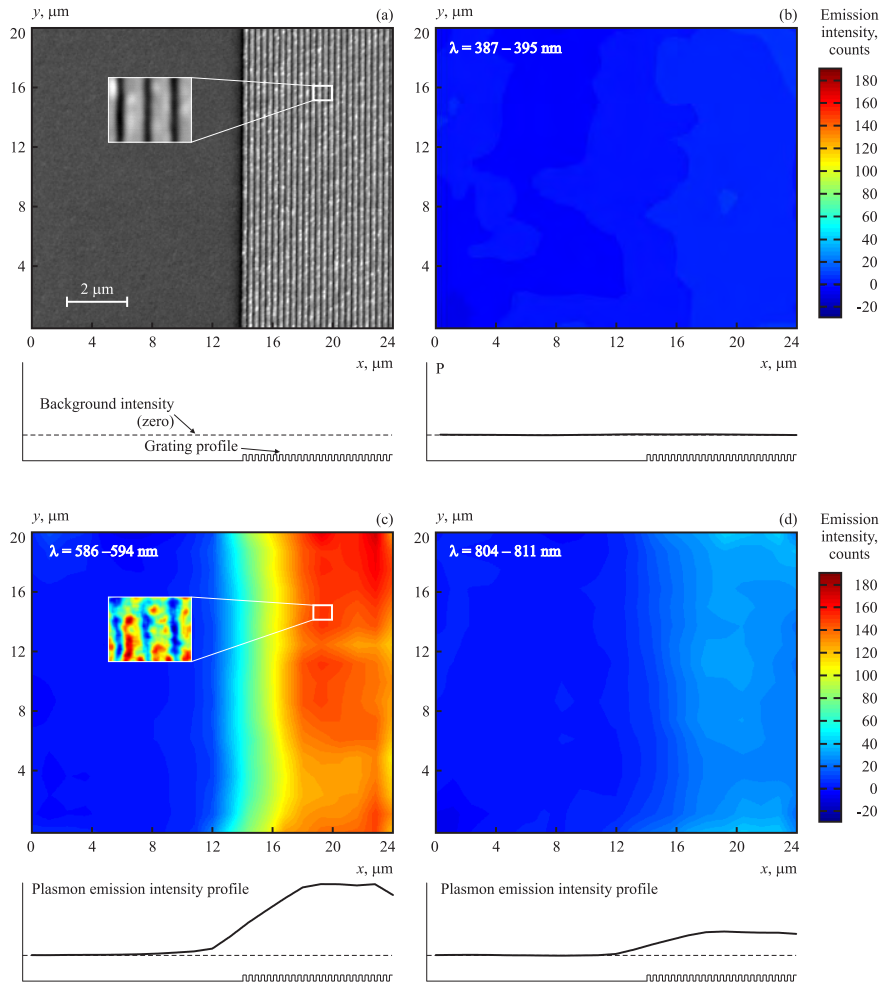

Figure 4.9: Hyperspectral imaging of the 400 nm gold grating sample with the wide-angle parabolic light-collection mirror. (a) Secondary electron image of the sample area, encompassing grating and adjacent unstructured gold film, which was imaged in hyperspectral mode. (b, c and d) Spatial plasmonic emission intensity distributions obtained by slicing the hyperspectral data cube in the x-y plane (averaged over 7 nm wavelength intervals), with corresponding average emission intensity profiles along the x direction: (b) 387–395 nm, where emission is negligible; (c) 586–594 nm, where the grating is resonant and efficiently decouples plasmons to optical radiation; (d) 804–811 nm, where the grating is weakly resonant and plasmon decoupling efficiency is relatively poor. The inset to (a) shows a high-resolution image of a small part of the grating. The inset to (c) shows the corresponding emission intensity distribution at 586–594 nm, wherein the grating structure is resolved.

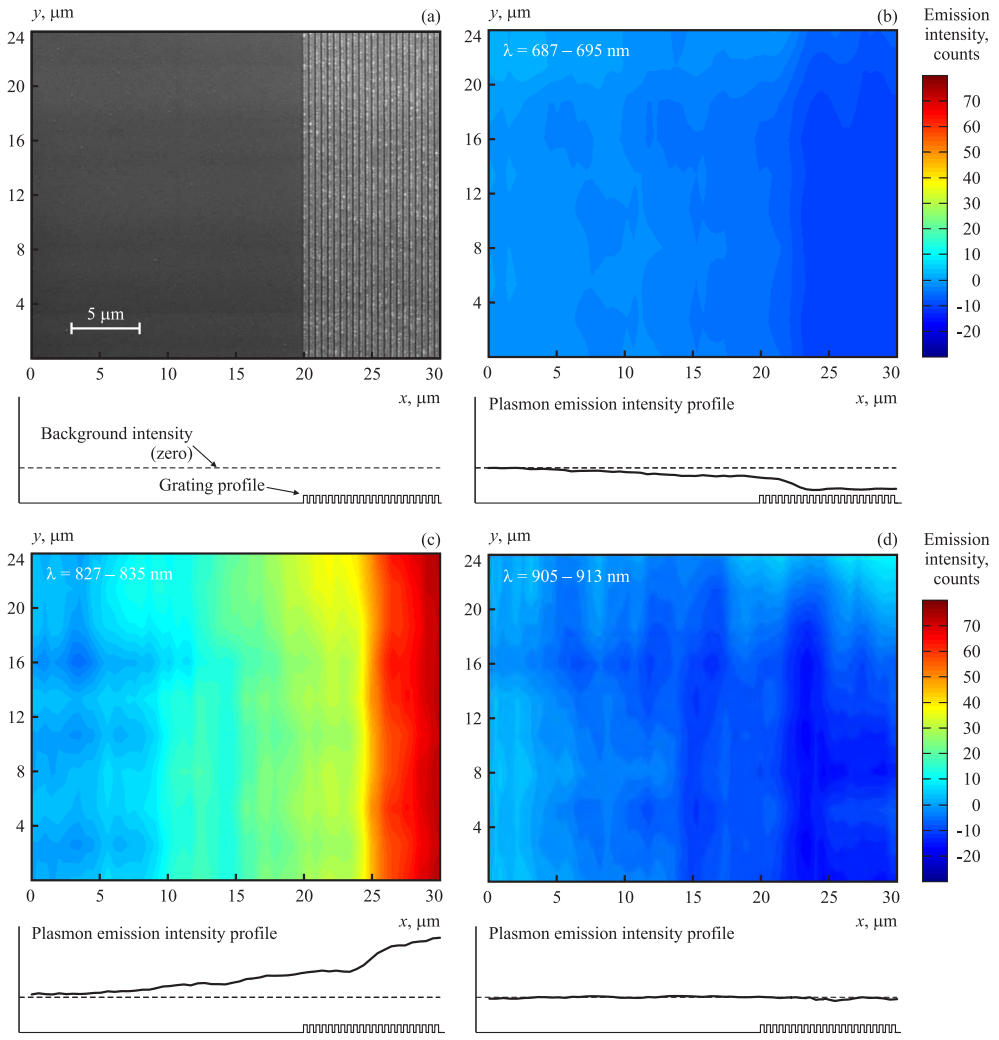

Figure 4.10: Hyperspectral imaging of the 450 nm gold grating sample with the narrow-angle parabolic light-collection mirror. (a) Secondary electron image of the sample area, encompassing grating and adjacent unstructured gold film, which was imaged in hyperspectral mode. (b, c and d) Spatial plasmonic emission intensity distributions obtained by slicing the hyperspectral data cube in the x-y plane (averaged over 7 nm wavelength intervals), with corresponding average emission intensity profiles along the x direction: (b) 687–695 nm, where the grating inhibits background emission at angles within the mirror's acceptance window; (c) 827–835 nm, where the grating is resonant and efficiently decouples plasmons to optical radiation; (d) 905–913 nm, where emission is negligible.

of plasmon emission over the sampled area as a function of wavelength, as illustrated in Figures 4.9(b–d) and 4.10(b–d) (where distributions are averaged over 7 nm wavelength intervals to reduce noise): for both gratings there are ranges, exemplified by distributions at 387–395 nm for 400 nm grating (Fig. 4.10(b)) and at 905–913 nm for 450 nm grating (Fig. 4.9(d), where there is little or no emission, indicating either that SPP's are not generated in this range or that they do not interact with the grating; Both also have highly resonant ranges, illustrated at 586–594 nm for the 400 nm grating (Fig. 4.9(c)) and 827–835 nm for the 450 nm grating (Fig. 4.10(c)), where the gratings efficiently decouple SPP's to optical radiation. For the 450 nm grating there is a range, exemplified by the distribution at 687–695 nm in Figure 4.10(b), where the *recorded* signal falls below the background level, indicating that the grating inhibits background emission (most likely from SPP scattering) at angles within the narrow-angle mirror's acceptance window. The inset to Figure 4.9(c) demonstrates the higher resolution capability of the wide-angle collection geometry: in this image (obtained with a 30×30 nm pixel size and 0.5 s dwell time) the individual grating lines can be identified in the emission pattern.

The HSI data cube can also be mined for information on decoupled light spectra and SPP decay lengths. By plotting intensity data along a line of fixed spatial coordinate in the cube, such as the vertical line at (x_p, y_q) in Figure 4.2(b), one obtains the decoupling emission spectrum (convoluted with the acceptance window of the light-collection geometry) for electron beam injection (SPP generation) at that point. By plotting intensity data along a line within a fixed-wavelength x-y plane, such as the horizontal line at (y_r, λ_s) in Figure 4.2(b), one obtains a linear emission intensity profile. If the line selected is perpendicular to the edge of a decoupling structure on the sample surface, then the SPP decay length at λ_s can be derived from an exponential fit to the intensity profile. Figure 4.11 illustrates such analyses for the present cases.

Figures 4.11(a) and (b) show spectra for single-pixel points within the 400 and 450 nm gratings respectively. Figure 4.11(a) shows a single broad emission peak for the 400 nm grating, centered at $\sim$ 600 nm. This may

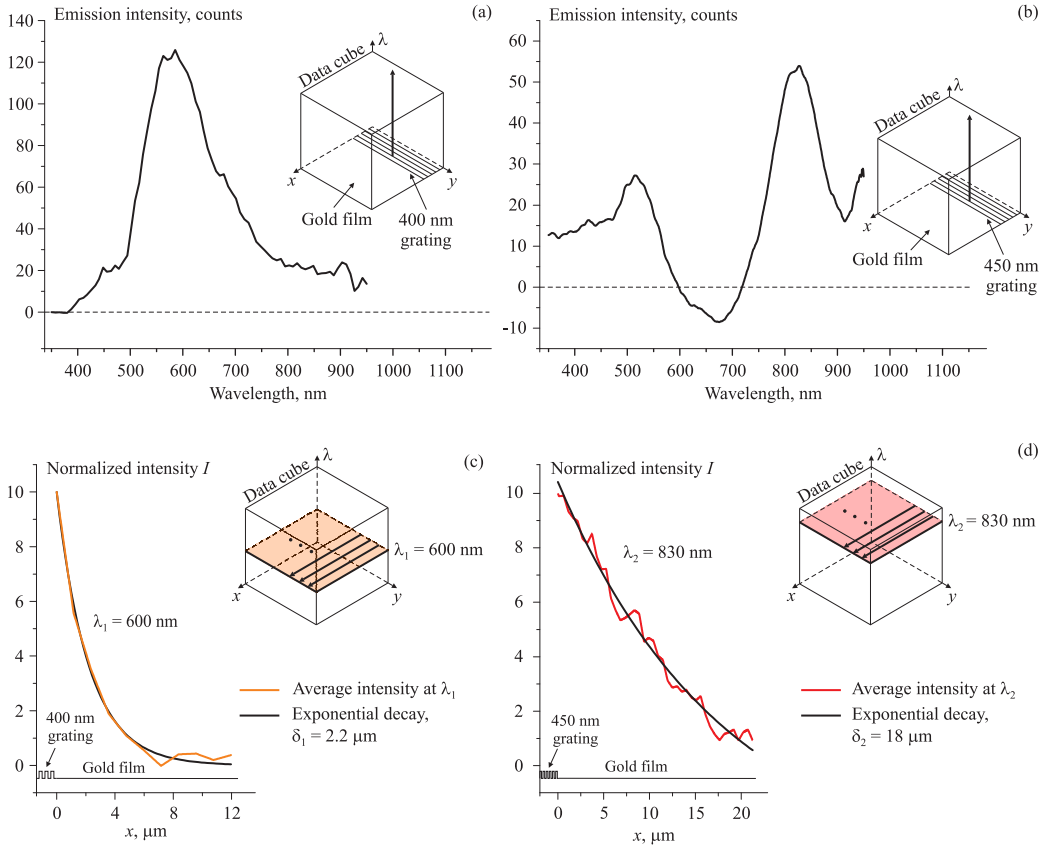

Figure 4.11: Single point spectra and surface plasmon decay lengths extracted from the hyperspectral imaging data cubes. Single-pixel spectra for points within: (a) the 400 nm period grating, recorded with the wide-angle light-collection geometry; (b) the 450 nm grating, recorded with the narrow-angle geometry. Linear emission intensity profiles along the x-direction (perpendicular to the grating lines), averaged over all values of y, for: (c) the 400 nm grating sample at $\lambda_1 = 600$ nm; (d) the 450 nm grating sample at $\lambda_2 = 830$ nm. Distances along x are measured relative to the edge of the gratings. Plasmon decay lengths δ are determined from exponential fittings to the data. The bold arrows in each figure's inset show the line(s) along which data is extracted from the cube to obtain the corresponding curve.

appear inconsistent with Figure 4.8(a), which indicates that the wide-angle light-collection geometry is capable of detecting first-order ($n = 1$) SPP decoupling at wavelengths down to the 350 nm lower limit of the spectrometer. However, mappings such as those shown in Figure 4.8 must be interpreted with care, in particular because Equation (4.1) says nothing

about the *efficiency* of SPP decoupling and scattering processes, which are complex wavelength-dependent functions of grating period, line-width and line-height that can only be analyzed numerically [53]. Neither does it take into account the spectrum of the electron beam SPP source, or the plasmon waves' decay lengths $\delta = [2\mathrm{Im}\{k_{\mathrm{SPP}}(\omega)\}]^{-1}$. Indeed for wavelengths shorter than ~ 510 nm, the SPP decay length is shorter than the period of either grating used in the present study, so grating-mediated decoupling is not possible.

In accordance with Figure 4.8, the narrow-angle geometry records a narrow peak in the near infra-red range, corresponding to the first ($n = 1$) decoupling order (Fig. 4.11b). For the reasons of poor short-wavelength decoupling efficiency described above, the predicted second-order ($n = 2$) peak at ~ 420 nm is not observed, however a peak centered at ~ 510 nm is recorded. This emission is most likely to result from the scattering of SPPs to light by the lines of the grating. As noted above, the scattering efficiency is a complex function of wavelength and grating geometry, however in general, while it may be as low as a few percent, it increases significantly as line-width deviates from $a/2$ (they are nearer $3a/4$ in the present cases) and as grating height exceeds $\sim 0.07\,\lambda$ (i.e. as wavelength decreases below ~ 710 nm in the present cases) [53]. As noted above (see Figure 4.10(b)), there is a wavelength range, shown in Figure 4.11(b) to be centered at $\sim$ 675 nm, over which the 450 nm grating inhibits background SPP scattering emission within the narrow-angle mirror's acceptance window.

Figures 4.11(c) and 4.11(d) show linear emission intensity profiles along the x-direction (perpendicular to the grating lines), averaged over all values of y, for the 400 nm grating sample at $\lambda_1 = 600$ nm, and for the 450 nm sample at $\lambda_2 = 830$ nm. SPP decay lengths of $\delta_1 = 2.2$ μm (at 600 nm), and $\delta_2 = 18$ μm (at 830 nm) are obtained from exponential fittings to this data. These may be compared with theoretical values of $\delta_{600} = 4.3$ μm, and $\delta_{830} = 53$ μm (where subscripts denote wavelength), calculated for an ideal gold/vacuum interface using optical constants for gold from [51]. The experimental lengths are shorter primarily because of losses due to scattering at random surface imperfections on the real gold film.

To summarize, the decoupling of surface plasmon polaritons by two diffraction gratings have been studied with the hyperspectral imaging with an electron beam in two configurations of the light collection system: using wide-angle and narrow-angle parabolic mirrors. Plasmonic maps of the gratings, decoupling spectra and spatial intensity of decoupled SPP has been acquired, plasmon decay lengths have been derived.

The ultimate resolution of the plasmonic maps obtained from hyperspectral imaging data cube largely depends on the size of the SPP source generated by an electron beam. The estimation of the surface plasmon source size can be performed by the HSI technique, as shown in the following Section.

4.6 Localization of the SPP source measured by the HSI of the diffraction grating

The localization of the SPP source, as discussed in Section 3.7, is limited by three fundamental factors: scattering of primary electrons in the skin depth layer of the metal, delocalization of the electrons due to Coulomb interaction with the electrons of the material, and broadening due to the finite electron speed in the skin layer of the metal. In this Section it is shown that the localization of the SPP source, generated by an electron beam on a metal surface, can be estimated using plasmonic maps acquired in a HSI experiment on a grating.

In order to estimate the size of the SPP source generated by an electron beam, the hyperspectral 21×17 pixel image of several periods of the 400 nm grating was taken with a 40 keV electron beam. The problem of SPP distribution on the scale of one period of the diffraction grating is very interesting on it own. However, the obtained results will only be analyzed from the point of view of the resolution of the HSI and localization (size) of the SPP source, generated by an electron beam.

The process of SPP source estimation is illustrated in Figure 4.12. The secondary electron image of the studied area of the grating is presented in Figure 4.12a. Besides illustration purposes, this image was used to obtain

the size of the electron beam, according to the procedure described in Section 3.3.4.

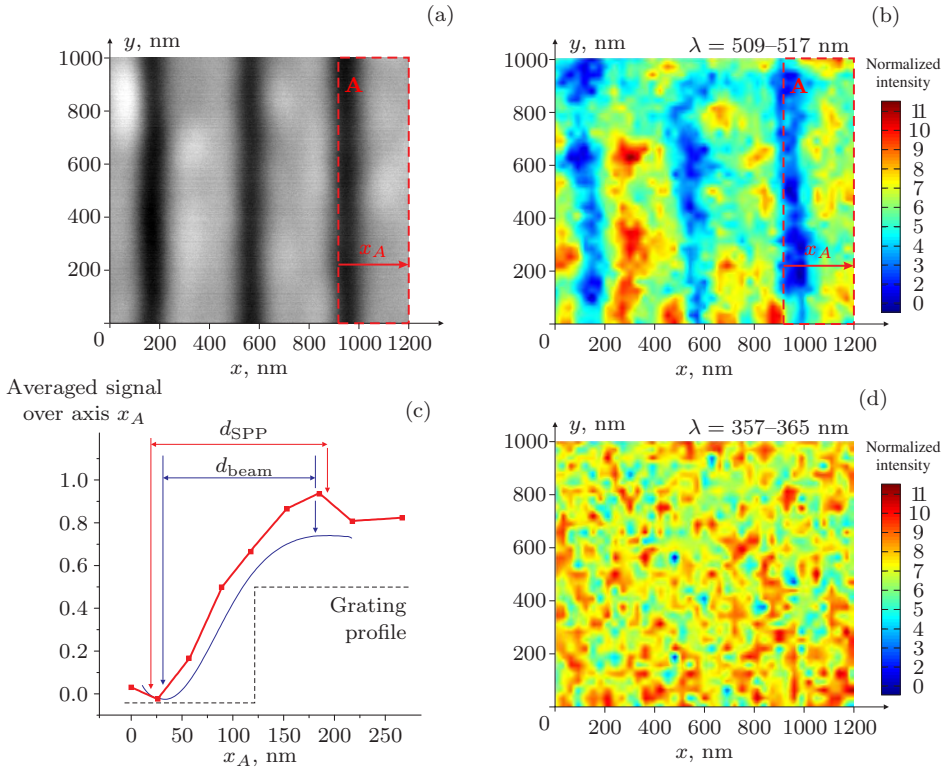

Figure 4.12: Determination of the localization of the SPP source from an HSI image of a 400 nm grating. Secondary electron image of the 400 nm period grating with area A in the vicinity of the edge of the rib, representing the step (a). White areas correspond to ribs os the grating, and black areas are spaces between ribs. Plasmonic map at $\lambda \sim 510$ nm used to determine the size of the SPP source generated by an electron beam (b). Average signal distribution in the area A along axis x_A (c), obtained from plasmonic map (b) is the step-like profile of the grating integrated by the electron beam of size d_{SPP}, which can be determined as the half distance between the points of minimum and maximum signal in the averaged signal curve: $d_{\mathrm{SPP}} = 180$ nm. Plasmonic map at $\lambda \sim 360$ nm (d) is not suitable for the determination of the SPP localization.

The same approach (detailed below) was found to be applicable for the estimation of the SPP source, generated by an electron beam, from a plasmonic map of the grating's groove, taken at the wavelength $\lambda \sim 510$ nm (Fig. 4.12b). The plasmonic map only at this wavelength bears closest

resemblance to the original structure (Fig. 4.12a). Plasmonic maps at other wavelengths either show no structure at all (due to plasmon decay rate shorter than the period of the grating), as illustrated in Figure 4.12d, or the resemblance to the structure is too remote (due to plasmon interference effects).

The intensity of the plasmon map at $\lambda = 509$–517 nm in the area A in the vicinity of the edge was averaged along the y axis to obtain a distribution of the signal along axis x_A (Fig. 4.12c). Again, assuming that the edge of the grating is ideal and is indeed a sharp step, the obtained curve would represent the integral of the step by the electron beam of a finite size. The size of the SPP source d_{SPP} can be determined as the distance between the minimum (the bottom part of the step) and maximum (the top part of the step) values of the curve. The obtained estimate of the SPP source size is $d_{\mathrm{SPP}} = 180$ nm for $\lambda \sim 510$ nm. The size of the 40 keV electron beam of current 10 nA, estimated similarly from Figure 4.12a, is $d_{\mathrm{beam}} = 150$ nm (see Figure 4.12c). Therefore, the contribution from all delocalizing mechanisms is $b = d_{\mathrm{SPP}} - d_{\mathrm{beam}} = 30$ nm.

The theoretical values of the SPP source broadening for 40 keV electron beam for the three identified mechanisms (see Section 3.7.2): scattering of primary electrons in the skin depth layer of the metal ($b_{\mathrm{br}}(40\ \mathrm{keV}) = 12$ nm, see Table 3.1), delocalization of the electrons due to Coulomb interaction with the electrons of the material ($b_{\mathrm{del}}(40\ \mathrm{keV}) = 29$ nm), and broadening due to the finite electron speed in the skin layer of the metal ($b_{\delta}(40\ \mathrm{keV}) = 53$ nm), are in a good agreement with the value, obtained in the HSI measurement of the groove of the grating. The contribution of each mechanism is yet to be determined.

Therefore, it has been demonstrated that the hyperspectral imaging technique can be used to estimate the size of the source of the surface plasmon polaritons generated by an electron beam on an unstructured metal surface. The comparison of the obtained value to the size of the electron beam allows measuring the broadening of the SPP source. The obtained estimate shows that the acquisition of plasmonic properties with the HSI technique can indeed be performed with nanoscale resolution.

4.7 Summary and conclusions

The Hyperspectral Imaging technique (HSI) for the visualization of surface plasmon polaritons in metallic structures has been developed. The technique employs the electron beam of a scanning electron microscope as a broadband plasmon source for quantitative, single-scan studies of light emission from plasmonic nanostructures, which can yield spatial emission intensity distributions, single-point emission spectra, and plasmon decay lengths with the nanoscale resolution of the electron microscope.

Demonstrative studies have illustrated the relative merits of wide- and narrow-angle light-collection geometries, and have shown that results must always be interpreted with due consideration for the dielectric properties of sample media and the assorted modes of plasmon interaction with surface features.

The size of the surface plasmon polariton source generated by a beam of free electrons on an unstructured metal surface was estimated using a hyperspectral image of a diffraction grating. The delocalization of the SPP source (broadening of the source compared to the size of the electron beam) at $\lambda \sim 510$ nm, generated by a 40 keV electron beam, was measured to be 30 nm. The obtained value lies within the theoretical estimate.

Several improvements can be applied to the developed experimental technique in order to increase its performance. First of all, the distance between the window in the SEM chamber and the spectrometer can be reduced to decrease the distance the light travels from the point of generation to the detector, resulting in better light collection efficiency. Moreover, the reflectivity of the parabolic mirror can be increased by manufacturing a new wide-angle parabolic mirror out of brass with a chromium coating. Replacing the manually controlled xy-stage with a motorized one would significantly simplify the process of alignment of the focus of the mirror with the electron beam. The technique would undoubtedly benefit from the introduction of polarization sensitivity.

Shortly after the original publication [41], a similar technique (denoted as High-Resolution Cathodoluminescence Spectroscopy) was applied to the

study of gold nanowires by the group of Professor A. Polman [54]. Plasmonic eigenmodes of gold nanowires with lengths of 500–1200 nm and 100 nm width in the spectral range 390–950 nm were studied. The plasmonic emission maps and linear intensity distributions have been acquired, spatial and spectral properties of the wire eigenmodes derived and the dispersion relation for plasmonic Au nanowire modes determined.

Possible applications of hyperspectral imaging of the plasmonic properties of nanostructures with an electron beam include the visualization of plasmon modes in single nanoparticles, particle dimers or clusters, and metamaterial nanostructures.

4.8 References

[1] S.A. Maier. *Plasmonics: fundamentals and applications*. Springer, New York, 2007.

[2] V.M. Shalaev and S. Kawata. *Nanophotonics with surface plasmons*. Elsevier, Amsterdam, 2007.

[3] W.L. Barnes, A. Dereux, and T.W. Ebbesen. Surface plasmon subwavelength optics. *Nature*, 424:824, 2003.

[4] A.V. Zayats, I.I. Smolyaninov, and A.A. Maradudin. Nano-optics of surface plasmon polaritons. *Phys. Rep.*, 408:131, 2005.

[5] R. Zia, J.A. Schuller, A. Chandran, and M.L. Brongersma. Plasmonics: the next chip-scale technology. *Mat. Today*, 9(7):20, 2006.

[6] A. Huber, N. Ocelic, D. Kazantsev, and R. Hillenbrand. Near-field imaging of mid-infrared surface phonon polariton propagation. *Appl. Phys. Lett.*, 87(8):081103, 2005.

[7] A.V. Zayats and I.I. Smolyaninov. Near-field photonics: surface plasmon polaritons and localized surface plasmons. *J. Opt. A*, 5:S16, 2003.

[8] R. Moller, U. Albrecht, J. Boneberg, B. Koslowski, P. Leiderer, and K. Dransfeld. Detection of surface plasmons by scanning tunneling microscopy. *J. Vac. Sci. Tech. B*, 9(2):506, 1991.

[9] N. Kroo, J.P. Thost, M. Volcker, W. Krieger, and H. Walther. Decay length of surface plasmons determined with a tunnelling microscope. *Europhys. Lett.*, 15(3):289, 1991.

[10] D.W. Pohl and D. Courjon. *Near field optics*. Amsterdam: Kluwer, 1993.

[11] I. Smolyaninov, A. Zayats, and O. Keller. The effect of the surface enhanced polariton field on the tunneling current of a stm. *Phys. Lett. A*, 200(6):438, 1995.

[12] M. Specht, J.D. Pedarnig, W. M. Heckl, and T.W. Hänsch. Scanning plasmon near-field microscope. *Phys. Rev. Lett.*, 68(4):476, 1992.

[13] R.B.G. de Hollander, N.F. van Hulst, and R.P.H. Kooyman. Near field plasmon and force microscopy. *Ultramicroscopy*, 57(2):263, 1995.

[14] Y.K. Kim, J.B. Ketterson, and D.J. Morgan. Scanning plasmon optical microscope operation in atomic force microscope mode. *Opt. Lett.*, 21(3):165, 1996.

[15] A.V. Zayats. Electromagnetic field enhancement in the context of apertureless near-field microscopy. *Opt. Comm.*, 161(1):156, 1999.

[16] R.W. Rendell and D.J. Scalapino. Surface plasmons confined by microstructures on tunnel junctions. *Phys. Rev. B*, 24(6):3276, 1981.

[17] B. Hecht, H. Bielefeldt, L. Novotny, Y. Inouye, and D.W. Pohl. Local excitation, scattering, and interference of surface plasmons. *Phys. Rev. Lett.*, 77(9):1889, 1996.

[18] S.I. Bozhevolnyi. Near-field mapping of surface polariton fields. *J. Microsc.*, 202(2):313, 2001.

[19] S.I. Bozhevolnyi. Localization phenomena in elastic surface-polariton scattering caused by surface roughness. *Phys. Rev. B*, 54(11):8177, 1996.

[20] A. Bouhelier, T. Huser, J.M. Freyland, H.J. Guntherodt, and D.W. Pohl. Plasmon transmissivity and reflectivity of narrow grooves in a silver film. *J. Microscopy*, 194(2):571, 1999.

[21] S.I. Bozhevolnyi and F.A. Pudonin. Two-dimensional micro-optics of surface plasmons. *Phys. Rev. Lett.*, 78(14):2823, 1997.

[22] I.I. Smolyaninov, D.L. Mazzoni, J. Mait, and C.C. Davis. Experimental study of surface-plasmon scattering by individual surface defects. *Phys. Rev. B*, 56(3):1601, 1997.

[23] J.R. Krenn, R. Wolf, A. Leitner, and F.R. Aussenegg. Near-field optical imaging the surface plasmon fields of lithographically designed nanostructures. *Opt. Comm.*, 137(1):46, 1997.

[24] T. Klar, M. Perner, S. Grosse, G. von Plesse, W. Spirkl, and J. Feldmann. Surface-plasmon resonances in single metallic nanoparticles. *Phys. Rev. Lett.*, 80(19):4249, 1998.

[25] S. Ducourtieux, V.A. Podolskiy, S. Grésillon, S. Buil, B. Berini, P. Gadenne, A.C. Boccara, J.C. Rivoal, W.D. Bragg, K. Banerjee, V.P. Safonov, V.P. Drachev, Z.C. Ying, A.K. Sarychev, and V.M. Shalaev. Near-field optical studies of semicontinuous metal films. *Phys. Rev. B*, 64(16):165403, 2001.

[26] R. Hillenbrand and F. Keilmann. Optical oscillation modes of plasmon particles observed in direct space by phase-contrast near-field microscopy. *Appl. Phys. B*, 73(3):1432, 2001.

[27] K. Imura, H. Okamoto, M.K. Hossain, and M. Kitajima. Visualization of localized intense optical fields in single gold-nanoparticle assemblies and ultrasensitive Raman active sites. *Nano Lett.*, 6(10):2173, 2006.

[28] H. Okamoto and K. Imura. Near-field imaging of optical field and plasmon wavefunctions in metal nanoparticles. *J. Mat. Chem.*, 16(40):3920, 2006.

[29] S.I. Bozhevolnyi, B. Vohnsen, and E.A. Bozhevolnaya. Transfer functions in collection scanning near-field optical microscopy. *Opt. Comm.*, 172(1):171, 1999.

[30] P.E. Batson. Damping of bulk plasmons in small aluminum spheres. *Solid State Comm.*, 34(6):477, 1980.

[31] P.E. Batson. Surface plasmon coupling in clusters of small spheres. *Phys. Rev. Lett.*, 49(13):936, 1982.

[32] Z.L. Wang and J.M. Cowley. Surface plasmon excitation for supported metal particles. *Ultramicroscopy*, 21(1):77, 1987.

[33] M. Bosman, V.J. Keast, M. Watanabe, A.I. Naaroof, and M.B. Cortie. Mapping surface plasmons at the nanometre scale with an electron beam. *Nanotechnology*, 18:165505, 2007.

[34] J. Nelayah, M. Kociak, O. Stephan, F.J.G. de Abajo, M. Tence, L. Henrard, D. Taverna, I. Pastoriza-Santos, L.M. Liz-Marzan, and C. Colliex. Mapping surface plasmons on a single metallic nanoparticle. *Nat. Phys.*, 2007.

[35] N. Yamamoto, K. Araya, A. Toda, and H. Sugiyama. Light emission from surfaces, thin films and particles induced by high-energy electron beam. *Surf. Interf. Anal.*, 31:79, 2001.

[36] N. Yamamoto, H. Sugiyama, and A. Toda. Cherenkov and transition radiation from thin plate crystals detected in the transmission electron microscope. *Proc. Royal Soc. Lond.*, 452(1953):2279, 1996.

[37] N. Yamamoto, H. Itoh, V. Grillo, S.F. Chichibu, S. Keller, J.S. Speck, S.P. DenBaars, U.K. Mishra, S. Nakamura, and G. Salviati. Cathodoluminescence characterization of dislocations in gallium nitride using a transmission electron microscope. *J. Appl. Phys.*, 94(7):4315–4319, 2003.

[38] K. Akiba, N. Yamamoto, V. Grillo, A. Genseki, and Y. Watanabe. Anomalous temperature and excitation power dependence of cathodoluminescence from inas quantum dots. *Phys. Rev. B*, 70:165322, 2004.

[39] N. Yamamoto, K. Araya, and F.J. Garcia de Abajo. Photon emission from silver particles induced by a high-energy electron beam. *Phys. Rev. B*, 64:205419, 2001.

[40] N. Yamamoto, M. Nakano, and T. Suzuki. Light emission by surface plasmons on nanostructures of metal surfaces induced by high-energy electron beams. *Surf. Interf. Anal.*, 38:1725, 2006.

[41] M.V. Bashevoy, F. Jonsson, K.F. MacDonald, Y. Chen, and N.I. Zheludev. Hyperspectral imaging of plasmonic nanostructures with nanoscale resolution. *Opt. Express*, 15(18):11313, 2007.

[42] J.E. McFee, C. Anger, S. Achal, and T. Ivanco. Landmine detection using passive hyperspectral imaging. *Chem. Biol. Sensing*, 6554:55404, 2007.

[43] T. Ivanco, S. Achal, J.E. Mcfee, C. Anger, and J. Young. Real-time airborne hyperspectral imaging of land mines. *Detection And Remediation Technologies For Mines And Minelike Targets Xii*, 6553:55315, 2007.

[44] R. Harig, G. Matz, P. Rusch, H.H. Gerhard, J.H. Gerhard, and V. Schlabs. Infrared remote sensing of hazardous vapours: Surveillance of public areas during the FIFA Football World Cup 2006. *Sensors, And Command, Control, Communications And Intelligence (C31) Technologies For Homeland Security And Homeland Defense Vi*, 6538:Z5381, 2007.

[45] X.F. Chen, T.A. Warner, and D.J. Campagna. Integrating visible, near-infrared and short-wave infrared hyperspectral and multispectral thermal imagery for geological mapping at Cuprite, Nevada. *Remote Sensing Of Envir.*, 110(3):344, 2007.

[46] E.A. Cloutis. Hyperspectral geological remote sensing: Evaluation of analytical techniques. *Int. J. Remote Sensing*, 17(12):2215, 1996.

[47] R.G. Resmini, M.E. Kappus, W.S. Aldrich, J.C. Harsanyi, and M. Anderson. Mineral mapping with hyperspectral digital imagery collection experiment (HYDICE) sensor-data at Cuprite, Nevada, USA. *Int. J. Remote Sensing*, 18(7):1553, 1997.

[48] F.A. Kruse. Identification and mapping of minerals in drill core using hyperspectral image analysis of infrared reflectance spectra. *Int. J. Remote Sensing*, 17(9):1623, 1996.

[49] R.O. Green, M.L. Eastwod, C.M. Sarture, T.G. Chrien, M. Aronsson, B.J. Chippendale, J.A. Faust, B.E. Pavri, C.J. Chovit, M. Solis, M.R. Olah, and O. Williams. Imaging spectroscopy and the Airborne Visible/Infrared Imaging Spectrometer (AVIRIS). *Remote Sensing of Envir.*, 65:227, 1998.

[50] A. Barducci and I. Pippi. Retrieval of atmospheric parameters from the hyperspectral image data. *Igarss '95 International Geoscience And Remote Sensing Symposium, Quantitative Remote Sensing For Science And Applications*, 1–3:138, 1995.

[51] E.D. Palik. *Handbook of optical constants of solids*. Academic Press, Orlando, 1985.

[52] M.V. Bashevoy, F. Jonsson, A.V. Krasavin, N.I. Zheludev, Y. Chen, and M.I. Stockman. Generation of traveling surface plasmon waves by free-electron impact. *Nano Lett.*, 6(6):1113, 2006.

[53] A.V. Krasavin, K.F. MacDonald, and N.I. Zheludev. *Active plasmonics*. Nanophotonics with Surface Plasmons. Elsevier Science, 2007.

[54] E.J.R. Vesseur, R. de Waele, M. Kuttge, and A. Polman. Direct observation of plasmonic modes in Au nanowires using high-resolution cathodoluminescence spectroscopy. *Nano Lett.*, 7(9):2843, 2007.

Chapter 5

Excitation of localized plasmon modes in nanoparticle dimers with an electron beam

5.1 Synopsis

Hyperspectral imaging (HSI) with a scanning electron beam has been used to study localized surface plasmon excitations of singular and dimeric gold decahedron-shaped nanoparticles with nanoscale resolution. Simultaneous visualization of a spectral hybridization mode and spatial symmetric/asymmetric dimer modes in a single measurement has been demonstrated.

The concept of hyperspectral imaging of plasmonic excitations for a nanodimer, consisting of two metallic nanoparticles, is illustrated in Section 5.3. In Section 5.4 the results of HSI measurements of a single 100 nm decahedron-shaped gold nanoparticle are presented. Hyperspectral imaging analysis of "short" and "long" dimers (consisting of the same particles at different distances from each other), including plasmonic emission maps, spectral symmetric/asymmetric and spatial hybridization modes is performed in the following Section. The interpretation of the obtained experimental results of electron beam excitation of nanodimers, based on the classical model of forced oscillations of two oscillatory circuits with AC power supply and a capacitance feedback, is presented in Section 5.6.

5.2 Introduction

Single metallic nanoparticles and nanodimers have become an essential part of nanophotonics. High field localization in the vicinity of a dimer allows for sufficient Raman signal from single molecules [1–7]. As emission properties of a dimer highly depend on the interparticle distance and boundary state, it makes them ideal candidates as biological and chemical nano sensors [8–11], and plasmonic enhancing nanoantennae [12–14]. A key to the design of future all-optical computer components such as plasmonic nanoparticle chain waveguides [15–22] and single nanoparticle switches [23–28] lies within the understanding of plasmonic properties of single metal nanoparticles and nanodimers.

Over the years a number of methods have been suggested for investigation of plasmons on a nanoscale. The first optical spectroscopic techniques [29] and the study of light emission from tunnel junctions [30–36] were unable to provide a correlation between the geometry of a nano-sample and plasmonic excitations. Most common spatially resolved techniques such as Scanning Near-field Optical Microscopy (SNOM) [37, 38], Scanning Tunneling Microscopy (STM) [39] and Electron Energy Loss Spectroscopy (EELS) [40, 41] allow excitation, detection and mapping of plasmonic excitations with spacial resolution up to $\sim$ 10 nm or less. Transmission/scanning electron microscopes with cathodoluminescence imaging setup were used to map plasmonic excitations at a single wavelength of single nanoparticles and touching spheres [42, 43].

The comparison of experimental data of optical and electron beam excitation of single metallic nanoparticles and related structures (nanoparticle dimers, trimers, waveguides, etc.) with theoretical models suggests that the dominant mechanism of light emission by such structures is due to excitation of either propagating or localized surface plasmon modes, as opposed to the "bulk" photo- and cathodoluminescence of metal films [14, 40]. Therefore, electron-induced photon-emission of nanostructures, described in this Chapter, will be referred to as "plasmonic" excitations of the nanoparticles and nanodimers.

In this Chapter it is shown that with the Hyperspectral imaging [44] with an electron beam based on a scanning electron microscope with a cathodoluminescence setup technique, it is possible to map surface plasmons on both single nanoparticles and dimers in the whole visible and near-infrared part of the spectrum and obtain both spatial and spectral modes, all in a single measurement. This approach allows fast and comprehensive analysis of plasmonic structures excited by an electron beam with a nanoscale resolution.

5.3 Hyperspectral imaging of metallic nanoparticle dimers

The Hyperspectral imaging (HSI) of plasmonic excitations of nanostructures with an electron beam was described and illustrated on a metallic grating in the previous Chapter. In this Section the application of this technique to the study of localized nanoparticle dimer excitation with a beam of electrons is detailed.

The technique uses an electron beam to probe the sample in an orderly fashion and detect the light emission response at every point in 350–1150 nm wavelength range. In this Chapter the sample consists of a carbon film substrate and a pair of gold nanoparticles (Fig. 5.1a). The HSI measurement results in an "image," a three dimensional array of hundreds of light emission intensity distributions of the sample at each wavelength. This is often referred to as a "data cube" (Fig. 5.1b).

The "data cube" can be "mined" for various information such as photon emission maps (by slicing the data cube into xy-planes, as shown in Figure 5.1b), induced emission spectra from particular parts of the sample (following vertical lines at a point (x_p, y_q) of the data cube) and linear spacial distributions at a specific wavelength (following horizontal lines at a point (λ_s, y_r) of the data cube). Applied to the single nanoparticle or a nanodimer on a carbon substrate, this technique allows for the production plasmon excitation maps of the sample (by subtracting the background signal

from the substrate), spectral distributions and spatial modes excited by the electron beam in a single measurement.

The setup, used to demonstrate the excitation of surface plasmon polaritons with an electron beam on an unstructured metal surface, was described in the previous Chapter. Without any modifications it was applied for hyperspectral imaging of nanoparticles and nanodimers. Due to poor signal–noise ratio in the infrared region for the samples used in this chapter, the results are presented in the 350–850 nm spectral region.

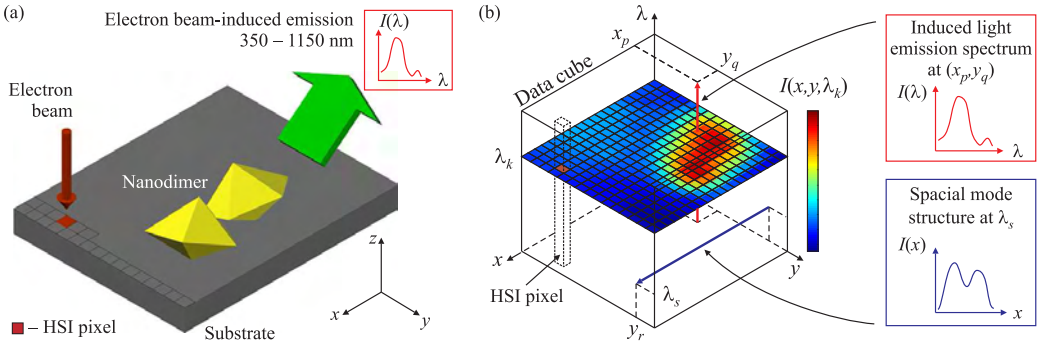

Figure 5.1: (a) The hyperspectral imaging concept illustrated for a nanodimer on a carbon substrate. At each electron beam injection point in the sample xy-plane, i.e. each image pixel, the entire emission spectrum from the electron beam-induced radiation is sampled simultaneously at a number of discrete wavelengths λ_k. (b) The data cube generated can be mined to produce single-wavelength spatial intensity distributions of induced emission (xy-planes), point spectra (vertical lines), and wavelength-specific linear emission intensity profiles (horizontal lines).

The hyperspectral imaging of plasmonic excitations was performed on three samples: a single gold decahedron-shaped 100 nm nanoparticle, and two dimers, consisting of such nanoparticles: a "short" dimer with a $D = 50$ nm gap between the particles and a "long" dimer with a $D = 150$ nm gap. The results are presented and discussed in the following Sections.

5.4 HSI of single nano decahedron

The hyperspectral imaging was first performed on a single decahedron-shaped 100 nm gold particle deposited on a carbon substrate. The suspension of

gold nanoparticles was prepared by the group of Professor L.M. Liz-Marzán, Universidade de Vigo, Spain. The preparation procedure is described below, following [45].

The formation of particles is the result of the reduction of $HAuCl_4$ using DMF (Dimethylformamide, N,N-dimethylformamide, a common solvent) in the presence of small (2–3 nm) gold seeds with uniform size distribution, using $NaBH_4$ as a strong reducing agent and polyvinylpyrrolidone as a stabilizer. Ultrasound was used to provide controlled and reproducible synthesis of monodisperse decahedra with high yield. The large proportion of the particles obtained by this procedure had an extremely regular pentagonal symmetry (80–90 % of the particles). Most of the remaining particles having the shape of triangular prisms (Fig. 5.2a).

The shape of the nanoparticles was determined with a transmission electron microscope in a study by Sánchez-Iglesias et al. [45]. Imaged at different angles, the particles were nearly perfect pentagonal bi-pyramids of equal equilateral-triangle faces (decahedra), but with somewhat rounded edges (Fig. 5.2b, c). The height and side length of each bi-pyramid is 40 nm and 55 nm correspondingly.

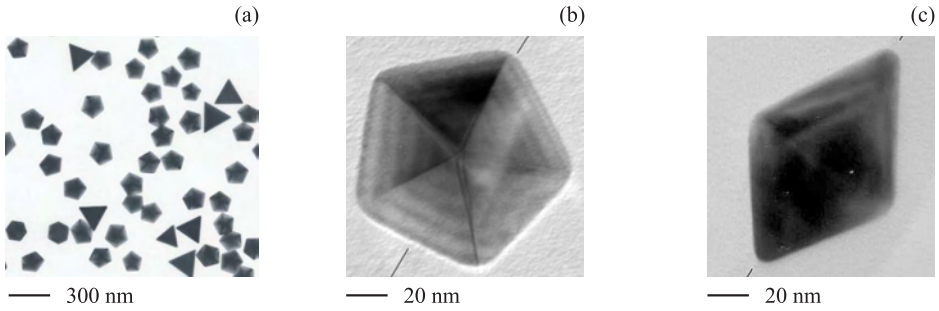

Figure 5.2: TEM image of the particles obtained by the experimental procedure described in [45]. The vast majority of the particles were nearly perfect pentagonal bi-pyramids of equal equilateral-triangle faces (decahedra) (80–90 % of the particles). The most of the remaining particles had the shape of triangular prisms (a). The evidence of the decahedron-like shape was seen in transmission electron images of a single nanoparticle taken at different angles (b, c). After ref. [45].

A drop of DMF suspension of gold decahedra, prepared according to the described procedure, was placed on a carbon film formed in the 500×500 μm openings of the copper grid (Fig. 5.3a, b). After evaporation, the random arrangement of decahedra on the carbon substrate could be observed (Fig. 5.3c): nanoparticles formed large groups, trimers, dimers (width different separation gap). Isolated particles, with the distance to the closest neighbors up to 500 nm, were also present.

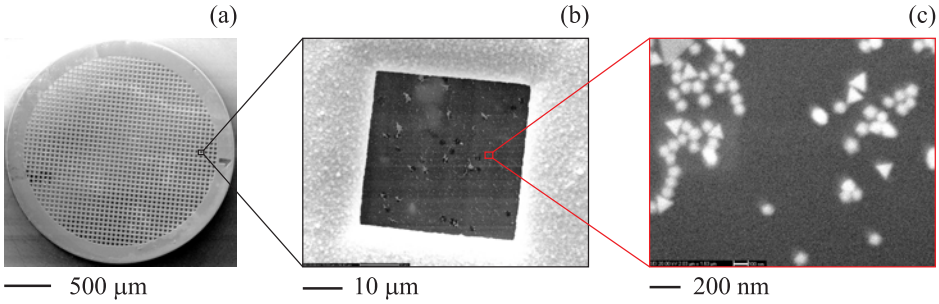

Figure 5.3: A drop of DMF suspension of the nanoparticles was placed on a carbon film formed in the openings of the copper grid, as seen on the secondary electron image taken with a scanning electron microscope (a, b). After evaporation, the random arrangement of the decahedra on the carbon substrate could be observed. Nanoparticles formed large groups, trimers, dimers (with different separation gaps). Isolated particles were also present (c).

The first hyperspectral imaging experiment was performed on an isolated gold decahedron on a carbon substrate. A 40 keV electron beam of 500 pA current was used. The size of the created SPP source, or plasmonic "probe," estimated according to the procedure detailed in Section 4.6, is 50 nm. The size of the probe does not allow for resolving the features of the nanoparticles, but provides sufficient signal to perform HSI. The 21×17 point hyperspectral image of the area 500×400 nm encompassing a gold decahedron was taken, and the plasmonic data: plasmonic maps, spectral and spatial mode, was acquired. The results are presented in Figure 5.4.

After the acquisition of the HSI data, the corresponding data cube was initially mined for spectral (Fig. 5.4a, solid black curve) and spatial (Fig. 5.4b) distributions of light emitted by the nanoparticle (Fig. 5.4c) due to electron beam excitation. The former was acquired by extracting light

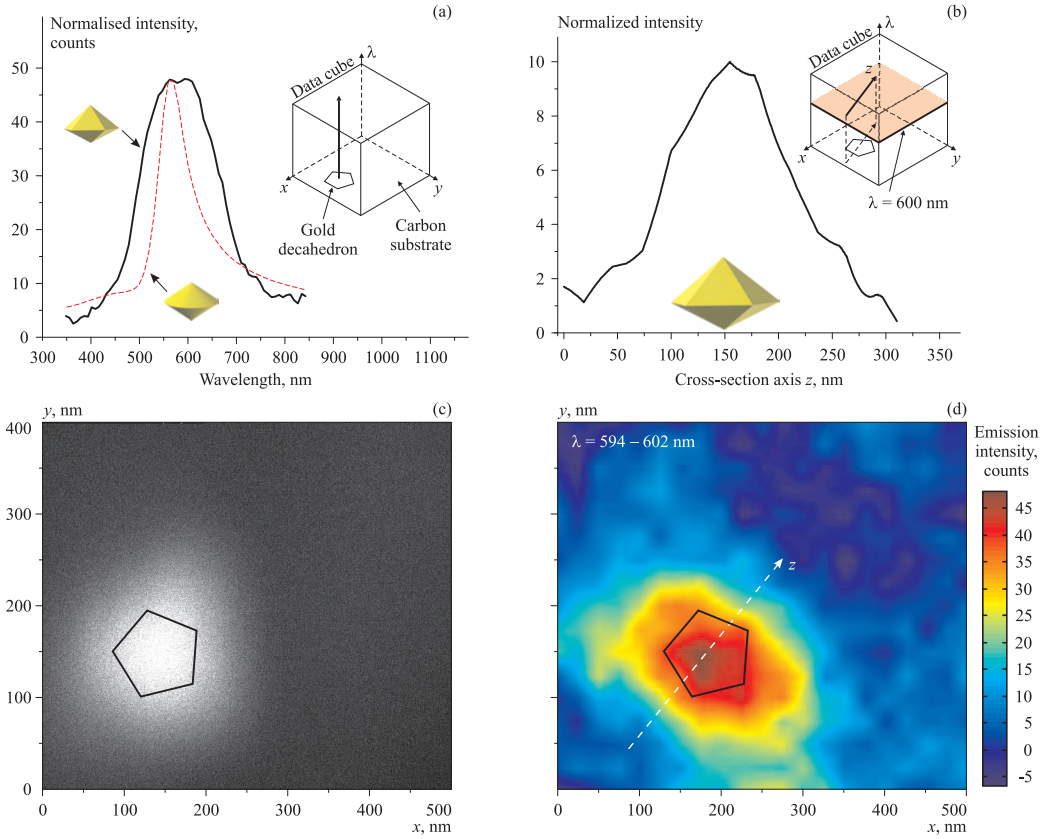

Figure 5.4: Hyperspectral imaging of a single 100 nm gold decahedron-shaped nanoparticle. (a) Electron beam-induced light spectrum by the nanoparticle obtained from the HSI data cube by extracting data along vertical axis passing through the nanoparticle (black curve) and theoretical spectra obtained by a boundary element method [46] for a bi-conical particle with radius 55 nm and hight 40 nm (red dashed curve). (b) Spatial distribution of light emitted by the decahedron at the wavelength of maximum emission, extracted along z axis, crossing the nanoparticle in xy plane at $\lambda = 600$ nm. (c) Secondary electron image of the nanoparticle. (d) Spatial plasmonic emission intensity distribution obtained by slicing the hyperspectral data cube in the xy plane (averaged over 8 nm wavelength interval): $\lambda = 594$–602 nm, where the particle is in plasmon resonance. The white dotted line indicates the position of axis z used to extract spatial distribution of the intensity.

intensity along the vertical axis of the data cube placed in the middle of the nanoparticle (see inset in Figure 5.4a). The obtained spectrum has a single peak centered around $\lambda = 600$ nm. The spatial distribution was acquired at the same wavelength by collecting the light intensity along the line in the data cube, passing through the middle of the nanoparticle, in the corresponding xy plane $\lambda = 600$ nm (see inset in Figure 5.4b). The spectral distribution also shows a single peak centered at the middle of the nanoparticle. The plasmonic map, extracted from the data cube by averaging xy distributions of light in the wavelength region $\lambda = 594$–602 nm, is presented in Figure 5.4d (where the distribution is averaged over an 8 nm wavelength interval to reduce noise).

The measured spectrum of electron beam-induced photon emission from a single nano decahedron (black curve, Figure 5.4a) has been compared to the theoretical spectrum, obtained a numerical technique, developed by Professor F.J. García de Abajo [46]. This technique allows the calculation of electron-induced photon-emission spectra, using the numerical solution of Maxwell's equations by the boundary element method, from structures of arbitrary shape and dielectric function. The theoretical approach is outlined in Appendix B.

For the simulations the nano decahedron was approximated by a bi-conical structure with radius 55 nm and height 40 nm, illuminated by a 40 keV electron beam positioned in the middle of the nanoparticle (Fig. 5.5a). The theoretical electron-induced photon-emission spectra is depicted in Figure 5.4a (red dashed curve). The modeled and measured spectra (Fig. 5.4a, black solid curve) correlate reasonably well.

The broadening of the experimental curve, compared to the theoretical spectrum, can be accounted for by a number of things: the model does not include the interaction between the nanoparticle and the carbon substrate (Fig. 5.5b); in the experiment the cross section of the electron beam is comparable to the size of the nanoparticle; the orientation of the decahedron relative to the electron beam is unclear and a 10–30 degrees tilt of the nanoparticle can influence the induced spectrum.

The size of the SPP source used to acquire the results, obtained in the HSI measurements described in this Chapter, cannot resolve the fine structure of

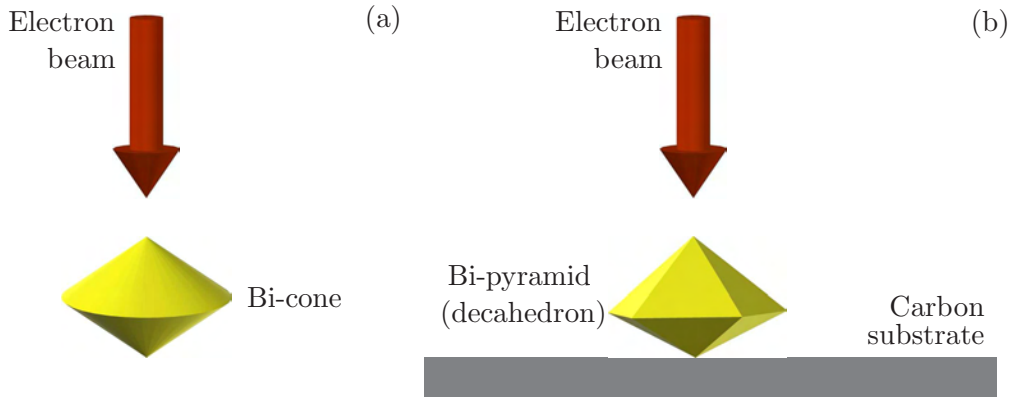

Figure 5.5: The geometrical configuration of the theoretical model of the single decahedron-shaped nanoparticle excited by an electron beam. The bi-pyramid (decahedron) was approximated by a bi-cone with with radius 55 nm and height 40 nm (a). Experimental configuration (b).

the spatial modes of the nanoparticle. Moreover, it was shown [42] that the experimental observation of the modes requires polarization sensitivity and higher angular selectivity. The light emission of each mode is polarized and confined in a relatively narrow angle. The geometry of the light collection system with the "wide mirror" does not allow for the high angular selectivity, causing the overlap of the detected modes.

However, it was sufficient to resolve peculiar features of the interaction between two nanoparticles, forming a nanodimer. The HSI of a single nanoparticle was used to demonstrate the capabilities of the technique on the nanoscale, and also to be used as a reference for the hyperspectral images of dimer structures. The hyperspectral imaging of two types of dimers, formed of such nanoparticles, is presented in the following Section.

5.5 HSI of "short" and "long" dimers

The second set of experiments was performed on a "short" dimer with a $D = 50$ nm gap between the 100 nm decahedron-shaped gold particles, deposited on a carbon substrate, and a "long" dimer with a $D = 150$ nm gap (see Figure 5.6). It was expected that the spectral and spatial distributions

of electron-beam induced emission would 1) show new modes compared to a single decahedron (due to the interaction between the particles), and 2) would differ between the "short" and "long" dimers due to weakening between the constituent nanoparticles with distance.

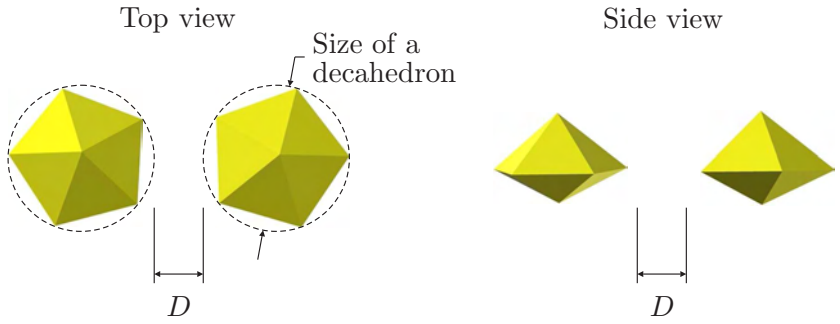

Figure 5.6: Top and side views of a dimer, consisting of two 100 nm decahedron-shaped nanoparticles separated by a gap D. Two types of dimers have been investigated: a "short" dimer with $D = 50$ nm and a "long" dimer with $D = 150$ nm.

Plasmonic maps acquired from the "short" dimer ($D = 50$ nm) possess striking differences from the analogous distributions of single nanoparticle (see Figure 5.7). It can be seen that the emission of light due to excitation of localized plasmons drastically depends on the wavelength. In the ranges $\lambda = 425$–433 nm, $\lambda = 540$–548 nm, $\lambda = 671$–679 nm, and $\lambda = 842$–850 nm (Fig. 5.7b, c, e, f respectively) that distribution is localized on one or other nanoparticle within the dimer (the intensity distributions are averaged over 8 nm wavelength intervals to reduce noise). However, as can be seen from the plasmonic map in Figure 5.7d, at the wavelengths around $\lambda = 600$ nm the emission of light by a dimer reaches a peculiar state: the dimer emits light like a single nanoparticle. This state is attributed to the excitation of a *hybridization mode* [47, 48]. This mode has only been observed in a narrow range of wavelengths close to the plasmonic resonance of a single nanoparticle.

Plasmonic maps of a "short" dimer, presented in Figures 5.7b–f, exhibit an asymmetry of the electron-induced emission relative to the axis of the dimer. This can be attributed to the following: the axis of each nanoparticle

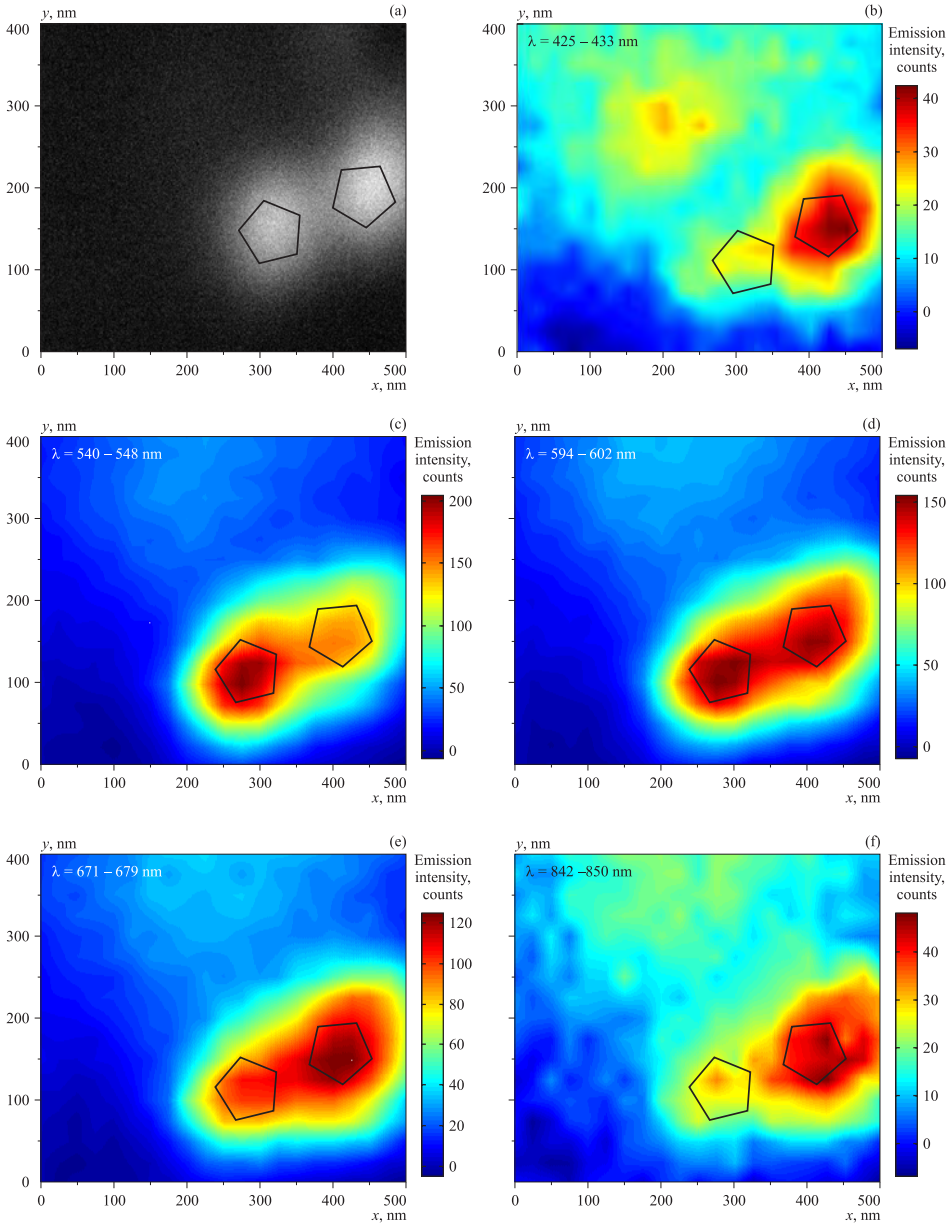

Figure 5.7: Hyperspectral imaging of a short ($D = 50$ nm) dimer (a): spatial plasmonic emission intensity distributions obtained by slicing the hyperspectral data cube in the xy plane (averaged over 8 nm wavelength intervals). Localized excitations on one of the nanoparticles in the ranges $\lambda = 425$–433 nm (b), $\lambda = 540$–548 nm (c), $\lambda = 671$–679 nm (e), $\lambda = 842$–850 nm (f). Excitation of hybridization mode at $\lambda = 625$–633 nm: dimer emits as a single particle (d).

is most likely to be non-perpendicular to the plane of the substrate, therefore the mutual orientation of the nanoparticles can be asymmetric.

The evidence of excitation of the hybridization mode was not found on the long ($D = 150$ nm) dimer, consisting of two decahedron-shaped 100 nm nanoparticles at a distance of 150 nm (Fig. 5.8a). The lack of coupling between the particles, resulting in non-hybridized (independent) emission by each particle, is demonstrated in plasmonic maps of the long dimer in the wavelength ranges $\lambda = 563$–571 nm, $\lambda = 617$–625 nm and $\lambda = 710$–718 nm (Fig. 5.8c–d).

Introduction of a second nanoparticle at a $D = 50$ nm distance, in the "short dimer" case, results in the splitting of a single nanoparticle's spectrum into two modes of emission by the dimer. The evidence for the splitting can be seen in (Fig. 5.9a), representing three spectral distributions: the spectrum of a single nanoparticle (dashed black curve), centered at $\lambda = 600$ nm, and spectra extracted from the middle of each nanoparticle within the dimer (blue and red curves). The lines inside the data cube, along which the spectra of nanoparticles within the dimer was extracted, are indicated in the inset to Figure 5.9a.

The splitting of the single nanoparticle's spectrum seen on the dimer is attributed to the excitation of symmetric and asymmetric modes of the dimer. In the symmetric mode each of the nanoparticles within the dimer oscillates in phase with one another, while in the asymmetric case the oscillations of the particles are anti-phased. As a result, the maxima of light emission spectra obtained from each particle exhibits a small shift from the peak of emission of a isolated nanoparticle (Fig. 5.9a).

For the long ($D = 150$ nm) dimer the splitting of spectra has not been observed, as shown in Figure 5.9b. The maxima of emission spectra of a single nanoparticle (shown as a black dotted curve) and each of the nanoparticles within the dimer (blue and black curves) coincide. The excitation of symmetric and asymmetric modes in this case is impossible due to the weak interaction between the nanoparticles.

Spatial intensity distribution of light emission from the short ($D = 50$ nm) dimer was obtained by mining the data cube along the axis of the dimer in

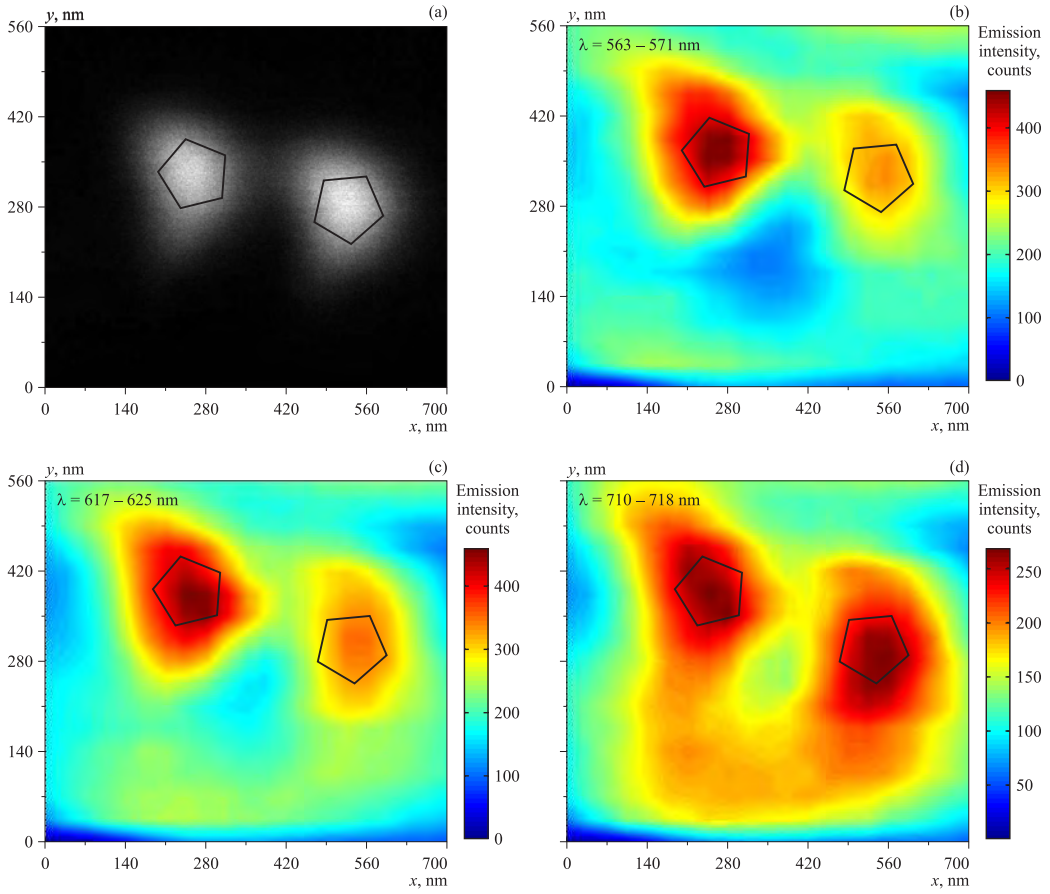

Figure 5.8: Hyperspectral imaging of a long ($D = 150$ nm) dimer (a): spatial plasmonic emission intensity distributions obtained by slicing the hyperspectral data cube in the xy plane (averaged over 8 nm wavelength intervals). Plasmon emission maps of a non-hybridization regime due to weak coupling between nanoparticles at $\lambda = 563$–571 nm (b), $\lambda = 617$–625 nm (c), and $\lambda = 710$–718 nm (d).

the planes corresponding to wavelengths $\lambda_1 = 600$ nm and $\lambda_2 = 815$ nm (Fig. 5.9c). As can be seen from spatial distribution along line z_2, corresponding to $\lambda_2 = 815$ nm (black line), the plasmon excitation is localized on one of the nanoparticles within the dimer. However, on $\lambda_1 = 600$ nm the dimer emits light as a single particle (red curve). This phenomena is attributed to the excitation of hybridization mode, illustrated earlier on a plasmonic map on the same wavelength (Fig. 5.7d).

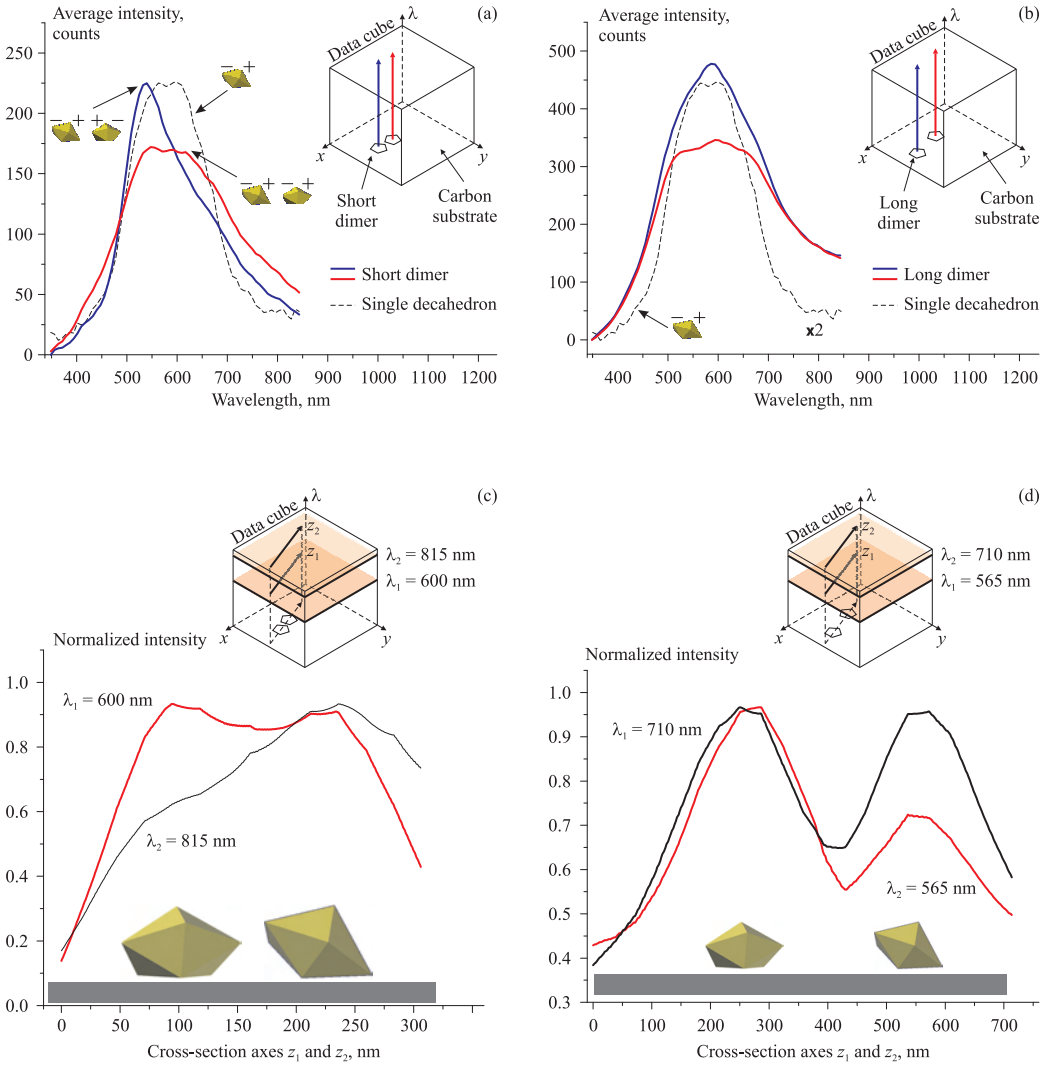

Figure 5.9: Spectral and spatial distributions of light emitted by short ($D = 50$ nm) and long ($D = 150$ nm) dimers with 40 kV electron beam excitation. (a) Splitting of the single nanoparticle mode spectrum for a short dimer: maxima of spectra of emission of each nanoparticle (red and blue curves) exhibits a small shift from the peak of emission of a isolated nanoparticle (black dashed curve). (b) The splitting was not observed for the long dimer. (c) Hybridization spacial mode of the short dimer at $\lambda_1 = 600$ nm (solid red line) compared to a localized excitation of one of the nanoparticles within the dimers at $\lambda_2 = 815$ nm. The excitation of the hybridization mode is previously illustrated on a plasmonic map at λ_1 (Fig. 5.7d). (d) Non-hybridized emission of the long dimer: the emission of each nanoparticle is independent of the other.

Spatial distributions along the axis of a long ($D = 150$ nm) dimer do not exhibit any interesting features (Fig. 5.9d). At all wavelengths in the studied region the emission of each nanoparticle within the dimer is independent. The excitation of the hybridization mode cannot be observed.

It has therefore been demonstrated that the developed hyperspectral imaging technique allows for quick visualization of nanoparticles and systems of nanoparticles, such as dimers, and analysis of spectral and spatial modes. Excitation of the hybridization mode and the spectral symmetric/asymmetric modes in a nanodimer has been achieved.

5.6 Interpretation of the coupled plasmon modes in nanoparticle dimers

The phenomena, observed in HSI measurements of nanodimers, described in the previous Section, can be illustrated on a classical model of forced oscillations of two coupled circuits. Specifically, the gain-frequency characteristic of current oscillations of the model as a function of coupling factor can be directly compared to the detected spectra of "short" and "long" nanodimers. Consideration of plasmonic nanoparticles as elements of electrical circuits became popular after a study performed by Nader Engheta [49].

Consider a system of two parallel oscillatory circuits with capacitive feedback (Fig. 5.10a). Each of the circuits, representing one of the nanoparticles within a dimer, consists of a resistor G_i, capacitor C_i and inductor L_i, $i = 1, 2$. The system also has an AC power supply J and a capacitor C_f, providing feedback between the circuits.

The correspondence between the components of the model and the experiment (Fig. 5.10b) is the following. Electromagnetically coupled nanoparticles within the dimer act like oscillatory circuits with capacitance feedback. Excitation of the dimer with the electron beam (acting as the AC power supply for the circuits) results in generation of light with intensity I_i from each nanoparticle (currents U_i in the model), $i = 1, 2$.

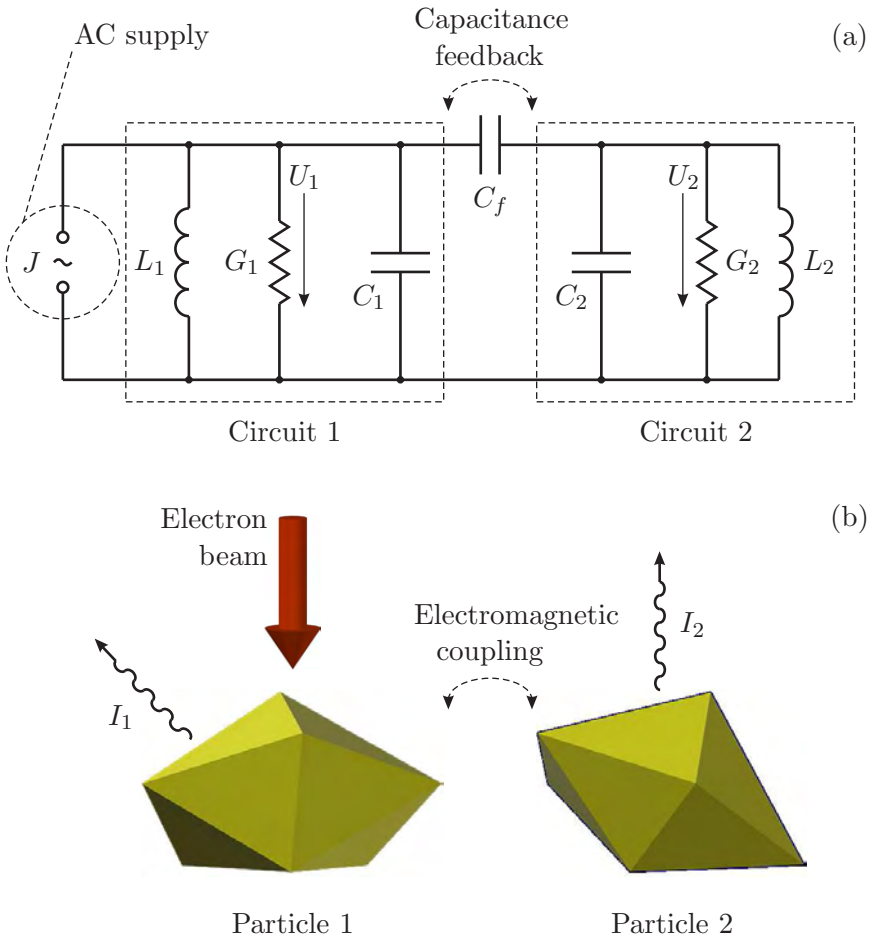

Figure 5.10: The system of coupled parallel oscillatory circuits with a capacitance feedback (a): each of the circuits consists of a resistor G_i, capacitor C_i and inductor L_i, $i = 1, 2$. The system also has an AC power supply J and a capacitor C_f, providing feedback between the circuits. Nanodimer excited by an electron beam (b): electromagnetically coupled gold decahedron-shaped particles 1 and 2. The behavior of the coupled nanoparticles under electron beam excitation is analogous to the behavior of two circuits with a AC power supply and a capacitance feedback.

Currents U_1 and U_2 in each circuit are defined by the following system of integro-differential equations:

$$\begin{aligned} C_1\frac{dU_1}{dt} + G_1U_1 + \frac{1}{L_1}\int U_1dt + C_f\frac{d(U_1-U_2)}{dt} &= J, \\ C_2\frac{dU_2}{dt} + G_2U_2 + \frac{1}{L_2}\int U_2dt + C_f\frac{d(U_2-U_1)}{dt} &= 0. \end{aligned}$$

Taking a first time derivative from each of the equations, one can obtain:

$$\frac{d^2U_1}{dt^2} + 2\alpha_1\frac{U_1}{dt} + \omega_{01}^2 U_1 + k_1^C\frac{d^2U_2}{dt^2} = \frac{1}{C_{1\Sigma}}\frac{dJ}{dt}, \tag{5.1}$$

$$\frac{d^2U_2}{dt^2} + 2\alpha_2\frac{U_2}{dt} + \omega_{02}^2 U_2 + k_2^C\frac{d^2U_1}{dt^2} = 0. \tag{5.2}$$

Here $C_{1\Sigma} = C_1 + C_f$, $C_{2\Sigma} = C_2 + C_f$ — the total capacities of partial subsystems, $\alpha_1 = G_1/2C_{1\Sigma}$ and $\alpha_2 = G_2/2C_{2\Sigma}$ — damping coefficients of each circuit, $\omega_{01} = 1/\sqrt{L_1C_{1\Sigma}}$ and $\omega_{02} = 1/\sqrt{L_2C_{2\Sigma}}$ — partial frequencies of the circuits, $k_1^C = C_f/C_{1\Sigma}$ and $k_2^C = C_f/C_{2\Sigma}$ — coupling coefficients of circuits.

Consider J a harmonic function of time with frequency ω and complex amplitude J_m:

$$J(t) = J_m e^{j\omega t}.$$

Equations (5.1), (5.2) will then take the form:

$$(G_1 + jB_{1\Sigma})U_{1m} - jB_fU_{2m} = Y_1U_{1m} - jB_fU_{2m} = J_m, \tag{5.3}$$

$$-jB_fU_{1m} + (G_2 + jB_{2\Sigma})U_{2m} = -jB_fU_{1m} + Y_2U_{2m} = 0. \tag{5.4}$$

Here U_{1m} and U_{2m} are complex amplitudes of U_1 and U_2; $Y_1 = G_1 + jB_{1\Sigma}$, $Y_2 = G_2 + jB_{2\Sigma}$ — complex conductivities of circuits; $B_{1\Sigma} = \omega C_{1\Sigma} - 1/\omega L_1$, $B_{2\Sigma} = \omega C_{2\Sigma} - 1/\omega L_2$, $B_f = \omega C_f$.

Expressions for complex amplitudes U_{1m} and U_{2m} can be found from the system (5.3)–(5.4). These expressions are cumbersome and not essential for the current analysis. The behavior of the system of two coupled circuits can be described using the following parameters: detuning factors for each circuit:

$$\xi_{01} = \omega_{01}\frac{C_{1\Sigma}}{G_1}\left(\frac{\omega}{\omega_{01}} - \frac{\omega_{01}}{\omega}\right), \qquad \xi_{02} = \omega_{02}\frac{C_{2\Sigma}}{G_2}\left(\frac{\omega}{\omega_{02}} - \frac{\omega_{02}}{\omega}\right);$$

quality factors for each circuit:

$$Q_1 = \omega_{01}\frac{C_{1\Sigma}}{G_1}, \qquad Q_2 = \omega_{02}\frac{C_{2\Sigma}}{G_2},$$

and the coupling factor:

$$A = \omega C_f/\sqrt{G_1G_2}.$$

Consider a system with $\xi_{01} = \xi_{02} = \xi$ and $Q_1 \cong Q_2$. The resonance condition in this case can be written as:

$$\xi \left(1 - \frac{A^2}{1+\xi^2}\right) = 0. \tag{5.5}$$

From Equation 5.5 one can show that the discussed system of coupled circuits has two distinctive states, depending on the value of the coupling factor A.

For $A < 1$ the system has only one resonance at the frequency of the external force:

$$\omega = \omega_0.$$

For $A > 1$ the maximum of $|U_{2m}|$ (resonance) is achieved at frequencies:

$$\omega_1 = \frac{\omega_0}{\sqrt{1+\sqrt{k^2-d^2}}}, \qquad \omega_2 = \frac{\omega_0}{\sqrt{1-\sqrt{k^2-d^2}}}.$$

Here $k = \sqrt{k_1^C k_2^C} = C_f/\sqrt{C_{1\Sigma}C_{2\Sigma}}$ — the coupling coefficient and $d^2 = G_2^2/\omega^2 C_{2\Sigma}^2$. The dependence of the spectral response of the system of coupled parallel oscillatory circuits on the coupling factor is illustrated in Figure 5.11.

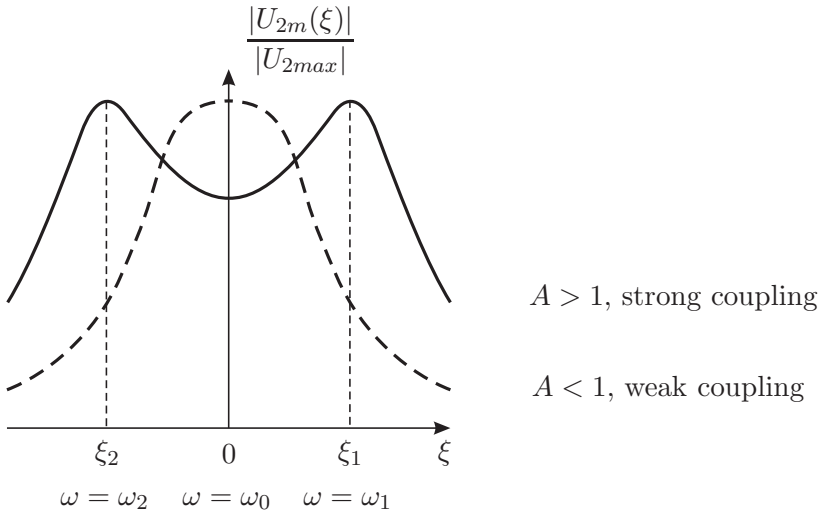

Figure 5.11: Gain-frequency dependence of the system of two coupled circuits: single resonance $\omega = \omega_0$ in the case of the coupling factor $A < 1$ and the splitting of the resonance into ω_1 and ω_2 for $A > 1$.

The correlation between HSI experimental results on nanodimers and the behavior of the system of coupled circuits can be clearly seen. In the case of the "short" dimer ($D = 50$ nm) the coupling factor $A > 1$ and the splitting of the detected spectrum into two frequencies ω_1 and ω_2 around the eigenfrequency ω_0 was observed (Fig. 5.9a). In the case of the "long" dimer ($D = 150$ nm) the coupling between the particles is not strong enough ($A < 1$) to produce resonant splitting.

It, therefore, has been shown that the experimental results obtained in this Chapter for "short" and "long" dimers can be interpreted using the model of two forced oscillations of coupled circuits with capacitance feedback. The difference between the electron-induced photon-emission spectra of two dimers correspond to the excitation of systems with low ($A < 1$) and high ($A > 1$) decoupling factors.

5.7 Summary and conclusions

It was shown that hyperspectral imaging with a scanning electron beam can be used to measure photon maps, spectral and spacial distributions of surface plasmons excited on single nanoparticles and nanodimers with an electron beam at nanoscale resolution.

Excitation of the hybridization mode was demonstrated by the hyperspectral imaging of a gold dimer. It was found that the hybridization mode only exists on a "short" dimer ($D = 50$ nm) in the narrow range of wavelengths very close to the wavelength of the plasmonic resonance of the individual particle.

It was shown that the spectra of a dimer significantly depends on the separation between its constituents: the splitting of the spectrum of a single nanoparticle into symmetric/asymmetric modes has been observed on a "short" dimer. The spectrum of "long" dimer ($D = 150$ nm) did not exhibit any evidence of coupling between the nanoparticles. A comparison between the behavior of a two coupled nanoparticles comprising a dimer and a classical model of forced oscillations of two coupled parallel circuits has been made.

The efficiency of the system can be further improved as detailed in the previous Chapter. A more efficient light collection system would further increase the spatial resolution of the technique to allow imaging of modes excited locally on a nanoparticle.

To summarize, the hyperspectral imaging of plasmonic nanostructures with an electron beam technique proved to be extremely useful in the quick and comprehensive examination of planar nanostructures, such as metal gratings [44], as well as individual and coupled nanoparticles. This technique can be applied to the study of plasmonic properties of nano-scaled planar waveguides and nano-meta-materials. Hyperspectral imaging can also be applied for analysis and design of nanoparticle chain waveguides and all-optical computer nano-components.

5.8 References

[1] K. Kneipp, Y. Wang, H. Kneipp, L.T. Perelman, I. Itzkan, R.R. Dasari, and M.S. Feld. Single molecule detection using surface-enhanced Raman scattering (SERS). *Phys. Rev. Lett.*, 78(9):1667, 1997.

[2] G. Deinum, K. Kneipp, H. Kneipp, I. Itzkan, R.R. Dasari, and M.S. Feld. Single-molecule detection of a cyanine dye in silver colloidal solution using near-infrared surface-enhanced Raman scattering. *Appl. Spec.*, 52(2):175, 1998.

[3] K. Kneipp, H. Kneipp, R. Manoharan, I. Itzkan, R.R. Dasari, and M.S. Feld. Surface-enhanced raman scattering (SERS) — a new tool for single molecule detection and identification. *Bioimaging*, 6(2):104, 1998.

[4] K. Kneipp, H. Kneipp, R. Manoharan, I. Itzkan, R.R. Dasari, and M.S. Feld. Near-infrared surface-enhanced Raman scattering can detect single molecules and observe "hot" vibrational transitions. *J. Raman Spec.*, 29(8):743, 1998.

[5] K. Kneipp, H. Kneipp, I. Itzkan, R.R. Dasari, and M.S. Feld. Surface-enhanced Raman scattering and biophysics. *J. Phys. Cond. Matter*, 14(18):R597, 2002.

[6] K. Kneipp and H. Kneipp. Single molecule Raman scattering. *Appl. Spec.*, 60(12):322A, 2006.

[7] T. Assmus, K. Balasubramanian, K. Burghard, M.and Kern, M. Scolari, N. Fu, A. Myalitsin, and A. Mews. Raman properties of gold nanoparticle-decorated individual carbon nanotubes. *Appl. Phys. Lett.*, 90:173109, 2007.

[8] M.L. Brongersma. Nanoshells: gifts in a gold wrapper. *Nat. Mat.*, 2:296, 2003.

[9] M.C. McAlpine, H. Ahmad, D.W. Wang, and J.R. Heath. Highly ordered nanowire arrays on plastic substrates for ultrasensitive flexible chemical sensors. *Nat. Mat.*, 6(5):379, 2007.

[10] J.W. Li, J.J. Yu, F.Q. Zhao, and B.Z. Zeng. Direct electrochemistry of glucose oxidase entrapped in nano gold particles-ionic liquid-N,N-dimethylformamide composite film on glassy carbon electrode and glucose sensing. *Analytica Chimica Acta*, 587(1):33, 2007.

[11] X.D. Hoa, A.G. Kirk, and M. Tabrizian. Towards integrated and sensitive surface plasmon resonance biosensors: A review of recent progress. *Biosensors and Bioelectronics*, 23:151, 2007.

[12] L. Rogobete, F. Kaminski, M. Agio, and Sandoghdar. Design of plasmonic nanoantennae for enhancing spontaneous emission. *Opt. Lett.*, 32(12):1623, 2007.

[13] O.L. Muskens, V. Giannini, J.A. Sánchez-Gil, and J. Gómez Rivas. Strong enhancement of the radiative decay rate of emitters by single plasmonic nanoantennas. *Nano Lett.*, 7(9):2871, 2007.

[14] I. Romero, J. Aizpurua, G.W. Bruant, and F.J.G. de Abajo. Plasmons in nearly touching metallic nanoparticles: singular response in the limit of touching dimers. *Opt. Express*, 14(21):9988, 2006.

[15] S.A. Maier, M.L. Brongersma, P.G. Kik, S. Meltzer, A.A.G. Requicha, and H.A. Atwater. Plasmonics — a route to nanoscale optical devices. *Adv. Mat.*, 13(19):1501, 2001.

[16] S.A. Maier, P.G. Kik, and H.A. Atwater. Observation of coupled plasmon-polariton modes in Au nanoparticle chain waveguides of different lengths: estimation of waveguide loss. *Appl. Phys. Lett.*, 81(9):1714, 2002.

[17] K.J. Webb and J. Li. Resonant slot optical guiding in metallic nanoparticle chains. *Phys. Rev. B*, 72(20), 2005.

[18] S.L. Zou and G.C. Schatz. Metal nanoparticle array waveguides: Proposed structures for subwavelength devices. *Phys. Rev. B*, 74(12), 2006.

[19] N.F. van Hulst. Light in chains. *Nature*, 448:141, 2007.

[20] C.G. Poulton, M.A. Schmidt, G.J. Pearce, G. Kakarantzas, and P.St.J. Russel. Numerical study of guided modes in arrays of metallic nanowires. *Opt. Lett.*, 32(12):1647, 2007.

[21] I.P. Radko, S.I. Bozhevolnyi, A.B. Evluikhin, and A. Boltasseva. Surface plasmon polariton beam focusing with parabolic nanoparticle chains. *Opt. Express*, 15(11):6576, 2007.

[22] H.E. Ruda and A. Shik. Polarization and plasmon effects in nanowire arrays. *Applied Physics Letters*, 90:223106, 2007.

[23] B.F. Soares, F. Jonsson, and N.I. Zheludev. All-optical phase-change memory in a single gallium nanoparticle. *Phys. Rev. Lett.*, 98(15):153905, 2007.

[24] N.I. Zheludev. Nonlinear optics on the nanoscale. *Contemp. Phys.*, 43(5):365, 2002.

[25] K.F. MacDonald, V.A. Fedotov, S. Pochon, G. Stevens, F.V. Kusmartsev, V.I. Emel'yanov, and N.I. Zheludev. Controlling the coexistence of structural phases and the optical properties of gallium nanoparticles with optical excitation. *Europhys. Lett.*, 67(4):614, 2004.

[26] B.F. Soares, K.F. MacDonald, V.A. Fedotov, and N.I. Zheludev. Light-induced switching between structural forms with different optical properties in a single gallium nanoparticulate. *Nano Lett.*, 5(10):2104, 2005.

[27] K.F. MacDonald, B.E. Soares, M.V. Bashevoy, and N.I. Zheludev. Controlling light with light via structural transformations in metallic nanoparticles. *IEEE J. Sel. Topics In Quant. El.*, 12(3):371, 2006.

[28] B.F. Soares, K.F. MacDonald, and N.I. Zheludev. Resetting single nanoparticle structural phase with nanosecond pulses. *Appl. Phys. Lett.*, 91(4):0431115, 2007.

[29] U. Kreibig and M. Vollmer. *Optical properties of metal clusters*. Springer, Berlin, 1995.

[30] P.K. Hansma and H.P. Broida. Light emission from gold particles excited by electron tunneling. *Appl. Phys. Lett.*, 32(9):545, 1978.

[31] J. Kirtley, T.N. Theis, and J.C. Tsang. Light emission from tunnel junctions on gratings. *Phys. Rev. B*, 24(10):5650, 1981.

[32] N. Kroo, Zs. Szentirmay, and J. Felszerfalvi. On the origin of light emission by tunnel junctions. *Phys. Lett. A*, 81(7):399, 1981.

[33] R.W. Rendell and D.J. Scalapino. Surface plasmons confined by microstructures on tunnel junctions. *Phys. Rev. B*, 24(6):3276, 1981.

[34] J.R. Kirtley, T.N. Theis, and J.C. Tsang. Diffraction-grating-enhanced light emission from tunnel junctions. *Appl. Phys. Lett.*, 37(5):435, 1980.

[35] D.C. Tsui. Observations of surface plasmon excitation by tunneling electrons in GaAs-Pb tunnel junctions. *Phys. Rev. Lett.*, 22(7):293, 1969.

[36] R.N. Hall, J.H. Racette, and H. Ehrenreich. Direct observation of polarons and phonons during tunneling in group 3-5 semiconductor junctions. *Phys. Rev. Lett.*, 4(9):456, 1960.

[37] T. Klar, M. Perner, S. Grosse, G. von Plesse, W. Spirkl, and J. Feldmann. Surface-plasmon resonances in single metallic nanoparticles. *Phys. Rev. Lett.*, 80(19):4249, 1998.

[38] K. Imura, H. Okamoto, M.K. Hossain, and M. Kitajima. Visualization of localized intense optical fields in single gold-nanoparticle assemblies and ultrasensitive Raman active sites. *Nano Lett.*, 6(10):2173, 2006.

[39] M.M.J. Bischoff, M.C.M.M. van der Wielen, and H. van Kempen. STM-induced photon emission spectroscopy of granular gold surfaces in air. *Surf. Sci.*, 400(1-3):127, 1998.

[40] M. Bosman, V.J. Keast, M. Watanabe, A.I. Naaroof, and M.B. Cortie. Mapping surface plasmons at the nanometre scale with an electron beam. *Nanotechnology*, 18:165505, 2007.

[41] J. Nelayah, M. Kociak, O. Stephan, F.J.G. de Abajo, M. Tence, L. Henrard, D. Taverna, I. Pastoriza-Santos, L.M. Liz-Marzan, and C. Colliex. Mapping surface plasmons on a single metallic nanoparticle. *Nat. Phys.*, 2007.

[42] N. Yamamoto, K. Araya, and F.J. Garcia de Abajo. Photon emission from silver particles induced by a high-energy electron beam. *Phys. Rev. B*, 64:205419, 2001.

[43] N. Yamamoto, M. Nakano, and T. Suzuki. Light emission by surface plasmons on nanostructures of metal surfaces induced by high-energy electron beams. *Surf. Interf. Anal.*, 38:1725, 2006.

[44] M.V. Bashevoy, F. Jonsson, K.F. MacDonald, Y. Chen, and N.I. Zheludev. Hyperspectral imaging of plasmonic nanostructures with nanoscale resolution. *Opt. Express*, 15(18):11313, 2007.

[45] A. Sanchez-Iglesias, I. Pastoriza-Santos, J. Perez-Juste, B. Rodriguez-Gonzalez, F.J.G. Abajo, and L.M. Liz-Marzan. Synthesis and optical properties of gold nanodecahedra with size control. *Adv. Mat.*, 18:2529, 2006.

[46] F.J.G. Abajo and A. Howie. Relativistic electron energy loss and electron-induced photon emission in inhomogeneous dielectrics. *Phys.Rev. Lett.*, 80(23):5180, 1998.

[47] P. Nordlander, C. Oubre, E. Prodan, K. Li, and M.I. Stockman. Plasmon hybridization in nanoparticle dimers. *Nano Lett.*, 4(5):899, 2004.

[48] J.H. Song, S.Y. Hong, Y.G. Kim, K.W. Lee, and Y.Y. Kim. Observation of plasmon hybridization in gold nanoparticle pairs. *J. Korean Phys. Soc.*, 50(3):558, 2007.

[49] N. Engheta, A. Salandrino, and A. Alu. Circuit elements at optical frequencies: Nanoinductors, nanocapacitors, and nanoresistors. *Phys. Rev. Lett.*, 95:095504, 2005.

Chapter 6

Summary and future work

6.1 Summary

It was demonstrated for the first time that the electromagnetic field structure near a plasmonic nanoparticle forms a vortex. It was shown that the power-flow lines of linear polarized monochromatic light interacting with a metal $\lambda/20$ nanoparticle, in the proximity of its plasmon resonance, form whirlpool-like nanoscale optical vortices (optical whirlpools). Both spherical and spheroidal particles were studied using analytical Mie theory and the Finite Element method (See Chapter 2). One of two types of vortices, inward or outward, was detected depending on the sign of frequency detuning between the external field and the plasmon resonance of the nanoparticle. It was shown that inward and outward optical whirlpools can exist on a 20 nm spherical silver nanoparticle in the upper ultra-violet and visible range of wavelengths.

A new hyperspectral imaging (HSI) technique with an electron beam for imaging plasmon excitations and cathodoluminescence in nanostructures with nanoscale resolution has been developed. The apparatus for HSI, based on a scanning electron microscope synchronized with a multi-channel spectrum analyzer, allows for collection and detection of optical electron-induced emission from a sample in two configurations (high efficiency and high angular resolution modes) and in the wavelength region from 350 to 1150 nm with 0.8 nm spectral resolution and high quantum efficiency

(See Chapters 3 and 4). The phenomena of light emission from an unstructured gold surface, gratings, single nanoparticles and nanodimers, resulting from the excitation of plasmons with an electron beam, has been analyzed with HSI.

Using this instrument it was demonstrated for the first time that the injection of a beam of free electrons into an unstructured metal surface creates a highly localized nanoscale source of SPPs (See Chapter 3). It was shown that on a gold surface a 50 keV electron beam of 10 μA current creates a 10 nW source of plasmons with the spectrum spreading from 350 to 1150 nm. The plasmons were detected by controlled decoupling into light with a grating at a distance from the excitation point. The 30 nm delocalization of the plasmon source at the grating was demonstrated and decay lengths of SPPs were measured.

The hyperspectral imaging technique was used to study plasmon emission, induced by electron beam excitation on gold monocrystal decahedron-shaped nanoparticles and dimers consisting of such nanoparticles, for the first time (See Chapter 5). It was shown that in 100 nm gold decahedron-shaped nanoparticles electron-induced plasmon emission is excited in the spectral range from 350 to 850 nm. The dependence of spatial and spectral structure of dimer plasmon emission on wavelength and separation between the nanoparticles within the dimer was studied. The excitation of hybridized mode on a dimer with 50 nm gap between the particles was detected at wavelength 600 nm.

6.2 Future work

Numerous avenues of investigation may be followed in relation to the demonstrated whirlpool-like regimes of light interaction with metallic nanoparticles. As a vortex is a very unusual path for the propagation of light, the question of the stability of such an electromagnetic field structure immediately arises. Moreover, it is interesting to investigate if the formation of optical whirlpools can lead to the formation of chaotic electromagnetic fields. The approach developed can also be used to interpret plasmon resonance effects, such as

anomalous absorption and high values of optical cross-sections, not only on single metallic nanoparticles, but also on dimers, waveguides, metamaterial shell structures, nanoparticles on a substrate, and nonlinear nanoparticles.

Currently nanophotonics is progressing towards on-chip nanoplasmonic circuit elements and circuits. The SPP source, generated on the nanoscale with an electron beam, can undoubtedly become one of the key elements of such plasmonic circuits. A range of plasmonic propagation, decoupling, and interference behaviours can be studied using this source. Beyond plasmonics, with recent advances in fabrication, sample characterization, and computational simulation techniques it is now possible to explore interactions between light and electron beams in nanostructured materials using and electron microscope.

Hyperspectral imaging with an electron beam is a powerful technique which can be applied to the study of light emission from various nanostructures, localized plasmon modes, optical density of states, and luminescence of materials. Even in the current stage of development, it can be used for the study of plasmonic properties and design of nanoparticle waveguides, planar surface waveguides, and the study of SPP interference effects in a system of coupled gratings and quasiperiodic hole arrays.

With improved spatial resolution, the fine structure of plasmonic modes of single nanoparticles and nanodimers can be observed with HSI in a scanning electron microscope. Time-resolved measurement of nanodimer response to pulses of electron excitation can be used to obtain deeper insight into the formation of hybridization mode. The spectral range of the light detection could be further expanded into the infrared region. The HSI technique would also undoubtedly benefit from the introduction of polarization sensitivity.

Appendix A

Mie theory solution

In this Appendix the Mie theory formulae used to demonstrate excitation of optical whirlpools on metal nanoparticles of spherical shape are presented in the form of explicit expressions for all components of electric and magnetic fields $(\mathbf{E}, \mathbf{H})$ in the spherical system of coordinates with the polar axis directed along the incident light wave.

Incident field ($\mathbf{E}_i = E_0 e^{ikr\cos\theta}\mathbf{e}_x$):

$$E_{ir} = \sum_{n=1}^{\infty} E_n \left(-i\cos\varphi n(n+1)\sin\theta\pi_n(\cos\theta)\frac{j_n(kr)}{kr} \right).$$

$$E_{i\theta} = \sum_{n=1}^{\infty} E_n \left(\cos\varphi\pi_n(\cos\theta)j_n(kr) - i\cos\varphi\tau_n(\cos\theta)\frac{[krj_n(kr)]'}{kr} \right).$$

$$E_{i\varphi} = \sum_{n=1}^{\infty} E_n \left(-\sin\varphi\tau_n(\cos\theta)j_n(kr) + i\sin\varphi\pi_n(\cos\theta)\frac{[krj_n(kr)]'}{kr} \right).$$

$$H_{ir} = -\frac{k}{\omega}\sum_{n=1}^{\infty} E_n \left(i\sin\varphi n(n+1)\sin\theta\pi_n(\cos\theta)\frac{j_n(kr)}{kr} \right).$$

$$H_{i\theta} = -\frac{k}{\omega}\sum_{n=1}^{\infty} E_n \left(-\sin\varphi\pi_n(\cos\theta)j_n(kr) + i\sin\varphi\tau_n(\cos\theta)\frac{[krj_n(kr)]'}{kr} \right).$$

$$H_{i\varphi} = -\frac{k}{\omega}\sum_{n=1}^{\infty} E_n \left(-\cos\varphi\tau_n(\cos\theta)j_n(kr) + i\cos\varphi\pi_n(\cos\theta)\frac{[krj_n(kr)]'}{kr} \right).$$

Field inside the sphere:

$$E_{1r} = \sum_{n=1}^{\infty} E_n \left(-id_n \cos\varphi n(n+1) \sin\theta \pi_n(\cos\theta) \frac{j_n(k_1 r)}{k_1 r} \right).$$

$$E_{i\theta} = \sum_{n=1}^{\infty} E_n \left(c_n \cos\varphi \pi_n(\cos\theta) j_n(k_1 r) - id_n \cos\varphi \tau_n(\cos\theta) \frac{[k_1 r j_n(k_1 r)]'}{k_1 r} \right).$$

$$E_{i\varphi} = \sum_{n=1}^{\infty} E_n \left(-c_n \sin\varphi \tau_n(\cos\theta) j_n(kr) + id_n \sin\varphi \pi_n(\cos\theta) \frac{[k_1 r j_n(k_1 r)]'}{k_1 r} \right).$$

$$H_{ir} = -\frac{k_1}{\omega} \sum_{n=1}^{\infty} E_n \left(ic_n \sin\varphi n(n+1) \sin\theta \pi_n(\cos\theta) \frac{j_n(k_1 r)}{k_1 r} \right).$$

$$H_{i\theta} = -\frac{k_1}{\omega} \sum_{n=1}^{\infty} E_n \left(-d_n \sin\varphi \pi_n(\cos\theta) j_n(kr) + ic_n \sin\varphi \tau_n(\cos\theta) \frac{[k_1 r j_n(k_1 r)]'}{k_1 r} \right).$$

$$H_{i\varphi} = -\frac{k_1}{\omega} \sum_{n=1}^{\infty} E_n \left(-d_n \cos\varphi \tau_n(\cos\theta) j_n(kr) + ic_n \cos\varphi \pi_n(\cos\theta) \frac{[k_1 r j_n(k_1 r)]'}{k_1 r} \right).$$

Scattered field:

$$E_{sr} = \sum_{n=1}^{\infty} E_n \left(ia_n \cos\varphi n(n+1) \sin\theta \pi_n(\cos\theta) \frac{h_n(kr)}{kr} \right).$$

$$E_{i\theta} = \sum_{n=1}^{\infty} E_n \left(-b_n \cos\varphi \pi_n(\cos\theta) h_n(kr) + ia_n \cos\varphi \tau_n(\cos\theta) \frac{[kr h_n(kr)]'}{kr} \right).$$

$$E_{i\varphi} = \sum_{n=1}^{\infty} E_n \left(b_n \sin\varphi \tau_n(\cos\theta) h_n(kr) - ia_n \sin\varphi \pi_n(\cos\theta) \frac{[kr h_n(kr)]'}{kr} \right).$$

$$H_{ir} = \frac{k}{\omega}\sum_{n=1}^{\infty} E_n \left(ib_n \sin\varphi n(n+1)\sin\theta\pi_n(\cos\theta)\frac{h_n(kr)}{kr} \right).$$

$$H_{i\theta} = \frac{k}{\omega}\sum_{n=1}^{\infty} E_n \left(-a_n \sin\varphi\pi_n(\cos\theta)h_n(kr) + ib_n \sin\varphi\tau_n(\cos\theta)\frac{[krh_n(kr)]'}{kr} \right).$$

$$H_{i\varphi} = \frac{k}{\omega}\sum_{n=1}^{\infty} E_n \left(-a_n \cos\varphi\tau_n(\cos\theta)h_n(kr) + ib_n \cos\varphi\pi_n(\cos\theta)\frac{[krh_n(kr)]'}{kr} \right).$$

Where

$$a_n = \frac{m^2 j_n(mx)[xj_n(x)]' - j_n(x)[mxj_n(mx)]'}{m^2 j_n(mx)[xh_n(x)]' - h_n(x)[mxj_n(mx)]'},$$

$$b_n = \frac{j_n(mx)[xj_n(x)]' - j_n(x)[mxj_n(mx)]'}{j_n(mx)[xh_n(x)]' - h_n(x)[mxj_n(mx)]'}$$

— coefficients inside the sphere.

$$c_n = \frac{j_n(x)[xh_n(x)]' - h_n(x)[xj_n(x)]'}{j_n(mx)[xh_n(x)]' - h_n(x)[mxj_n(mx)]'}.$$

$$d_n = \frac{mj_n(x)[xh_n(x)]' - mh_n(x)[xj_n(x)]'}{m^2 j_n(mx)[xh_n(x)]' - h_n(x)[mxj_n(mx)]'}$$

— the scattering coefficients.

$E_n = E_0 i^n(2n+1)/n(n+1)$.

$x = ka$ — size parameter, a — sphere radius, k — wavenumber of incident wave, $k_1 = mk$ — wavenumber inside the sphere, $m = \sqrt{\varepsilon}$ — relative refractive index, ε — dielectric constant of the sphere, ω — frequency of incident wave.

$j_n(\rho) = \sqrt{\frac{\pi}{2\rho}} J_{n+1/2}(\rho)$ — spherical Bessel function, $J_{n+1/2}(\rho)$ — Bessel function.

$h_n(\rho) = \sqrt{\frac{\pi}{2\rho}} Y_{n+1/2}(\rho)$ — spherical Hankel function, $Y_{n+1/2}(\rho)$ — Hankel function.

$\pi_n = \frac{P_n^1}{\sin\theta}$, $\tau_n = \frac{dP_n^1}{d\theta}$, P_n^1 — associated Legendre function.

Appendix B

Electron-induced photon emission in inhomogeneous materials

This section details the theoretical approach to the calculation of electron-induced photon emission probabilities both in the vicinity and inside the axially symmetric, but otherwise arbitrarily shaped, materials described by frequency-dependent response functions. The software implementation of this technique was kindly provided by its originator, Professor F. J. García de Abajo. The description of the technique is presented below, following the original publication[1].

The computation of electron-induced photon emission spectra from a material of an arbitrary shape can be performed by solving Maxwell's equations numerically using the boundary element method. The electric and magnetic fields in a nonmagnetic inhomogeneous material are conveniently expressed in terms of scalar and vector potentials φ and $\mathbf{A}$ as:

$$\mathbf{E} = \frac{i\omega}{c}\mathbf{A} - \nabla\varphi, \qquad \mathbf{H} = \nabla \times \mathbf{A}.$$

Here the Lorentz gauge condition $\nabla \cdot \mathbf{A} - \frac{i\omega}{c}\varepsilon\varphi = 0$ has been adopted, ε is the space and frequency-dependent local dielectric functions. Maxwell's

[1]F.J. García de Abajo and A. Howie. Relativistic electron energy loss and electron-induced photon emission in inhomogeneous dielectrics, *Phys. Rev. Lett.*, 80:5180, 1998

equations in terms of φ and $\mathbf{A}$ take the form:

$$(\nabla^2 + k^2\varepsilon)\varphi = -4\pi(\rho/\varepsilon + \sigma_s), \tag{B.1}$$

$$(\nabla^2 + k^2\varepsilon)\mathbf{A} = -\frac{4\pi}{c}(\mathbf{j} + \mathbf{m}), \tag{B.2}$$

where $k = \omega/c$, $\sigma_s = \frac{1}{4\pi}\mathbf{D}\cdot\frac{1}{\varepsilon}$, $\mathbf{m} = -\frac{i\omega}{4\pi}\varphi\nabla\varepsilon$, ρ and $\mathbf{j}$ are the external charge and current density, respectively.

Focusing on an abrupt interface separating two different media described by dielectric functions ε_j, $j = 1, 2$, the electromagnetic fields find their source in both the external perturbation and the polarization charges and currents induced on the interface, σ_s and $\mathbf{m}$ as can be seen in equations (B.1), (B.2). Therefore, the fields must result from the propagation of these sources by means of Green functions:

$$G_j(r) = \exp(ik_j r)/r$$

appropriate for each separate medium, where $k_j = k\sqrt{\varepsilon_j(\omega)}$ and the square root is chosen such that k_j lies in the upper complex plane in order to guarantee that the fields vanish at infinity. More precisely, the potentials inside medium j read:

$$\begin{bmatrix} \varphi(\mathbf{r}) \\ \mathbf{A}(\mathbf{r}) \end{bmatrix} = \int d\mathbf{r}' G_j(|\mathbf{r}-\mathbf{r}'|) \begin{bmatrix} \rho(\mathbf{r}')/\varepsilon(\mathbf{r}',\omega) \\ \mathbf{j}(\mathbf{r}')/c \end{bmatrix} + \int d\mathbf{s} G_j(|\mathbf{r}-\mathbf{s}|) \begin{bmatrix} \sigma_j(\mathbf{s}) \\ \mathbf{h}_j(\mathbf{s}) \end{bmatrix},$$

where the additional integrals over the interface S are required partly to include the effects of the interface charges and currents noted above and partly to compensate for the discontinuity of the Green function at the interface.

The continuity of the parallel electric field and the normal magnetic field at the interface is guaranteed by the continuity of the potentials, which leads to:

$$G_1\sigma_1 - G_2\sigma_2 = -(\varphi_1 - \varphi_2), \qquad G_1\mathbf{h}_1 - G_2\mathbf{h}_2 = -(\mathbf{g}_1 - \mathbf{g}_2), \tag{B.3}$$

where:

$$\begin{bmatrix} \varphi_j(\mathbf{s}) \\ f_j(\mathbf{s}) \end{bmatrix} = \int d\mathbf{r} \begin{bmatrix} 1 \\ \mathbf{n}_s\cdot\nabla_s \end{bmatrix} G_j(|\mathbf{s}-\mathbf{r}|)\frac{\rho(\mathbf{r})}{\varepsilon(\mathbf{r},\omega)}, \tag{B.4}$$

and matrix notation has been adopted, so that the interface coordinates $\mathbf{s}$ are used as matrix and vector indices, and matrix–vector products such as $G_j\sigma_j$ involve integration over the interface.

The continuity of the parallel magnetic field and normal electric displacement leads to:

$$H_1\mathbf{h}_1 - H_2\mathbf{h}_2 + \rho\mathbf{n}_s G_1\sigma_1 = -\mathbf{q}_1 + \mathbf{q}_2 - \rho\mathbf{n}_s\varphi_1, \tag{B.5}$$

$$\frac{1}{ik}(\varepsilon_1 H_1\sigma_1 - \varepsilon_2 H_2\sigma_2) - \varepsilon_1\mathbf{n}_s G_1\cdot\mathbf{h}_1 + \varepsilon_2\mathbf{n}_s G_2\cdot\mathbf{h}_2 = \varepsilon_1\left(\mathbf{n}_s\cdot\mathbf{g}_1 - \frac{f_1}{ik}\right) - \varepsilon_2\left(\mathbf{n}_s\cdot\mathbf{g}_2 - \frac{f_2}{ik}\right), \tag{B.6}$$

where $H_j(\mathbf{s}-\mathbf{s}') = \mathbf{n}_s\cdot\nabla_s G_j(|\mathbf{s}-\mathbf{s}'|) \pm 2\pi\delta(\mathbf{s}-\mathbf{s}')$ (the sign is + for $j=1$, and − for $j=2$), $p = k(\varepsilon_2-\varepsilon_1)$,

$$\begin{bmatrix} \mathbf{g}_j(\mathbf{s}) \\ \mathbf{q}_j(\mathbf{s}) \end{bmatrix} = \frac{1}{c}\int d\mathbf{r} \begin{bmatrix} 1 \\ \mathbf{n}_s\cdot\nabla_s \end{bmatrix} G_j(|\mathbf{s}-\mathbf{r}|)\mathbf{j}(\mathbf{r}), \tag{B.7}$$

and $\mathbf{n}_s$ is chosen towards medium 2.

Upon discretization of the surface integrals using N points, equations (B.3)–(B.7) become a set of $8N$ linear equations, which can be solved by direct numerical inversion in a time proportional to $512N^3$. A more efficient ($6N^3$) numerical procedure has been followed, consisting of separately manipulating operators such as G_j, which now become $N\times N$ matrices.

For simplicity, the case of axially symmetric, but otherwise arbitrarily shaped, materials is considered. This allows analytical evaluation of the azimuthal interface integrals, so that the number of points N is considerably reduced, though one has to sum over the azimuthal momentum number m.

The electron-induced photon emission probability Γ^{rad} can be obtained by dividing the component of the Poynting vector normal to an arbitrarily large sphere centered at the sample by ω.

The described numerical technique was implemented by Professor F.J. García de Abajo in the form of Bemax software. This program allows for the calculation of electron-induced photon emission spectra from isolated objects with axial symmetry, such as disks, ellipsoids, or coated spheres, illuminated by an electron beam of selected energy, positioned parallel or perpendicular to the object.

Appendix C

Refereed publications

[1] **Excitation of localized plasmon modes in nanoparticle dimers with an electron beam**

M. V. Bashevoy, F. Jonsson, K. F. MacDonald, F. J. Garcia de Abajo, L. M. Liz-Marzán, and N. I. Zheludev

Submitted to Applied Physics Letters.

[2] **Hyperspectral imaging of plasmonic nanostructures with nanoscale resolution**

M.V. Bashevoy, F. Jonsson, K.F. MacDonald, Y. Chen, and N.I. Zheludev

Optics Express 15(18):11313, 2007.

[3] **Hyperspectral imaging of plasmonic excitations induced by an electron beam**

M.V. Bashevoy, F. Jonsson and N.I. Zheludev

In *CLEO/QELS 2007: Conference on Lasers and Electro-Optics: Quantum Electronics and Laser Science Conference*, 2007.

[4] **Hyperspectral imaging of gold dimers**

M.V. Bashevoy, F. Jonsson, N.I. Zheludev, F.J. García de Abajo, I. Pastoriza-Santos and L.M. Liz Marzán

In *Conference on Lasers and Electro-Optics (CLEO)-Europe/International Quantum Electronics Conference (IQEC)*, 2007.

[5] **Electron beam excitation of plasmonic modes in gold dimers**

M.V. Bashevoy, F. Jonsson, N.I. Zheludev, F.J. García de Abajo, I. Pastoriza-Santos and L.M. Liz Marzán

In *International Conference on Coherent and Nonlinear Optics (ICONO)/International Conference on Lasers, Applications, and Technologies*, 2007.

[6] **Generation of surface plasmons by electron beam excitation**

M.V. Bashevoy, F. Jonsson, N.I. Zheludev and C. Yifang

In *Nanometa 2007: The 1st European Topical Meeting on Nanophotonics and Metamaterials*, 2007.

[7] **Polymorphic nanoparticles as all-optical memory elements**

B.F. Soares, M.V. Bashevoy, F. Jonsson, K.F. MacDonald, and N.I. Zheludev

Optics Express 14(22):10652, 2006.

[8] **Generation of traveling surface plasmon waves by free-electron impact**

M.V. Bashevoy, F. Jonsson, A.V. Krasavin, N.I. Zheludev, Y. Chen, and M.I. Stockman

Nano Letters 6(6):1113, 2006.

[9] **Controlling light with light via structural transformations in metallic nanoparticles**

K.F. MacDonald, B.F. Soares, M.V. Bashevoy, and N.I. Zheludev

IEEE Journal of Selected Topics in Quantum Electronics 12(3):371, 2006.

[10] **Optical whirlpool on an absorbing metallic nanoparticle**

M.V. Bashevoy, V.A. Fedotov, and N.I. Zheludev

Optics Express 13(21):8372, 2005.